Single-Photon Frequency Upconversion for Long-Distance Quantum Teleportation and Communication

by

Marius A. Albota

B.S. Engineering Physics, Cornell University (1997)
S.M. Electrical Engineering and Computer Science, MIT (2002)

Submitted to the Department of Electrical Engineering and Computer Science
in partial fulfillment of the requirements for the degree of
Doctor of Philosophy in Electrical Engineering and Computer Science
at the
MASSACHUSETTS INSTITUTE OF TECHNOLOGY
June 2006

Author . . . .
Department of Electrical Engineering and Computer Science
May 26, 2006

Certified by . . . .
Franco N. C. Wong
Senior Research Scientist
Thesis Supervisor

Certified by . . . .
Jeffrey H. Shapiro
Julius A. Stratton Professor of Electrical Engineering
Thesis Supervisor

Accepted by . . . .
Arthur C. Smith
Chairman, Department Committee on Graduate Students

Single-Photon Frequency Upconversion for Long-Distance Quantum Teleportation and Communication

by

Marius A. Albota

Submitted to the Department of Electrical Engineering and Computer Science
on May 26, 2006, in partial fulfillment of the
requirements for the degree of
Doctor of Philosophy in Electrical Engineering and Computer Science

Abstract

Entanglement generation, single-photon detection, and frequency translation that preserves the polarization quantum state of the photons are essential technologies for long distance quantum communication protocols. This thesis investigates the application of polarization entanglement to quantum communication, including frequency upconversion, photon-counting detection, and photon-pair and entanglement generation. We demonstrate a near-unity efficient frequency conversion scheme that allows fast and efficient photon counting at wavelengths in the low-loss fiberoptic and atmospheric transmission band near 1.55 μm. This upconverter, which is polarization-selective, is useful for classical as well as quantum optical communication. We investigate several schemes that allow frequency translation of polarization-entangled photons generated via spontaneous parametric downconversion in second order nonlinear crystals. We demonstrate upconversion from $\sim$1.56 to 0.633 μm that preserves the polarization state of an arbitrarily polarized input. The polarization-insensitive upconverter uses bidirectional sum-frequency generation in bulk periodically poled lithium niobate and a Michelson interferometer to stabilize the phase. Using this bidirectional upconversion technique, entangled photons produced in a periodically poled parametric downconverter can be translated to a different wavelength with preservation of their polarization state. We discuss the implications of these results for quantum information processing.

Thesis Supervisor: Franco N. C. Wong
Title: Senior Research Scientist

Thesis Supervisor: Jeffrey H. Shapiro
Title: Julius A. Stratton Professor of Electrical Engineering

Single-Photon Frequency Upconversion for Long-Distance Quantum Teleportation and Communication

by

Marius A. Albota

Submitted to the Department of Electrical Engineering and Computer Science
on May 26, 2006, in partial fulfillment of the
requirements for the degree of
Doctor of Philosophy in Electrical Engineering and Computer Science

Abstract

Entanglement generation, single-photon detection, and frequency translation that preserves the polarization quantum state of the photons are essential technologies for long distance quantum communication protocols. This thesis investigates the application of polarization entanglement to quantum communication, including frequency upconversion, photon-counting detection, and photon-pair and entanglement generation. We demonstrate a near-unity efficient frequency conversion scheme that allows fast and efficient photon counting at wavelengths in the low-loss fiberoptic and atmospheric transmission band near 1.55 μm. This upconverter, which is polarization-selective, is useful for classical as well as quantum optical communication. We investigate several schemes that allow frequency translation of polarization-entangled photons generated via spontaneous parametric downconversion in second order nonlinear crystals. We demonstrate upconversion from $\sim$1.56 to 0.633 μm that preserves the polarization state of an arbitrarily polarized input. The polarization-insensitive upconverter uses bidirectional sum-frequency generation in bulk periodically poled lithium niobate and a Michelson interferometer to stabilize the phase. Using this bidirectional upconversion technique, entangled photons produced in a periodically poled parametric downconverter can be translated to a different wavelength with preservation of their polarization state. We discuss the implications of these results for quantum information processing.

Thesis Supervisor: Franco N. C. Wong
Title: Senior Research Scientist

Thesis Supervisor: Jeffrey H. Shapiro
Title: Julius A. Stratton Professor of Electrical Engineering

Dedicated to my family and in the memory of my sister.

Acknowledgments

First, I would like to thank Franco Wong, my thesis advisor, for suffering through six long years with me. Franco's door, conveniently located vis-a-vis my own office, was always open. I often used (Franco might argue abused) his convenient location to engage him in passionate discussions about everything from politics, to the stock market, to quantum and nonlinear optics. In his visits to the lab, Franco never shied away from turning and pushing, as I looked on with fear, the many knobs and switches of my experiments, and in doing so helping me pinpoint problems.

I would also like to thank my thesis co-advisor, Jeffrey Shapiro. Our many discussions on the theory of quantum-state up- as well as down-conversion greatly influenced the development of this thesis. He was extraordinarily helpful to me as he has the rare ability to put theory in an experimental context and vice versa. I look forward to continuing to work with him at Lincoln Laboratory for many years to come.

Prof. Franz Kärtner provided valuable insight during our meetings and I am thankful that he agreed to serve as a member of my thesis committee.

I would like to thank Bill Keicher, my Group Leader at Lincoln Laboratory, for his continuous support of my academic career. He was instrumental in seeing that I had the financial support to complete my doctorate. Dave Kocher has been a mentor to me from the first day I joined MIT Lincoln Laboratory in 1997. I thank him for this friendship and help.

I would like to thank my fellow graduate students: T. Kim, O. Kuzucu, and I. Stork for our many enjoyable lunch-time conversations and useful technical discussions. I also appreciate the advice, support, and friendship received over the years from former members of our group: C. Kuklewicz, E. Mason, G. Messin, E. Keskiner, and P. Gorelik.

My family has always been here for me throughout the years and I'd like to thank them for their support and encouragement.

My wife, partner, and love of my life Beth, has been with me through many difficult times and she always stood by me. I can't thank her enough for her support, constant encouragement, friendship, and unconditional love.

Finally, I thank MIT Lincoln Laboratory and the Lincoln Scholars Program for supporting this research.

.... and, of course, I thank Phooka and Loki for the constant purrs and entertainment.

Contents

List of Figures

List of Tables

Chapter 1

Introduction

Entanglement is the essential resource for quantum information processing. The proposed schemes for the construction of future quantum information networks rely on the efficient creation, long-distance distribution, and storage of entanglement [1, 2, 3]. Spontaneous parametric downconversion (SPDC) via a 2^{nd} order nonlinear process in a crystalline medium is the most widely used scheme for generating entangled signal (s) and idler (i) photons. Pairs of photons, where by convention $\lambda_s < \lambda_i$, are said to be entangled if they are in an unfactorizable quantum state, as defined by Schrödinger [4]. When post-selection is used, a polarization entangled joint signal-idler state of the following form is generated [5]

$$|\psi\rangle_{si} = \frac{1}{\sqrt{2}}[|H\rangle_s|V\rangle_i + |V\rangle_s|H\rangle_i e^{j\phi}], \tag{1.1}$$

where $|H\rangle$ and $|V\rangle$ denote horizontal (H) and vertical (V) polarization states, ϕ is the relative phase, and spatio-temporal characteristics have been suppressed. Twenty three years ago, Alain Aspect and his collaborators [6] demonstrated the inconsistencies between Einstein, Podolsky, and Rosen's (EPR) suggestions of a hidden-variable theory [7] and physical observations. Their experiment showed that entanglement produces nonlocal correlations which cannot be explained classically. Ever since, there have been many experiments that have explored the foundations of quantum mechanics and have validated the inequalities derived by John Bell [8, 9]. Most of these experiments have been undertaken using entangled pairs of photons. Photons produced via SPDC [10, 11, 12] can be hyperentangled, which means that they exhibit degrees of correlation beyond classically allowed limits in several variables such as time, frequency, polarization, momentum or position [5]. A wide range of quantum applications for these sources of entangled light have been proposed, including quantum-enhanced channel capacity, metrology (positioning, ranging, and time-of-arrival measurements), conveyor-belt clock synchronization, multi-particle entangled states, teleportation, quantum logic and computation [13, 14, 15, 16]. Polarization-entangled qubits can also be utilized to create a one-time secret key pad for applications in quantum cryptography [17, 18, 19] and quantum key distribution (QKD) [20, 21]. These technologies hold the promise of enhancing the classical limits of computation, timing accuracy, imaging, ranging, and communication, and may also open up new information processing schemes that would be inconceivable in the classical world.

Entangled states lie at the heart of long-distance quantum teleportation. The efficient generation of entangled photons followed by the distribution of entanglement is an essential part of a support infrastructure for quantum communications and distributed quantum networks [22]. Photons represent the best choice for long-distance entanglement distribution while atomic or ionic quantum memories are the preferred storage and processing nodes for a quantum information network. A novel protocol investigated by Duan, Lukin, Cirac, and Zoller (DLCZ), uses entangled atomic ensembles to establish the resource necessary for teleporation-assisted quantum communication [1]. A different architecture for long-distance quantum communication has been proposed by researchers from the Massachusetts Institute of Technology and Northwestern University (MIT/NU). The MIT/NU proposal for qubit teleportation [2] relies on fiber-optic transmission of polarization-entangled photons [22] and trapped Rubidium (Rb) atom quantum memories [3]. Its concept for entanglement distribution to a pair of quantum memories is illustrated in Fig. 1-1. The photons are generated by a dual parametric downconverter source that can produce the narrow bandwidth 795-nm polarization-entangled signal and idler photons that are needed

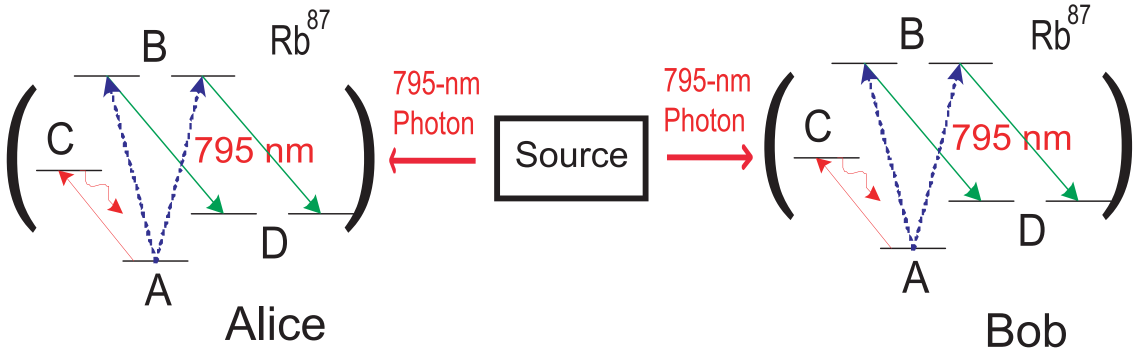

Figure 1-1: Schematic of the proposed experiment for creating long distance entanglement between a pair of trapped rubidium atoms. Each optical cavity contains a single trapped atom of ^{87}Rb, whose relevant hyperfine levels have been shown schematically here as A, B, C, D.

to match the MHz-wide D_2 absorption line of Rb [3]. The entangled photons are sent to a pair of quantum memories where the photons are absorbed by the trapped atoms, thus transferring their entanglement to the memories. This quantum memory scheme has been analyzed in detail by Lloyd and collaborators [3]; the following brief description will suffice for our purposes. Initially, each Rb atom is in the hyperfine ground state A. An arbitrarily polarized 795-nm photon can then be absorbed, transferring its polarization state to the energy-degenerate B levels. By means of a Raman transition, this coherence is then shelved in the long-lived D levels. As explained in [3], once both memories have shared entanglement, the rest of the qubit teleportation protocol can be completed by means of additional atomic levels not shown in Fig. 1-1. The energy levels of Rb have another desirable feature – they allow for the non-destructive verification of the cavity loading process via the A-to-C cycling transition. By monitoring the cavity for the fluorescence from this cycling transition, we can reliably infer whether or not a 795 nm photon has been absorbed by the atom in that cavity. An in-depth analysis of this communication scheme has shown that the architecture can achieve loss-limited throughput as high as 200 entangled-pairs/sec with 97.5% fidelity over a 50 km path when there is 10 dB of fixed loss in the overall system and 0.2 dB/km fiber propagation loss [2]. The MIT/NU quantum communication architecture, containing the source and the quantum memory, represents a complete scheme for the production, distribution, and storage of entanglement and may form the basis of more complex future quantum communication networks [2].

To realize the throughput quoted above, photon transmission was presumed to occur through optical fiber in the low-loss 1.55 μm transmission band. To do so, the dual parametric amplifier can be located in close proximity to one of the memories and arranged so that its paired photons are at 795 nm—for loading into the local memory at the appropriate hyperfine line of Rb—and 1.55 μm for long-distance fiber transmission to the remote memory. The architecture for long-distance quantum communication is then as shown in Fig. 1-2. Entangled signal (795 nm) and idler (1550 nm) photons are loaded into local (s) and remote (i) Rb-atom quantum memories, respectively. We can think of this process as transferring entanglement between flying qubits – the photons – and stationary qubits – the trapped atoms. Once the photonic entanglement has been transferred to the atomic storage nodes, an entanglement resource is established. This entanglement resource can subsequently be used to teleport the atomic state m of an atom from Alice to Bob.

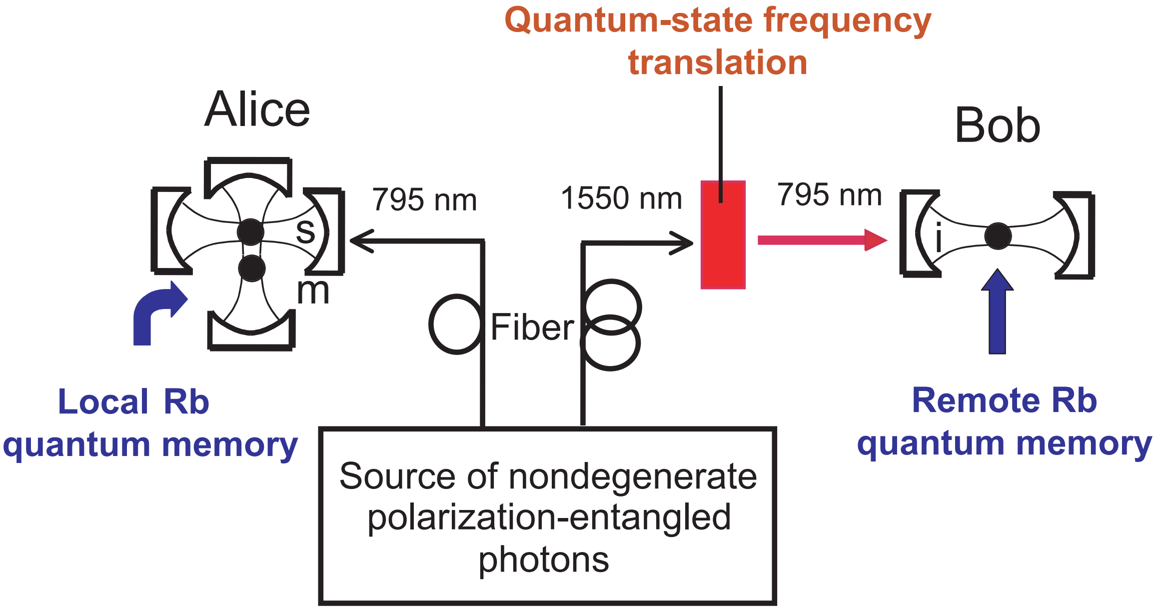

Figure 1-2: Architecture for long-distance quantum communication [2]. Entangled signal (795 nm) and idler (1550 nm) photons are loaded into local (s) and remote (i) Rb-atom quantum memories, respectively. Once the entanglement resource is established, it can be used for teleporting the atomic state m.

Because the 1.55 μm photon – used for long distance fiber transmission – does not match the 795 nm Rb line of the remote quantum memory we need a wavelength conversion device that maintains the coherence of quantum information as it is moved from a 1.55 μm photon to a 795 nm photon and then to the Rb atom. Specifically, in order to load the remotely-located memory as shown in Fig. 1-2, quantum-state frequency conversion [23] is required, so that the polarization state of the 1.55 μm photon is transferred to a 795 nm photon without loss of coherence. This form of frequency upconversion is therefore subject to very stringent requirements. It must function down to the single photon level with low insertion loss, while providing both high conversion efficiency and high-fidelity preservation of arbitrary polarization states. No such device presently exists, but were one available it would have a considerably broader impact than just enabling the loading of remote quantum memories. In particular, using a commercial Silicon (Si) Geiger-mode avalanche photodiode (APD) to perform photon counting on the upconverter's output would afford polarization-insensitive single-photon counting capability in the fiber-optic and atmospheric transmission bands that is far better than what is currently available from custom-built Indium Gallium Arsenide (InGaAs) or Germanium (Ge) Geiger-mode APDs [24, 25, 26, 27, 28]. This enhanced capability is of interest for high-sensitivity classical optical communication and quantum key distribution. The low-loss transmission windows in the short (S), conventional (C), and long (L) wavelength telecommunication bands are particularly well suited for long-range communication with geo-synchronous satellites and for high-sensitivity interplanetary optical data transmission. High-resolution optical imaging and ranging applications such as laser radar [29, 30] would also greatly benefit from enhanced photon counting technologies at eye-safe wavelengths in the telecommunication bands.

1.1 Summary of the Main Results

In this thesis, we investigate several essential components of an entanglement-based quantum communication architecture. Our main focus will be the demonstration of efficient polarization-preserving frequency upconversion at the single-photon level. We also develop high-performance 1.55 μm photon counting using upconversion and InGaAs avalanche photodiodes and report progress on entanglement generation. The remainder of the thesis is organized as follows.

Chapter 2 describes our work on entanglement generation and 1.55 μm single-photon detectors. We discuss the main features of an efficient source of nondegenerate photon pairs at 795 and 1609 nm based on bulk periodically poled lithium niobate (PPLN) [31]. We also discuss the performance characteristics of a polarization entanglement source at these wavelengths which is based on a bidirectionally-pumped PPLN parametric downconverter [32]. This source has an inferred bandwidth of $\sim$60 GHz and a spectral brightness of 300 pairs/s/GHz/mW of pump power. We have obtained a quantum interference visibility of $\sim$90% and verified the violation of the Clauser-Horne-Shimony-Holt (CHSH) form of Bell's inequality [33]. In Chapter 2 we also summarize the performance characteristics of our 1.55-μm sensitive single photon detectors. The counters we develop use commercial InGaAs APDs together with custom-built Peltier-cooling and custom Geiger-mode circuitry. When biased above their breakdown voltage in passively-quenched mode, these detectors are capable of $\sim$20% quantum efficiency and dark-count probabilities of less than 0.2% per 20-ns measurement interval. We compare their performance with the characteristics of other photon-counting technologies.

Chapter 3 is devoted to reviewing the theory of sum-frequency generation. A fully quantum treatment for upconversion of plane-wave modes is used to show that quantum-state frequency conversion is possible. We also present a classical treatment, which is more readily connected to the parameters of our experiments.

In Chapter 4 we present our demonstration of 90%-efficient frequency upconversion of single photons in the telecommunication band around 1.55-μm. The scheme uses a high-finesse traveling wave cavity for the pump beam that is stabilized for high-power and continuous-wave (cw) operation. Upconversion provides a novel and attractive way to detect photons at telecommunication wavelengths where good commercial single photon counters do not exist. We report efficient polarization-selective cw single-photon detection at 1.55 μm via sum-frequency mixing with a strong pump at 1.064 μm in PPLN followed by photon counting in the visible [34, 35]. This cascaded detection technique offers significant advantages over existing 1.55 μm photon-counting technologies, including continuous-mode operation, higher detection efficiency, higher counting rates, and no afterpulsing. The photon-counting setup we demonstrate has a variety of spinoff applications in the classical world, such as deep-space optical communication and imaging laser radar. We compare our technique with a scheme that uses upconversion in a PPLN waveguide.

Chapter 5 explores and contrasts several modalities for achieving polarization-preserving quantum-state frequency upconversion. We concentrate our discussion on architectures that employ upconversion in a bulk PPLN crystal. We are particularly interested in quantifying whether the quantum coherence survives, in principle, the process of frequency conversion in each of these schemes.

The main goal of this thesis is to demonstrate polarization-preserving frequency translation. In Chapter 6 we report the efficient upconversion from 1.55 μm to 0.633 μm of individual photons of any linear polarization [36, 37]. Wavelength tunability of the probe (from 1.5 to 1.6 μm) and the upconverted photons (to the 0.795 μm Rb-absorption line) can be easily accomplished with temperature tuning of the crystal and with a change in the pump wavelength. We implement efficient polarization-preserving wavelength translation using a bi-directional upconversion scheme in a servo-locked standing wave optical resonator. In our experiments, the input horizontal (vertical) polarization is converted in the forward (backward) direction and a dichroic Michelson interferometer is stabilized to lock the relative phase and maintain the polarization angle. We conclude, in Chapter 7, by summarizing the main achievements of this work and by discussing some of the remaining challenges.

1.2 Notation and Abbreviations

We will try to remain consistent with notation throughout the thesis. However some notation may change between chapters for clarity. The main symbols that appear

Notation	Definition
$\lambda_{p,i,s} = 2\pi c/\omega_{p,i,s}$	Pump, idler, and signal vacuum wavelengths
$\chi^{(2)}$	2^{nd} order nonlinear optical susceptibility
ϕ	Phase of the optical field
$\lvert H\rangle$ (or $\updownarrow$)	Horizontally-polarized (in plane or TM) state
$\lvert V\rangle$ (or $\bullet$)	Vertically-polarized (normal or TE) state
$\lvert\psi\rangle_{si}$	Polarization-entangled joint signal-idler state

Table 1.1: This table shows for reference the common symbols used throughout the thesis.

throughout this thesis and their definitions are tabulated here for convenience. Tables 1.1 and 1.2 describe the major notation and abbreviations in this thesis.

Abbreviation	Definition
SPDC	Spontaneous parametric downconversion
CHSH	Clauser, Horne, Shimony, Holt version of Bell's inequality
QPM	Quasi phasematching
SFG	Sum frequency generation
SHG	Second harmonic generation
PPLN	Periodically poled lithium niobate
LN ($LiNbO_3$)	Lithium niobate
MgO:PPLN	Magnesium-oxide doped periodically poled lithium niobate
InGaAs/InP	Indium gallium arsenide/indium phosphide
Si	Silicon
APD	Avalanche photodiode
cw	Continuous wave
QWP/HWP/PBS	Quarter-wave plate/Half-wave plate/Polarizing beam splitter
HR/HT	High-reflection/High-transmission
SPCM	Single-photon counting module (Si-based Geiger-mode APD)
PZT	Piezoelectric transducer
EDFA	Erbium-doped fiber amplifier
ASE	Amplified spontaneous emission
SNR	Signal-to-noise ratio
TIA	Transimpedance amplifier
AR	Anti-reflection

Table 1.2: This table displays the common abbreviations used throughout this thesis.

Chapter 2

Entanglement Generation and Detection

2.1 Entangled-Photon Generation

The preferred optical technique for producing polarization-entangled photons has been SPDC. Several schemes that use the $\chi^{(2)}$ nonlinearity of optical crystals to generate pairs of photons have been reported in type-I and type-II single-pass and cavity-enhanced configurations [38, 39]. Some of the earlier experiments have employed pulsed-SPDC in critically phase matched birefringent crystals, like beta-barium borate (BBO) [10, 11]. With such a setup, pairs of orthogonally polarized signal and idler photons are generated using a laser that is often in the ultraviolet. For example, using type-I birefringently phase matched parametric downconversion in two identical crystals oriented at 90°, researchers have produced 1.5×10^6 frequency degenerate entangled photons per second per 150 mW of pump power at 702 nm center wavelength with a spectral bandwidth of 5 nm [11]. The output downconverted light is spatially emitted along two conical manifolds with orthogonal relative polarizations. Besides being spectrally broad, and therefore not useful for exciting narrowband atomic transitions, the spatial structure of the output exhibited by this source is not particularly well suited for fiberoptic coupling. We have chosen to implement our nondegenerate SPDC source by taking advantage of noncritical quasi-phase matching (QPM) [40, 41] in a temperature-tunable bulk PPLN crystal [42]. QPM allows for a wide acceptance angle and the output beams from our type-I system are co-polarized and collinearly propagating with little walkoff, making their manipulation and coupling into single-mode fibers easier. More recent experiments on entanglement sources, undertaken in our group, have produced high-flux sources that exhibit quantum-interference visibilities in excess of 98-99% [43, 44].

2.2 Entanglement Sources for Long-Distance Quantum Communication

The process of parametric downconversion (three-wave mixing of a strong pump with vacuum signal and idler fields) involves the spontaneous conversion of power from a higher-frequency pump field to newly generated signal and idler fields of lower frequencies. As shown in Chapter 3, efficient SPDC occurs if the phase matching condition, dictated by momentum conservation, is satisfied inside a $\chi^{(2)}$ nonlinear crystal. One can show that for every pump photon that is annihilated in the downconversion process there is a signal photon and an idler photon that share non-classical correlations in time (are simultaneously created), energy, polarization, and momentum [45]. The process of spontaneous parametric downconversion is illustrated in Fig. 2-1. The pump (p), signal (s) and idler (i) frequencies are constrained by energy conservation to obey $\omega_p = \omega_s + \omega_i$, where $\omega_s > \omega_i$. Fundamental as well as economic considerations will, most likely, require any real-world implementation of quantum communication schemes to use the existing fiberoptic infrastructure. It will therefore be imperative to generate the entangled photons at wavelengths in the minimum-loss silica transmission window (1.5 to 1.6 μm). For long-distance quantum communication, the embodiment of the MIT/NU protocol relies on a highly-nondegenerate source of polarization-entangled photons, with signal and idler wavelengths near 0.795 and 1.6 μm, respectively. According to theoretical predictions [2, 22], a PPLN-based doubly resonant optical parametric amplifier that is resonant in both signal and idler fields

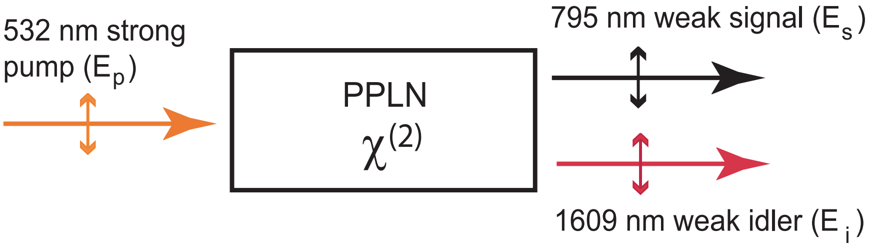

Figure 2-1: Type-I frequency downconversion of a strong pump (E_p) in periodically poled lithium niobate. The wavelengths of the co-polarized signal (E_s) and idler (E_i) output fields are tunable via a change in the crystal's temperature or grating period.

would be capable of a pair production rate of 1.5×10^6 s^{-1} per mW of pump power over a 30-MHz bandwidth around 0.795 and 1.609 μm center wavelengths. This photon-pair generation rate is estimated to be orders of magnitude brighter than previous sources within the bandwidth of the cavity containing a Rb atom.

2.3 Nondegenerate Photon-Pair Production

In this section we briefly discuss the experimental realization of a PPLN-based downconversion scheme that produces photon twins at the highly nondegenerate center wavelengths of 808 nm and at 1.56 μm. The schematic of the experimental setup for photon-pair generation is shown in Fig. 2-2. We used a 0.5 mm (T) × 12 mm (W) × 20 mm (L) periodically poled LiNbO$_3$ crystal with a grating period of 21.6 μm designed for 3$^{\text{rd}}$ order quasi-phase-matching. We fabricated this device at MIT Lincoln Laboratory using lithography and electric-field poling [46, 47]. The crystal was anti-reflection (AR)-coated at the pump, signal and idler wavelengths $\lambda_p = 0.53$, $\lambda_s = 0.8$, and $\lambda_i = 1.6$ μm. The bulk PPLN was pumped with cw light at 532 nm from a

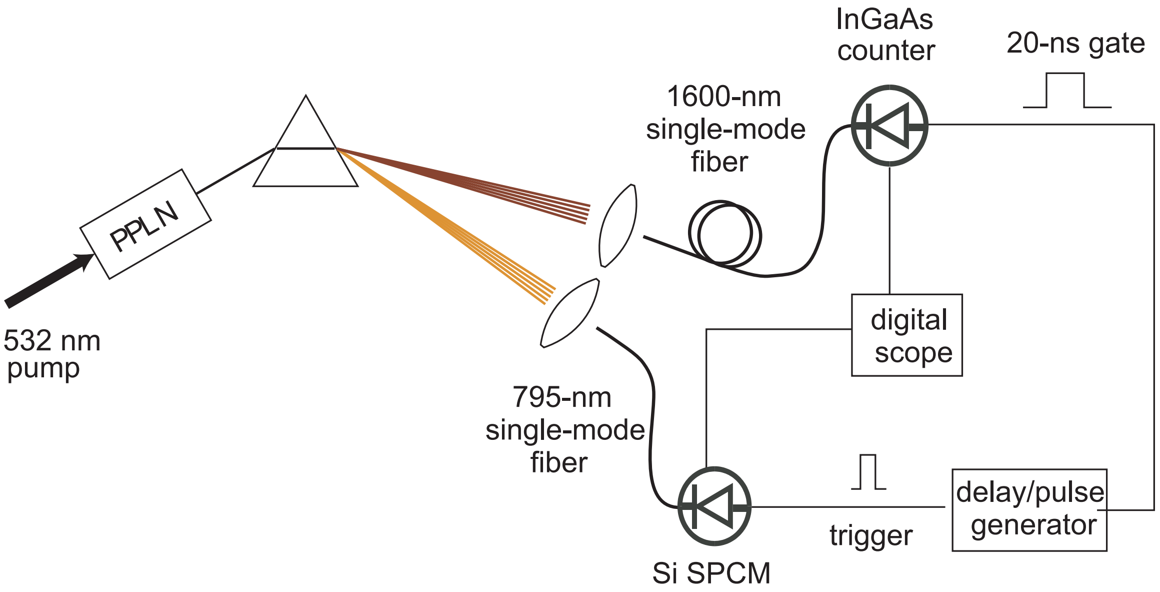

Figure 2-2: Simplified experimental setup for nondegenerate photon-pair generation in bulk PPLN. The colinearly propagating downconverted signal and idler photons are detected with Si and InGaAs photon counters, respectively. For coincidence counting, the Si APD triggers the pulse generator, which in turn gates on the custom-built InGaAs photon counter.

frequency-doubled Nd:YVO_4 laser (Coherent Verdi-8). The crystal was temperature stabilized inside a commercial oven (Super Optronics) with ±0.1°C stability. The PPLN was set up for collinear propagation with its z axis aligned with the pump's horizontal polarization. For type-I QPM, the d_{33} nonlinear coefficient of $LiNbO_3$ was utilized, and the signal and idler outputs were also polarized along the crystal's z axis. In this configuration, the SPDC source produced two collinearly-propagating and co-polarized signal and idler beams in a single pass through the nonlinear crystal.

When operated at a temperature of $\sim$142.4°C the PPLN source produced frequency-nondegenerate outputs at 1.559 μm (idler) and 808 nm (signal). This pair of wavelengths is of interest, for characterization measurements and for a first demonstration of this type of source, because the idler lies in the middle of the low-loss fiber transmission window and the signal is near the peak detection efficiency of Si SPCMs. These center wavelengths could be tuned by varying the crystal temperature over a range of 50°C. For example, at a temperature of 181.5°C, the idler and signal outputs were 1609 nm and 795 nm, respectively.

The downconverted beams were separated at the output using a prism. The signal photons were coupled into a visible/near infrared single-mode fiber and detected using a free-space SPCM (PerkinElmer model SPCM-AQR-14) with ~150 μm active-area diameter and ~55% quantum efficiency at 808 nm. In response to the incident photoelectrons, the Si APD produced 30-ns-duration, 3 V pulses with rise times on the order of 5 ns. The idler beam was coupled into a single mode telecom fiberoptic patchcord (SMF-28), followed by a fiberoptic delay line (~70 m). In this way the idler photons were delivered to a fiber-pigtailed InGaAs detector module custom-built to operate in Geiger mode. The electronic output pulse from the Si SPCM triggered a fast pulse generator (Stanford Research Systems DG535), which, in turn, sent a bias pulse to the InGaAs detector. This bias, or gating pulse turned the InGaAs APD on for the expected arrival the conjugate idler photon. The repetition rate of the gate pulse was limited in hardware to 10 kHz and a fiberoptic delay line was introduced to compensate for the finite turn-on times of bias electronics and other components. The output from the InGaAs detector and that from the Si SPCM were both fed into software-controlled Gage Scope digitizing data acquisition PC cards. Data collection was performed using LabView and Matlab was used to process the data for coincidences. Using ~2 mW of pump power at 532 nm, we measured a 3% conditional probability, within a 4 ns counting interval, of detecting an idler photon given the prior detection of a signal photon. The measured conditional detection probability was limited by the detector quantum efficiency, propagation loss, and fiber coupling efficiency of the idler mode that was matched to the signal mode. We measured an inferred pair generation rate of 1.4×10^7 pairs/s per mW of pump power tunable over a signal bandwidth of ~150 GHz [31].

2.4 A Frequency Nondegenerate Source of Polarization Entanglement

The configuration for efficient generation of nondegenerate polarization entanglement was proposed by Shapiro and Wong [22] and is shown schematically in Fig. 2-3. The experimental realization of this scheme was implemented by combining the outputs of a bidirectionally-pumped PPLN downconverter, as shown in Fig. 2-4 [32]. The cw

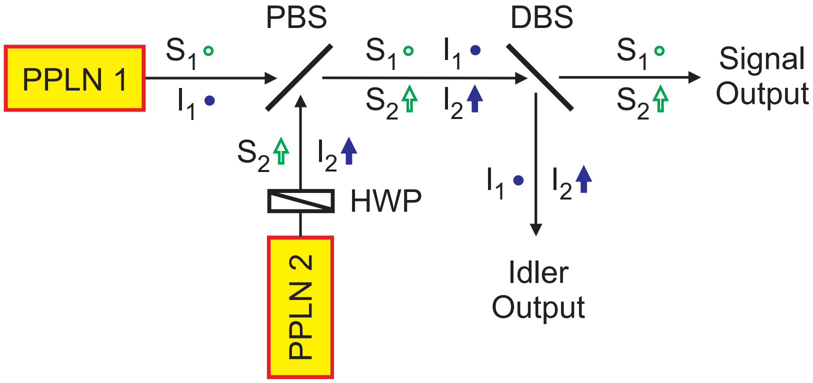

Figure 2-3: Entanglement generation: the outputs of two type-I nondegenerate downconverters can be judiciously combined to produce a high-flux source of polarization entangled photons. PBS: polarization beam splitter; HWP: half-wave plate; DBS: dichroic beam splitter.

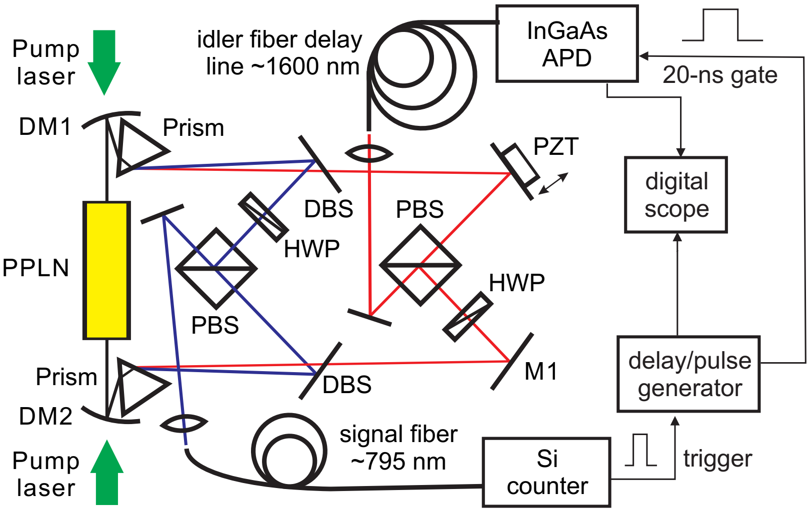

Figure 2-4: Experimental setup for highly-nondegenerate polarization entanglement generation in a dual-pumped bulk PPLN downconverter. Counter-propagating signal and idler photons are combined at the output to generate polarization entanglement.

pump at 532 nm laser downconverted inside the same PPLN crystal that was used for photon-pair generation. In contrast to the photon-pair generation scheme, the crystal was pumped in both the forward and backward directions. The horizontally polarized signal and idler fields in the forward direction were then combined with the vertically polarized signal and idler fields (after a $\pi/2$ polarization rotation) in the backward direction at the polarizing beam splitter. After the interferometric combination, the emerging output state is polarization-entangled. When post-selection is used, the output state of the bi-directional downconverter is in a non-factorizable joint signal-idler state

$$|\psi\rangle_{SI} = \alpha|H\rangle_S|V\rangle_I + \beta|V\rangle_S|H\rangle_I e^{j\phi}, \tag{2.1}$$

where $|H\rangle$ and $|V\rangle$ denote horizontally (H) and vertically (V) polarized signal (S) and idler (I) photons, $\phi = \phi_s + \phi_i + \phi_p$ is the net phase (pump, idler, and signal) determined by the source and the various path lengths, and $|\alpha|^2$ ($|\beta|^2 = 1 - |\alpha|^2$) is proportional to the overall efficiency for pair generation in the two paths and the subsequent propagation and coupling into the signal and idler fibers. Thus, when $|\alpha| = |\beta|$, Eq. 2.1 reduces to a maximally entangled state that is the equal superposition of a horizontally-polarized signal photon accompanied by a vertically-polarized idler plus a vertically-polarized signal photon accompanied by a horizontally-polarized idler. In this case both the signal and the idler photons are unpolarized, yet if we measure the polarization of one of them, we immediately know the polarization of its conjugate pair-photon with complete certainty.

In a manner similar to the the photon-pair generation experiment, the polarization-entangled signal and idler outputs were coupled into visible/near-infrared and SMF-28 single-mode fibers, respectively, for photon counting detection. We measured singles and coincidence counts with a commercial Si SPCM and with a custom-built InGaAs photon-counting detector module [27, 28]. The same 3^{rd} order PPLN crystal that was used for photon pair generation was now set at a temperature of ∼174°C for type-I downconversion of the 0.532 μm pump. After interferometric recombination of the two bi-directional outputs, as shown in Fig. 2-4, this setup generates polarization entanglement at ∼1.6 and 0.8 μm center wavelengths. The operating temperature of the PPLN crystal can be easily adjusted, thus allowing us to optimize the phasematched interaction and select different center wavelengths. The effective fiber-coupled idler bandwidth of the source was ∼60 GHz, corresponding to a photon time duration of ∼ 8.3 ps. Replacing the third-order PPLN crystal with a first-order grating of the same length would result in a pair production rate that is a factor of 9 higher, because the efficiency is proportional to the effective nonlinear coefficient squared. With this setup, we have measured quantum-interference visibilities greater than 90%. The main results are shown in Fig. 2-5 and more details can be found in the Ref. [32]. The output entangled state was not actively controlled resulting in a passive stability on the order of only several minutes. Active phase stabilization of the ϕ time-phase drift would be required to extend the temporal stability of this source. We have measured a violation of Bell's inequality in the CHSH form with $S = 2.606 \pm 0.010$ [32]. We note that classical and hidden variable theories limit S to less than 2, whereas quantum theory allows S as high as 2.828 for a maximally-entangled state. Although

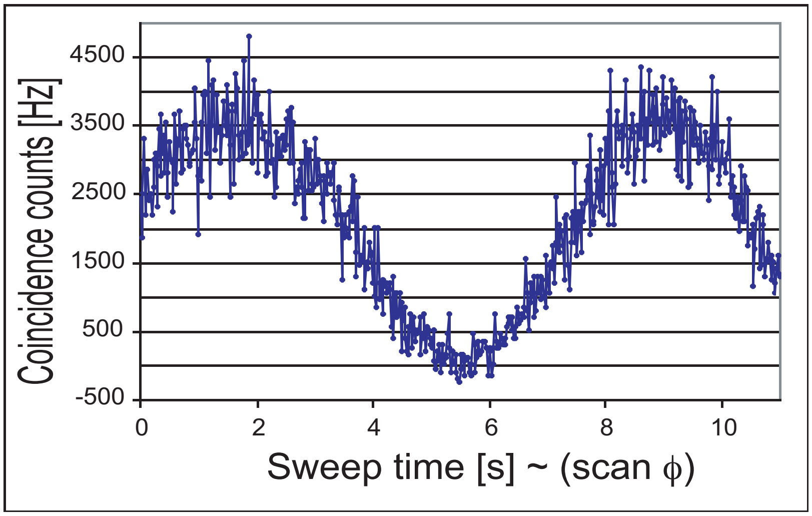

Figure 2-5: Quantum interference measured with the bi-directionally pumped PPLN SPDC: coincidence counts between downconverted signal and idler photons. The measured visibility is ∼90% and the passive stability of the output entangled state is on the order of a few minutes.

this source of polarization entanglement could be used to validate some aspects of the long distance quantum communication protocol, it is not stable enough to be useful for the demonstration of quantum-state frequency translation.

2.5 Photon Counting at 1.55 μm

Single-photon detection is required to demonstrate the nonclassical features of polarization-entanglement sources. Unfortunately, counting the 1.6-μm idler photons generated by our PPLN nondegenerate downconverter was difficult because of the lack of commercially available single-photon detectors at this wavelength. Although silicon-based single-photon counting modules (SPCMs), such as the PerkinElmer model SPCM-AQR-14, are commercially available, the band gap of the Si strictly limits their detection range to wavelengths below 1.1 μm. Photon counting detection at wavelengths beyond those reached by Si detectors has been demonstrated using superconducting structures [48]. However, the requirement of liquid-helium cooling for the operation of these devices has limited their real-world deployment. Another techniques for photon counting at 1.55 μm uses frequency upconversion followed by Si detection. This topic is the focus of Chapters 4 and 6. In the following section, we summarize the performance characteristics of our 1.55-μm single photon counters based on InGaAs APDs with custom-built electronics and cooling.

2.5.1 Geiger-Mode Avalanche Photodiodes for 1.55-μm Detection

Single-photon counting devices at infrared wavelengths in the S, C, and L telecom windows from 1.5 to 1.6 μm, employ InGaAs/InP or Ge APDs that are biased above the breakdown voltage, cooled, and operated in Geiger mode [24, 25, 26, 27, 28]. The reported efficiencies of these devices in this spectral region are generally in the 15 – 25% range, depending on the operating temperature and the associated trade-offs between dark counts, quantum efficiency, and counting rates. Typical devices are customized by researchers with a specific application in mind and, due to the inherent design trade-offs, they do not offer the flexibility needed in other experiments. Unlike their Si counterparts, room-temperature InGaAs/InP APDs are plagued by extremely high dark counts and afterpulses (due to the trapping and subsequent release of charge carriers) when they are over-biased to reach the photon-counting regime. To be useful as photon-counters, these complex semiconductor structures are typically cooled to liquid nitrogen temperatures. Because InGaAs/InP Geiger-mode APDs cannot be operated in continuous mode, due to severe afterpulsing, gated passively-quenched operation (with short-duration pulses) is typically used and the repetition frequency is typically limited to less than 100 kHz.

We built a compact, all-solid state, single-photon counter for 1.55 μm light using passively-quenched, gated, and entirely thermoelectrically (TE)-cooled InGaAs APDs. The overall design was a compromise between good quantum efficiency, low dark count probability, and sufficiently fast repetition rate, when operated at temperatures that can be achieved and long-term stabilized by Peltier elements. We also desired an unobtrusive package that can be used in bench-top optical experiments. A picture of two fiber-pigtailed custom counters inside a single cooling box is shown in Fig. 2-6.

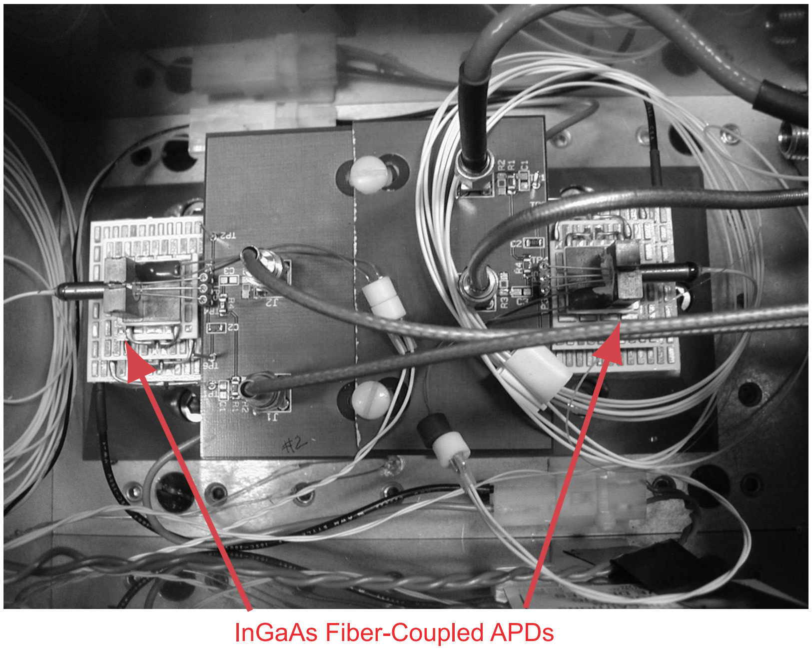

InGaAs Fiber-Coupled APDs

Figure 2-6: Two custom InGaAs photon counters inside a cooling box, showing the high-speed bias printed circuit boards and the cooling electronics.

When we cooled the counters to temperatures near -50°C, we obtained reliable photon-counting operation with quantum efficiencies of ∼20% at 1.55 μm, dark count probabilities of ∼0.16% per 20-ns gate, and negligible afterpulses at repetition rates of up to 200 kHz. In Fig. 2-7 we show selected data on the performance of these detectors in Geiger mode [28]. The data shown here are consistent with semiconductor device and Geiger-mode APD physics – dark counts increase exponentially with increasing device temperatures while the breakdown voltage increases linearly with temperature (at ∼1 V/°C). The dark count probability (per gate) is nearly constant over a wide gate repetition frequency range and shoots up when the contribution due to afterpulses begins to dominate, typically above 200 kHz at -60°C for the devices we tested, as shown in Fig. 2-7, panel d). In Fig. 2-8, we plot the two most important parameters for photon-counting operation, the quantum efficiency and the dark count probability (per 20-ns measurement interval). The data was collected as we increased the bias voltage. The operating conditions could be easily varied for optimal detection under different experimental conditions. If dark counts are the main concern, the temperature can be lowered to exponentially reduce this contribution. If a higher quantum efficiency is more important, larger over-biases should be used. Quantum efficiency or signal-to-noise constraints can be accommodated by controlling the operating temperature, bias voltage, gate width, and duty cycle. This setup can also be adapted to work with pulsed-laser experiments. An upgraded version of these single-photon counters was used in the first experimental implementation of the difference-beam entangled state [49]. More details on the construction and performance of these photon counters can be found in [28].

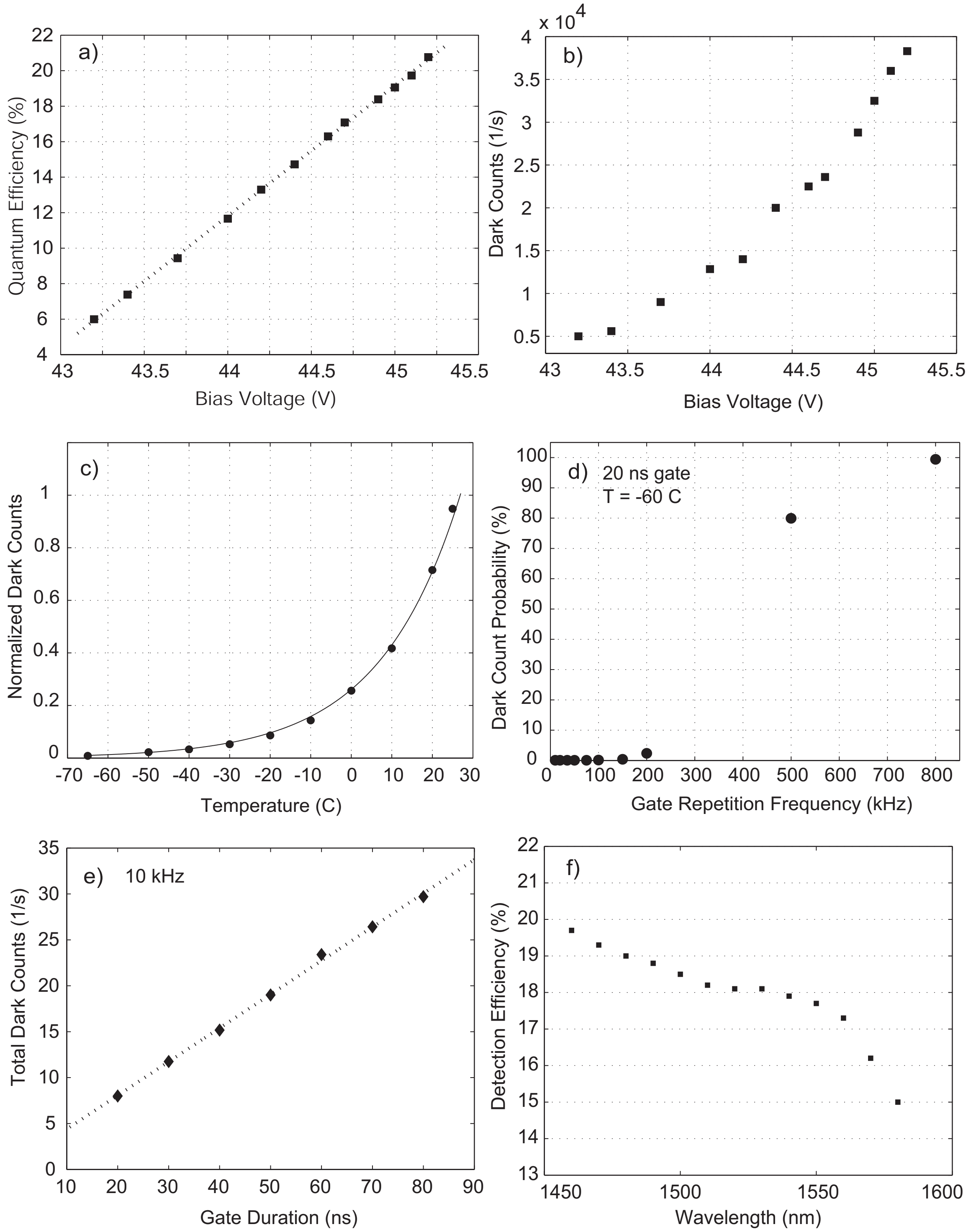

Figure 2-7: Typical behavior of the InGaAs/InP EPM239BA APD customized to operate in Geiger mode. a) QE vs. bias voltage and linear fit; b) total dark count rate vs. bias voltage; c) normalized dark count rate vs. temperature and exponential fit; d) dark count probability (per 20-ns gate) vs. gate repetition frequency; e) total dark counts vs. gate duration (at 10 kHz) and linear fit; f) detection efficiency versus wavelength. The detectors are passively quenched, gated in Geiger mode, and thermoelectrically-cooled to -50°C, except for d).

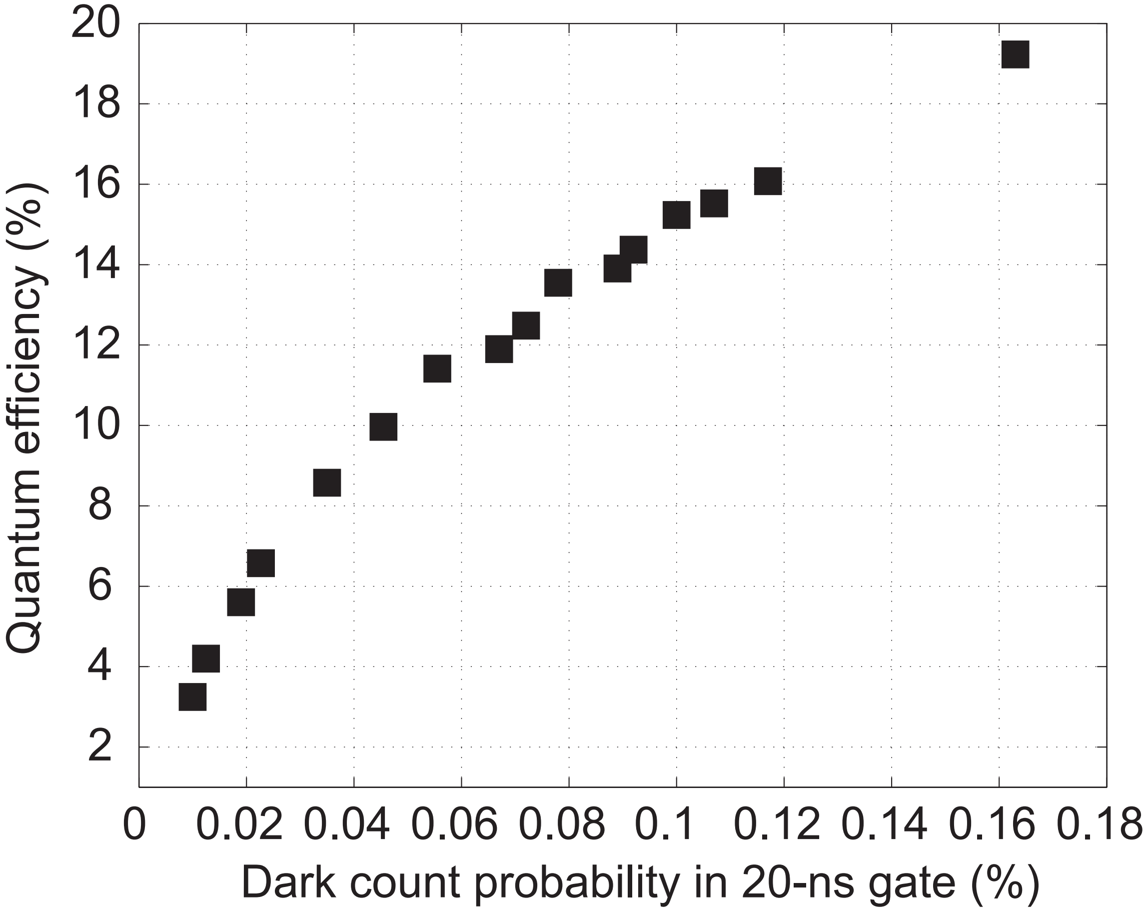

Figure 2-8: Quantum efficiency versus dark count probability in a 20-ns measurement interval. The performance is typical for our InGaAs photon counters at -50°C.

Chapter 3

Theoretical Considerations

Here we will review some theoretical underpinnings for our experimental work in quantum-state frequency conversion. We begin with the classical coupled-mode theory of sum-frequency generation in a $\chi^{(2)}$ crystal, including the use of periodic poling to achieve quasi-phase matching. This treatment connects naturally to the experimental work appearing in subsequent chapters because it includes Gaussian-beam focusing. We then present a fully-quantum coupled-mode analysis for plane-wave fields that shows the quantum-state preservation we are seeking.

3.1 Three-Wave Mixing in $\chi^{(2)}$ Nonlinear Crystals

The general process of three-wave mixing can be described by a set of three coupled classical wave equations. We are primarily concerned with the three-wave mixing interaction in which two lower-energy photons at ω_1 and ω_p combine into one higher-energy photon at ω_2. If the frequency ω_1 input field is weak with respect to the frequency ω_p pump, the process is known as upconversion from ω_1 to ω_2.

The induced material polarization can be written as

$$P_i \approx \chi_{ij}^{(1)} E_j + \chi_{ijk}^{(2)} E_j E_k + \cdots , \tag{3.1}$$

where $\chi^{(i)}$ are the material susceptibilities with $\chi^{(2)}$ being responsible for three-wave mixing processes, such as upconversion and downconversion, and $E_{j,k}$ are the relevant polarization components of the electric fields. It is standard practice to replace the three-dimensional susceptibility tensor $\chi^{(2)}$ with the effective nonlinear coefficient d_{eff} using the contracted notation [50]. The effective nonlinear coefficient contains all the information related to the strength and directionality of the crystal nonlinearity. Different values of d_{eff} can be selected depending on the propagation angle and, for various crystal classes, its value can be maximized for a given nonlinear interaction within the restrictions imposed by the phase-matching geometry.

The coupled differential equations that describe sum frequency generation are [50]:

$$\frac{dE_2}{dx} = -i\kappa_2 E_p E_1 e^{i\Delta kx} \tag{3.2}$$
$$\frac{dE_1}{dx} = -i\kappa_1 E_2 E_p^* e^{-i\Delta kx} \tag{3.3}$$
$$\frac{dE_p}{dx} = -i\kappa_p E_2 E_1^* e^{-i\Delta kx}\,, \tag{3.4}$$

where,

$$\kappa_j = \frac{\omega_j d_{\text{eff}}}{n_j c} \tag{3.5}$$

(for $j = 1, 2$ and p) are the coupling coefficients written in terms of the respective frequencies and indices of refraction, and $\Delta k = k_2 - k_1 - k_p$ is the wave-number (phase) mismatch. The derivation of Eqs. (3.2)-(3.4), invokes the standard slowly-varying envelope approximation, + x -going plane-wave interactions with negligible absorption, and propagation in a purely non-magnetic crystalline media with a nonvanishing $\chi^{(2)}$. Required for efficient nonlinear interactions are the following two conditions. First, energy conservation requires that these fields' frequencies obey $\omega_1 + \omega_P = \omega_2$. Secondly, momentum conservation requires $\Delta k = k_2 - k_1 - k_p = 0$. In the low conversion limit, with an undepleted pump, we take the input pump and weak probe fields, E_p and E_1, as constants and obtain the following expression for the amplitude E_2 of the upconverted signal for a crystal of length L,

$$E_2(\omega_2, L) = -i\kappa_2 E_p E_1 L \mathrm{sinc}[\frac{\Delta \mathrm{kL}}{2}] \mathrm{e}^{\mathrm{i}\frac{\Delta \mathrm{kL}}{2}}, \tag{3.6}$$

where $\mathrm{sinc(x)} = \frac{\sin(\mathrm{x})}{\mathrm{x}}$ is the phase-matching function – a measure of phase synchronization or lack thereof between the interacting fields. In terms of intensity, with $I = (1/2)n\sqrt{\frac{\epsilon_o}{\mu_o}}|E|^2$, we have

$$I_2(\omega_2, L) = \frac{2\omega_2^2 d_{eff}^2}{n_p n_1 n_2 c^3 \epsilon_o} L^2 I_p I_1 \mathrm{sinc}^2[\frac{\Delta \mathrm{kL}}{2}]. \tag{3.7}$$

The efficiency of the upconversion process is given by the ratio of the upconverted power to the input probe power, where $P = IA$ and the effective area for a Gaussian beam of radius w in the near-field limit is $A = \frac{1}{2}\pi w^2$. For perfect phase matching, $\Delta k = 0$, the single-pass upconversion efficiency can be written as

$$\eta = \frac{P_2}{P_1} = \frac{16\pi d_{eff}^2 P_p w_2^2 L^2}{n_p n_1 n_2 c \epsilon_o \lambda_2^2 w_p^2 w_1^2}. \tag{3.8}$$

We note that the conversion efficiency is proportional to d_{eff}^2 and it depends linearly on P_p. In near-field analysis it was shown [51] that in order to minimize the parametric threshold of the interation and for optimal conversion efficiency one must have

$$\frac{1}{w_2^2} = \frac{1}{w_p^2} + \frac{1}{w_1^2}. \tag{3.9}$$

We make this substitution, insert the confocal beam parameters inside the crystal $b_j = \frac{2\pi w_j^2 n_j}{\lambda_j}$ (which we set equal to each other), and introduce the efficiency reduction factor [51] for Gaussian-beam interactions $L/b \Rightarrow h_m(B, \zeta)$ to obtain the following useful expression for the upconversion efficiency

$$\eta = \frac{P_2}{P_1} = \frac{16\pi d_{eff}^2 P_p L}{n_p n_1 n_2 c \epsilon_o \lambda_2^2} \frac{h_m(B, \zeta)}{k_p^{-1} + k_1^{-1}}, \tag{3.10}$$

where B is the walk-off parameter (B ∼0 for quasi-phase matching). The values of the efficiency reduction factor $h_m(B, \zeta)$ must be computed numerically for various focusing conditions. Optimal upconversion requires $\zeta \sim 2.84$ and $B = 0$ and results in a peak value for h_m of 1.068 [51]. For non-ideal but experimentally realizable focusing with $L/b \sim 1$, the efficiency reduction factor is ∼0.776.

For quasi-phase-matched (QPM) interactions in periodically poled media, the preceding analysis applies, but with the effective nonlinear coefficient written as

$$d_m = \frac{2}{m\pi} \mathrm{sin(m\pi D)d_{eff}}, \tag{3.11}$$

where D is the grating duty cycle and m is the order of the QPM grating [41]. The maximum useful value for d_m occurs for $m = 1$ and $D = 0.5$, resulting in a value of the nonlinear coefficient that is ∼63.7% or $\frac{2}{\pi}$ of d_{eff}.

Conventional birefringent phase matching, $\Delta k = 0$, is achieved when the following condition is satisfied

$$\frac{n_2(\lambda_2)}{\lambda_2} = \frac{n_1(\lambda_1)}{\lambda_1} + \frac{n_p(\lambda_p)}{\lambda_p}. \tag{3.12}$$

QPM is achieved by introducing a compensating vector, $K_m = 2\pi m/\Lambda$ such that Δk vanishes, where Λ is the grating period of a domain-reversed unit cell in the periodically-poled structure. For the case of type-I phase matching, E_1, E_2, and E_p are all collinearly polarized and oriented along the extraordinary crystal axis, and the quasi-phase-matching condition becomes

$$\frac{n_e(\lambda_2, T)}{\lambda_2} = \frac{n_e(\lambda_1, T)}{\lambda_1} + \frac{n_e(\lambda_p, T)}{\lambda_p} \pm \frac{m}{\Lambda}, \tag{3.13}$$

where $n_e(\lambda_j, T)$ is the extraordinary index of refraction of the material given by the Sellmeier equations [52, 53].

3.2 Theory of Quantum-State Frequency Conversion

The quantum-mechanical version of the upconverter's coupled-mode equations and their solutions are summarized below. For convenience, we use photon-units fields

A_1 and A_2 instead of electric fields E_1 and E_2. Because of zero-point fluctuations, we cannot treat the quantum versions of A_1 and A_2 as monochromatic. Thus for a nonlinear crystal located at $0 \leq x \leq L$, we take $\{A_1(0,\omega), A_2(0,\omega)\}$ to be the classical input and upconverted fields at detuning ω, from ω_1 and ω_2 respectively, at the crystal's input facet. We then replace these classical fields with with field operators $\{\hat{A}_1(0,\omega), \hat{A}_2(0,\omega)\}$ that satisfy the canonical commutation relations,

$$[\hat{A}_j(0,\omega), \hat{A}_k(0,\omega')] = 0 \quad \text{and} \quad [\hat{A}_j(0,\omega), \hat{A}_k^\dagger(0,\omega')] = 2\pi\delta_{jk}\delta(\omega-\omega'), \quad \text{for } j,k = 1,2, \tag{3.14}$$

where $\hat{A}_j^\dagger(0,\omega)$ is the adjoint operator associated with $\hat{A}_j(0,\omega)$. Physically, $\hat{A}_j(0,\omega)$ annihilates a photon at frequency $\omega_j + \omega$ photon at $x = 0$, and $\hat{A}_j^\dagger(0,\omega)$ creates a photon at frequency $\omega_j + \omega$ at this location. The non-zero commutators for $\{\, \hat{A}_j(0,\omega), \hat{A}_j^\dagger(0,\omega') \,:\, j = 1,2 \,\}$ lead, via the Heisenberg uncertainty principle, to the existence of quantum noise on these light beams. Because the signal and upconverted fields at the crystal's output facet ($x = L$) must satisfy the same Heisenberg uncertainty principle, the quantum treatment of the upconverter must preserve commutator brackets. We assume colinear, collimated-beam propagation (constant cross-sectional area $\mathcal{A}$) with no pump depletion and perfect phase matching for upconversion from ω_1 to ω_2. The quantum coupled-mode equations for this system then have the following form for $0 \leq x \leq L$:

$$\frac{\partial}{\partial x}\hat{A}_2(x,\omega) = i\kappa A_P \hat{A}_1(x,\omega) e^{-i\omega\Delta k' x} \tag{3.15}$$

$$\frac{\partial}{\partial x}\hat{A}_1(x,\omega) = i\kappa A_P^* \hat{A}_2(x,\omega) e^{i\omega\Delta k' x}, \tag{3.16}$$

where

$$\kappa \equiv \sqrt{\frac{\hbar\omega_P\omega_1\omega_2}{2c^3 n_P n_1 n_2 \epsilon_0 \mathcal{A}}}\,\chi^{(2)} \tag{3.17}$$

is the nonlinear coupling coefficient, A_P is the classical pump field, and

$$\Delta k' \equiv \frac{\mathrm{d}}{\mathrm{d}\omega}[k_2(\omega_2 + \omega) - k_1(\omega_1 + \omega)]\Big|_{\omega=0} \tag{3.18}$$

quantifies the phase mismatch at detuning ω, with n_1, n_P, and n_2 being the refractive indices for the input, pump, and upconverted fields at frequencies ω_1, ω_P, and ω_2, respectively. Solving (3.15) and (3.16) we find that the field operators at the crystal's output facet are,

$$\begin{aligned}\hat{A}_2(L,\omega) &= \left(\cos(qL) + i\frac{\omega\Delta k' L}{2}\frac{\sin(qL)}{qL}\right) e^{-i\omega\Delta k' L/2}\hat{A}_2(0,\omega) \\ &\quad + i\kappa A_P L\frac{\sin(qL)}{qL}e^{-i\omega\Delta k' L/2}\hat{A}_1(0,\omega) \qquad (3.19) \\ \hat{A}_1(L,\omega) &= \left(\cos(qL) - i\frac{\omega\Delta k' L}{2}\frac{\sin(qL)}{qL}\right) e^{i\omega\Delta k' L/2}\hat{A}_1(0,\omega) \\ &\quad + i\kappa A_P^* L\frac{\sin(qL)}{qL}e^{i\omega\Delta k' L/2}\hat{A}_2(0,\omega) \qquad (3.20)\end{aligned}$$

where

$$q \equiv \sqrt{(\kappa|A_P|)^2 + (\omega\Delta k'/2)^2}. \qquad (3.21)$$

It is easily verified that these solutions preserve commutator relations. Unlike the classical situation, in which it is possible to have a field value of zero, quantum field operators cannot be dismissed even if they are associated with unexcited fields. This is because an unexcited field is in its vacuum state, and the vacuum state carries quantum noise (zero-point fluctuations) that can affect photodetection sensitivity. As a result, we cannot automatically ignore the $\hat{A}_2(0,\omega)$ terms in these solutions.

Equations (3.19) and (3.20) show that when the pump obeys

$$|A_P| = A_{\pi/2} \equiv \pi/2\kappa L, \qquad (3.22)$$

the upconverter will achieve perfect quantum-state frequency translation, from frequency ω_1 to ω_2, i.e. at zero detuning, except for a physically unimportant phase shift. This is because at pump strength $A_{\pi/2}$ we have

$$\hat{A}_2(L,0) = i\frac{A_P}{|A_P|}\hat{A}_1(0,0). \qquad (3.23)$$

Quantum-state frequency translation is imperfect at non-zero detuning ($\omega \neq 0$), even when $|A_P| = A_{\pi/2}$, because dispersion makes $q > \kappa|A_P|$. However, for operation well within the phase-matching bandwidth, Eq. (3.19) does yield near-perfect upconversion when $|A_P| = A_{\pi/2}$. In particular, when $|\omega| \ll 1/|\Delta k'|L$ we get $q \approx \kappa|A_P|$ and

$$\hat{A}_2(L,\omega) \approx \cos(\kappa|A_P|L)\hat{A}_2(0,\omega) + i\frac{A_P}{|A_P|}\sin(\kappa|A_P|L)\hat{A}_1(0,\omega), \tag{3.24}$$

which becomes

$$\hat{A}_2(L,\omega) \approx i\frac{A_P}{|A_P|}\hat{A}_1(0,\omega) \tag{3.25}$$

when $|A_P| = A_{\pi/2}$. Except for an unimportant absolute phase, the output field operator (under these ideal conditions) will be in the same quantum state as the input field operator.

3.3 Experimental Conditions for Near-Unity Upconversion

To better relate the preceding theory for quantum-state frequency conversion to our experiments, we will now make some simplifications that tie the results of Section 3.2 back to those of Section 3.1.

In particular, by suppressing the absolute phase term in Eq. 3.24, using the MKS-units expression $g|E_p|$ with $g = \sqrt{\kappa_1\kappa_2}$ in lieu of $\kappa|A_p|$, and focusing on the annihilation operators for narrowband single-mode fields at frequencies ω_1 and ω_2 we get the input-output relations

$$\begin{aligned} \hat{a}_1(L) &= \cos(|gE_p|L)\hat{a}_1(0) - \sin(|gE_p|L)\hat{a}_2(0)\,, & (3.26)\\ \hat{a}_2(L) &= \sin(|gE_p|L)\hat{a}_1(0) + \cos(|gE_p|L)\hat{a}_2(0)\,. & (3.27) \end{aligned}$$

We see that the average photon numbers of the frequency ω_1 and ω_2 fields at the crystal's output facet exhibit Rabi-type oscillations according to

$$N_2(L) = \langle \hat{a}_2^\dagger(L)\hat{a}_2(L)\rangle \quad = \quad N_1(0)\sin^2(|\mathrm{gE_p}|\mathrm{L}) \tag{3.28}$$

$$N_1(L) = \langle \hat{a}_1^\dagger(L)\hat{a}_1(L)\rangle \quad = \quad N_1(0)\cos^2(|\mathrm{gE_p}|\mathrm{L})\,, \tag{3.29}$$

where $N_1(0) = \langle \hat{a}_1^\dagger(0)\hat{a}_1(0)\rangle$. The behavior of these average photon numbers is illustrated in Fig. 3-1. Frequency translation of any quantum state at ω_1 to the same quantum state at ω_2 with unity efficiency is possible, even at the single-photon level, if $g|E_p|L = \pi/2$.

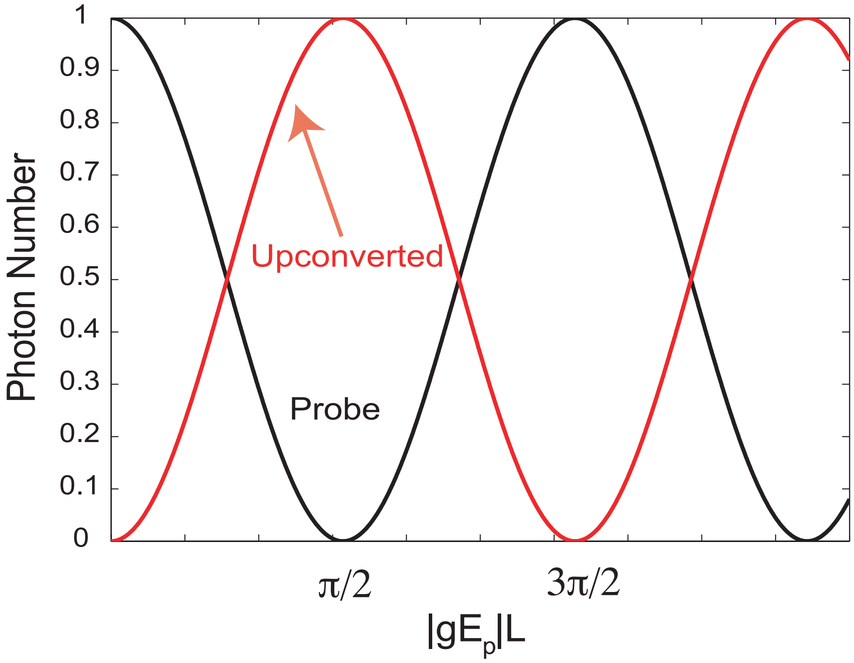

Figure 3-1: Probe and signal photon numbers. Unity conversion occurs for $|gE_p|L = \pi/2$.

The sum-frequency generation technique is characterized by the upconversion efficiency $\eta = N_2(L)/N_1(0)$, which can be written functionally as

$$\eta = \sin^2\left[(\pi/2)\sqrt{P_p/P_{\max}}\right], \tag{3.30}$$

where P_p is the input pump power to the nonlinear crystal and $P_{\max}$ is the pump power required to achieve unity conversion efficiency. For 100% upconversion efficiency using

Gaussian optics, we need

$$g|E_p|L = \frac{\pi}{2}, \tag{3.31}$$

where,

$$g = \sqrt{\kappa_1\kappa_2} = \frac{d_{eff}}{c}\sqrt{\frac{\omega_1\omega_2}{n_1n_2}}. \tag{3.32}$$

We introduce the intensity of the pump power via

$$I_p = \frac{P_p}{(1/2)\pi w_p^2} = \frac{n_pc\epsilon_o|E_p|^2}{2}, \tag{3.33}$$

and express the pump field as a function of pump power

$$|E_p|^2 = \frac{4P_p}{\pi n_pc\epsilon_o w_p^2}. \tag{3.34}$$

With these substitutions, the condition for 100% upconversion efficiency (3.31) becomes

$$(\frac{d_{eff}}{c})^2\frac{\omega_1\omega_2}{n_1n_2}\frac{4P_p}{\pi n_pc\epsilon_o w_p^2}L^2 = (\frac{\pi}{2})^2. \tag{3.35}$$

Solving Eq. 3.35 for P_p by introducing the the confocal beam parameter of the pump inside the crystal and the efficiency reduction parameter for Gaussian-beam interactions as done before, we obtain the final expression for $P_{\max}$ [35]

$$P_{\max} = \frac{c\epsilon_0n_1n_2\lambda_1\lambda_2\lambda_p}{128d_{\text{eff}}^2L\bar{h}_m(B, L/b_p)}\,. \tag{3.36}$$

Chapter 4

Frequency Upconversion

4.1 Frequency Conversion for High-Efficiency Photon Counting and Optical Communication

In this Chapter we report efficient polarization-selective upconversion. Although this basic idea was demonstrated for squeezed states of light, [54] it was only recently implemented for single photons [34, 35]. We also discuss an interesting application of near-unity upconversion in photon counting. We report high-performance single-photon detection at 1.55 μm via sum-frequency generation followed by direct detection in the visible with a Si SPCM. Owing to the many problems and limitations of using Geiger-mode InGaAs APDs as 1.55 μm photon counters, this cascaded approach to photon counting at 1.55 μm has great application potential. Indeed, it can help QKD systems achieve higher key rates and it can also improve interplanetary optical communications, as both of these applications may be driven to 1.55 μm operation by loss considerations (for fiber propagation in QKD) or transmitter technology (for interplanetary optical communications).

4.1.1 Periodically Poled Lithium Niobate for Frequency Upconversion

In this section, we describe a study of the near-unity upconversion efficiency that is desired for quantum-state frequency upconversion. The purpose of these experiments was to test the feasibility of high-performance upconversion in a bulk PPLN crystal, derive and measure the relevant crystal and laser parameters, and investigate any factors that might limit the applicability of this technique. We designed and fabricated in house a 6 mm (L) × 0.5 mm (T) × 14 mm (W) PPLN crystal with an 11.6-μm target grating period. This crystal allows 1st order type-I quasi phase matched sum-frequency generation of $\sim$640 nm (signal) from inputs at 1064.2 nm (pump) and 1.609 μm (probe). These wavelengths are tunable. With a slight change in the PPLN temperature, we can achieve sum-frequency generation at $\sim$631 nm from a 1064.2 nm pump and 1.55 μm probe. The process of frequency upconversion is illustrated in Fig. 4-1. As discussed previously, QPM in PPLN is the technique of choice for efficient frequency down as well as upconversion. Here, we note that by

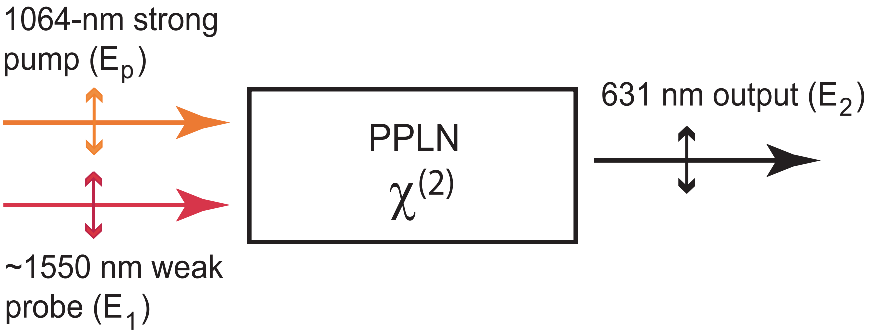

Figure 4-1: Sum frequency generation in a $\chi^{(2)}$ periodically poled nonlinear crystal such as PPLN. The input and output beams are co-polarized, as required by type-I QPM. The wavelengths are tunable via a change in the crystal temperature or grating period.

employing type-I noncritical phase matching in PPLN we access one of the highest nonlinear coefficients of all inorganic media, the d_{33} of lithium niobate ($LiNbO_3$) over a wide transmission band, from ∼0.4 to ∼4 μm.

The $LiNbO_3$ bulk sample was sliced out of a 3-inch-diameter optical grade z-cut wafer made by Crystal Technology Inc. The photolithographic grating mask was designed using AutoCad and was produced to our specifications by DuPont Photomasks Inc. We fabricated the PPLN using standard electric field poling techniques [41, 42, 46] and the fabrication methods developed by Mason [47]. The extraordinary refractive index of congruent $LiNbO_3$ as a function of wavelength at two different temperatures is shown in Fig. 4-2. A theoretical calculation showing the required grating period as a function of temperature for optimal phase matching at the wavelengths of interest is shown in Fig. 4-3. The curves are computed from the temperature-dependent Sellmeier equations [53] and include the thermal expansion of congruently grown $LiNbO_3$ at elevated temperatures. We chose to operate near 200°C in order

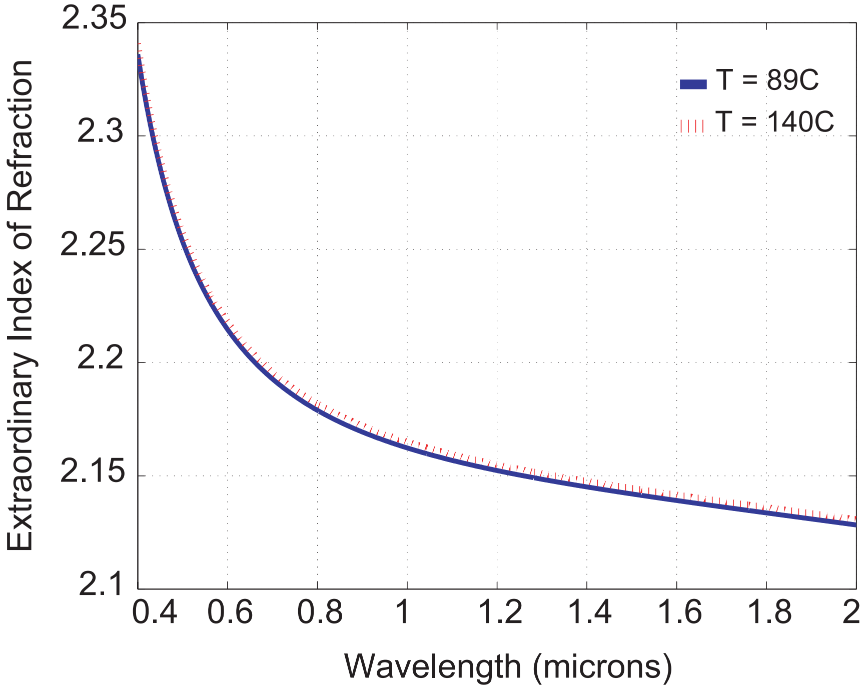

Figure 4-2: Calculated extraordinary refractive index, $n_e(\lambda, T)$, of lithium niobate plotted as a function of wavelength at two temperatures. Data are computed from the Sellmeier equations published in Ref. [53].

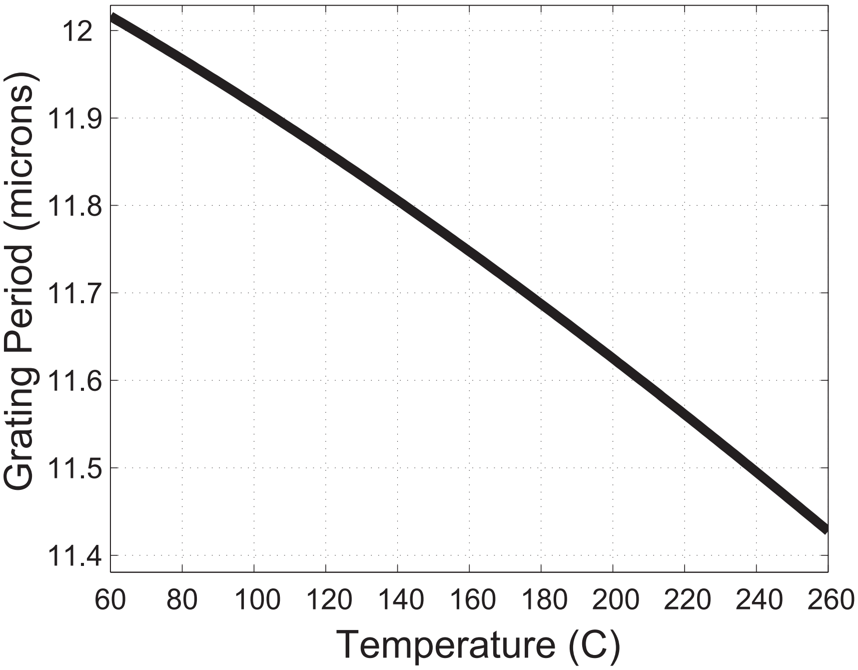

Figure 4-3: Optimum PPLN grating period for quasi-phase matched sum-frequency generation versus crystal temperature.

to avoid photorefractive damage due to the high pump powers at 1.064 μm that would eventually be needed to achieve near-unity frequency conversion. The temperature of the PPLN can be controlled reliably near these elevated temperatures using commercial heaters with an accuracy of ±0.1°C. We selected for the PPLN design a target grating with a period of 11.6 μm corresponding to an operating temperature of 208°C. Using this PPLN crystal, upconversion of 1.609 μm light using a strong pump at 1.064 μm resulted in a sum-frequency signal at 640 nm, near the peak of the Si detection window. The versatility of the upconverter could be further expanded by using a multi-grating PPLN crystal.

The 1600-nm probe light was chopped at ~460 Hz with an EGG 196 Light Chopper. We employed lock-in detection of the weak upconversion signal using a Stanford Research Systems 650 filter and lock-in amplifier (SRS Model 830). Figure 4-4 shows the temperature phase matching curve for the crystal. The upconversion data agrees very well with theory. We see clear evidence of phase matching and the data follows closely the sinc^2 shape predicted by theory. The FWHM temperature bandwidth is approximately 6.3°C, and the optimal crystal temperature corresponding to the

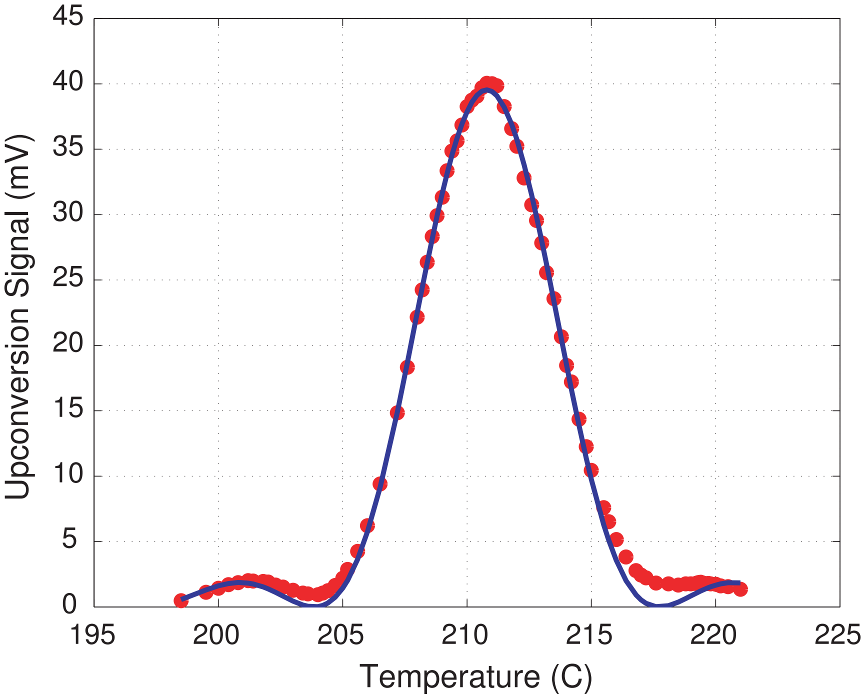

Figure 4-4: Upconversion signal as a function of crystal temperature (dots) and sinc^2 fit (solid line) for 6-mm PPLN. The FWHM temperature bandwidth is 6.3°C.

probe wavelength of 1.609 μm was found near ∼211°C. Using the values reported by Jundt [53], we computed a theoretical phase-matching temperature of ∼208°C. The observed temperature shift in the peak of the phase matching function from design specifications is only 3°C. From the Sellmeier equation we calculated that, for a nominal 6-mm-long crystal, a FWHM temperature bandwidth of 6.2°C was expected. From the FHWM bandwidth of the experimental data shown in Fig. 4-4, we inferred an effective nonlinear interaction length of ∼5.8 mm. This suggests that phase matching occurred over ∼96% of the 6-mm physical length of the crystal. Figure 4-5 shows the dependence of the upconverted light on the pump power in the weak-conversion regime. Again, the experimental data agrees very well with theory - a linear dependence of the upconversion on pump power is expected. When pumping the crystal with the maximum available power from the Nd:YAG laser, which was on the order of 332 mW, we achieved a single-pass conversion efficiency of 0.65%. This value was in good agreement with theoretical predictions, within∼15%. Using the 5.8 mm effective interaction length and the experimentally measured conversion effi-

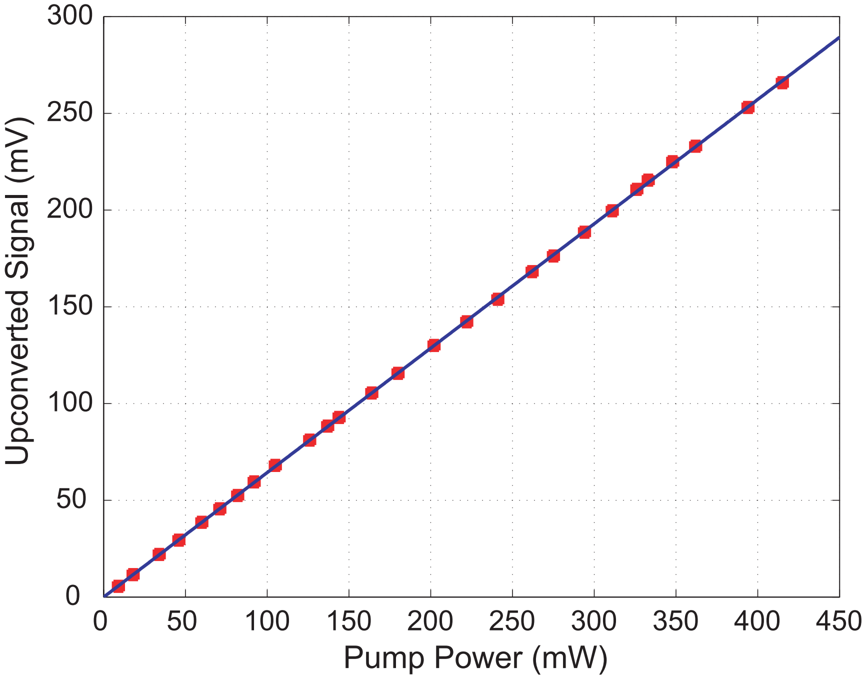

Figure 4-5: Upconversion signal versus pump power (squares) and theoretical fit (solid line). The phase matching temperature was 191.6°C and the probe wavelength for this measurement was tuned to 1601.88 nm.

ciency, we infer that d_{eff} ~14.6 pm/V. These measurements confirmed the feasibility of our upconversion scheme based on bulk PPLN. Our method for achieving near-unity-efficiency frequency upconversion and efficient 1.55-μm single photon counting is described in the following sections.

4.1.2 Analysis of Cavity-Enhanced Frequency Upconversion

As shown in Chapter 3, the sum-frequency generation technique is characterized by the upconversion efficiency $\eta = N_2(L)/N_1(0)$, that obeys

$$\eta = \sin^2\left[(\pi/2)\sqrt{\frac{P_p}{P_{\max}}}\right] , \tag{4.1}$$

when pump depletion and phase mismatch are neglected. In this equation P_p is the input pump power to the nonlinear crystal, and $P_{\max}$ is the pump power required to achieve unity conversion efficiency:

$$P_{\text{max}} = \frac{c\epsilon_0 n_1 n_2 \lambda_1 \lambda_2 \lambda_p}{128 d_{\text{eff}}^2 L \bar{h}_m(B, L/b_p)}\,, \tag{4.2}$$

where $\bar{h}_m$ is the reduction factor for focused Gaussian beams with a double refraction parameter $B = 0$ and a focusing parameter L/b_p, with b_p being the confocal parameter for the mode-matched interaction [40, 51]. For $\lambda_{1,2,p} = 1.548, 0.631$, and 1.064 μm, respectively, and using 1st order QPM in PPLN with $d_{\text{eff}} \approx 14$ pm/V, and $L/b_p = 1$ (yielding $\bar{h}_m = 0.776$), we estimate that the required pump power for 100% single-pass conversion efficiency is $P_{\text{max}} \approx 17\,\text{W}$ [27]. We have chosen the output wavelength at ~ 0.632 nm purely on the basis of convenience, in order to facilitate optical alignment and calibration with a HeNe laser. However the single-photon upconversion technique could also be implemented at other wavelengths of choice, including the 795-nm Rb absorption line, by using a different pump laser, PPLN grating period, and phase matching temperature.

4.2 Near-Unity Efficiency Upconversion Scheme

The experimental investigation reported in Section 4.1.1 was a useful test run designed to ascertain the basic idea of upconversion in PPLN. From that analysis we determined that in order to achieve near-100% conversion efficiency in a bulk material significantly more pump power (> 15 W) and longer nonlinear crystals (> 2 cm) are required. We decided that a good way to increase the power is by resonating the pump inside an optical cavity. With this scheme, we estimated that an input pump power of ∼400 mW would require a cavity enhancement factor of ∼43 to achieve the circulating power level necessary for unity upconversion. This level of power enhancement can be realized with a relatively low finesse ring cavity. Bulk PPLN crystals of improved quality and increased length have lately become commercially available, from companies such as HC Photonics. Longer 1st order PPLN crystals with a better effective nonlinear coefficient would further lower the constraints on the pump power necessary for high-efficiency upconversion.

We chose to implement the frequency conversion scheme in a 40 mm (L) × 5.1 mm (W) × 0.5 mm (T) bulk, congruently-grown, PPLN crystal purchased from HC Photonics. The 5.1-mm-wide crystal had 6 gratings, ranging from 11 to 12 μm in 0.2 μm steps. Each grating channel was 0.8-mm-wide, and the gap between the gratings was 0.06 mm. The crystal's faces were triple anti-reflection coated at the pump, input, and output wavelengths by VLOC. Figure 4-6 shows a picture of two PPLN crystals used in the upconversion experiments with the six gratings visible. Figure 4-7 shows a close-up picture of one of the PPLN crystals as viewed through a microscope. The periodically poled domains are clearly visible. There is evidence of poling nonuniformity (the domains are not regular), which could account for the less-than-maximum nonlinear optical coefficient of the crystal. The multi-grating PPLN design allowed the upconverter to work with a wide range of input wavelengths. Together with a temperature tuning range of 140–230°C and at a fixed pump wavelength (λ_p), this setup can accommodate any input wavelength (λ_1) in the 1.52 to 1.66 μm range, thus covering

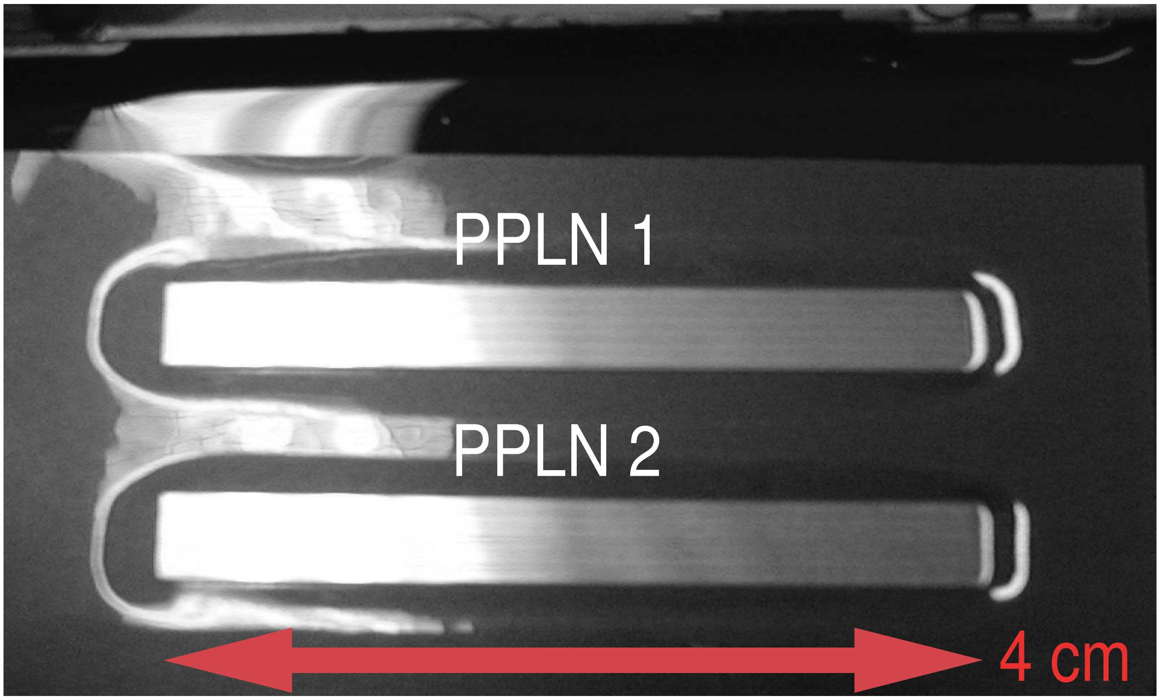

Figure 4-6: Picture of two 4-cm long congruently-grown PPLN crystals used in the near-unity upconversion experiments.

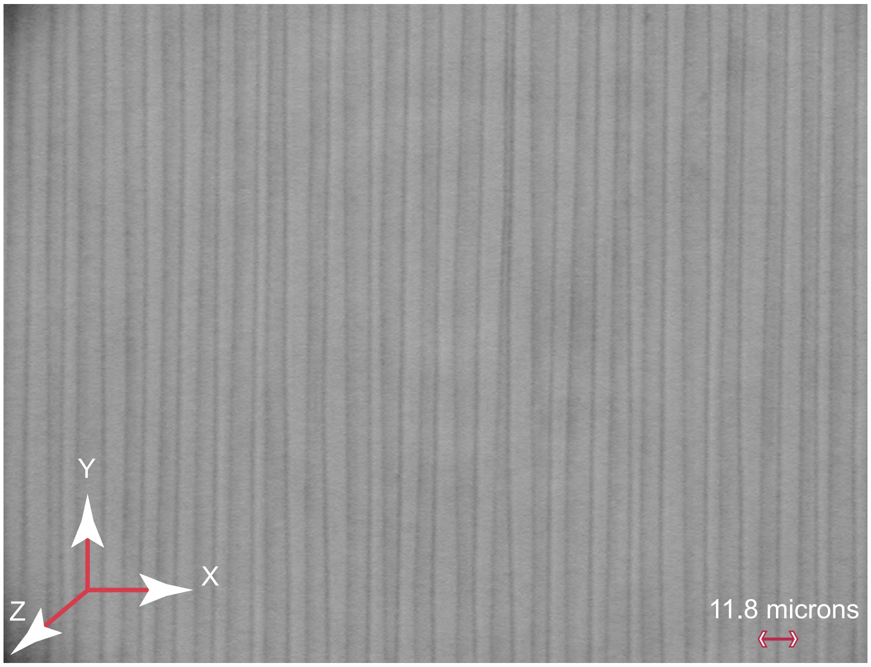

Figure 4-7: Mircroscopic view of the inverted domains on a single PPLN grating, showing some poling nonuniformity.

the C and L communication bands in their entirety. The measured PPLN temperature tuning coefficient was ∼0.35 nm/°C, with the optimal input probe wavelength increasing with increasing crystal temperature. We housed the 40-mm-long PPLN crystal in an oven (Super Optronics) set at ∼197.4°C. This temperature allowed for first-order, type-I, quasi-phase matched sum-frequency generation of $\lambda_2 = 631$ nm (signal) from inputs at $\lambda_1 = 1548$ nm (probe) and $\lambda_p = 1064$ nm (pump). The oven was controlled to within ±0.1°C, which is less than the PPLN temperature phase-matching bandwidth of 1°C. Therefore, the thermal fluctuations due to the oven were small enough and did not affect the long term operational stability of the upconverter.

We measured the dependence of the output signal on the input probe wavelength at a fixed pump power. In Fig. 4-8 we show wavelength tuning curve for the 11.2-μm grating of the crystal. The oven temperature was set at 228.8°C and the wavelength ranged from 1560.2 nm to 1561.6 nm. The experimental data agrees well with theory - there is clear evidence of phase matching as the tuning curve displays the expected sinc^2 shape predicted by theory. From the data we infer that d_{eff} ∼13.7 pm/V for this PPLN crystal. The FWHM wavelength phase-matching bandwidth is ∼0.3 nm,

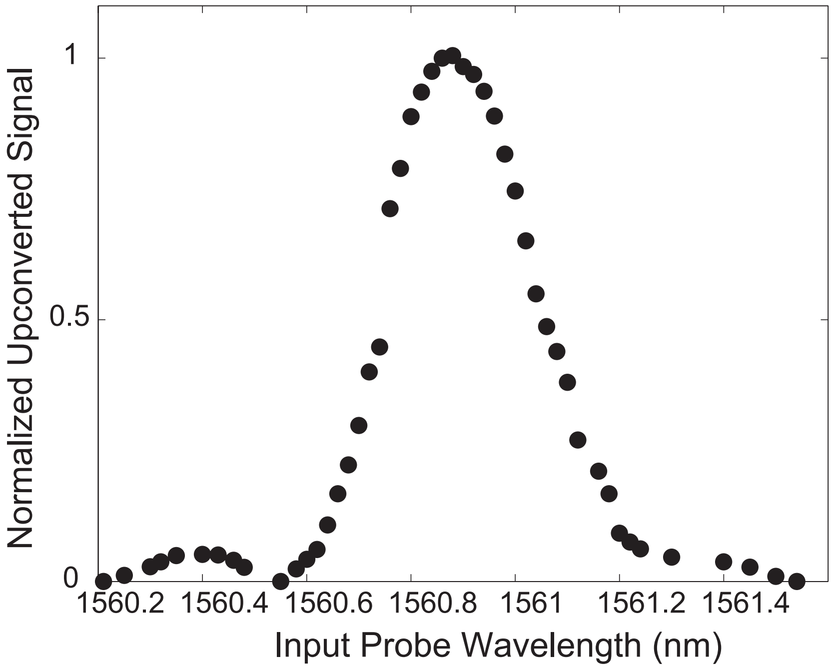

Figure 4-8: Output signal tuning bandwidth at a PPLN temperature of 228.8°C (FWHM bandwidth is ∼0.3 nm). The optimum probe wavelength for this grating at this temperature is ∼1560.9 μm.

in excellent agreement with the theoretical bandwidth for a 4-cm PPLN computed from the Sellmeier equations [53]. This corresponds to a frequency bandwidth of $\Delta\nu = \nu\lambda^{-1}\Delta\lambda \sim 37.5$ GHz, and a pulse width of $\Delta\tau_{UP} \approx \frac{1}{2}(\Delta\nu)^{-1} = 13.3$ ps.

4.2.1 Weak Probe Upconversion

We used a cw Nd:YAG laser (Lightwave Electronics Series 122) operating at 1064.2 nm and capable of 400-mW maximum output power as the pump. In order to implement our high-efficiency upconversion scheme in bulk PPLN using this relatively low power laser, we needed to resonate the cw pump inside a ring cavity. We used ABCD-matrix formalism [55] to design an optical setup with the proper beam radii of curvature (R) and waists (w_o) for the two input laser beams as well as for collecting the output light. The probe beam inside the PPLN was a TEM$_{00}$ Gaussian with a waist of ∼67 μm. The pump focus at the center of the crystal had a beam waist of ∼55 μm midway between the curved mirrors (with ∼10% difference between the sagittal and tangential waists). The corresponding confocal parameters for the pump and probe are given by $b = 2\pi n w_o^2/\lambda_o$, where λ_o is the vacuum wavelength, n is the extraordinary refractive index of the PPLN at λ_o, and w_o is the beam waist radius. These confocal beam parameters resulted in a value for L/b of ∼1 ($\hbar_m$ ∼0.776) which we set to be equal for both the probe and pump beams. We mode matched the confocal parameters of the two input lasers to the effective confocal parameter of the ring cavity. The characteristic length f_o is defined by the two effective waists, or, alternatively, by the two b-parameters, via (in free space)

$$f_o = \pi w_1 w_2/\lambda = 1/2\sqrt{b_1 b_2}. \tag{4.3}$$

Any simple lens with a focal length $f > f_o$ can be used to perform the matching transformation. Once f is chosen, the distances d_1 and d_2 between the chosen lens and the two effective beam waists must be adjusted as to satisfy the following relations [55]

$$d_1 = f \pm \frac{w_1}{w_2}\sqrt{f^2 - f_o^2}, \tag{4.4}$$

$$d_2 = f \pm \frac{w_2}{w_1}\sqrt{f^2 - f_o^2}. \tag{4.5}$$

The design parameters for the entire optical system were confirmed with actual beam-parameter measurements at several points along the propagation path. These measurements were performed with a beam scanner (Photon Inc.) with excellent fit to theoretical Gaussian-propagation curves. The cavity was single-pass for the input probe and output signal in order to minimize the insertion loss. This scheme is capable of both cw and pulsed upconversion, if the pulse bandwidth is smaller than the PPLN phase-matching bandwidth. The cavity configuration was also desirable because it imposed a well-defined spatial mode that simplified pump-probe mode matching and efficiency optimization.

The diagram of the ring cavity setup showing the essential optical components and the electronics used to lock the resonator for cw operation is shown in Fig. 4-9.

The PPLN crystal was situated in the center of the ring cavity arranged in a bow tie, or figure-8 configuration. A picture of the ring cavity showing the main optical components and the PZT used for locking the cavity at the peak of the transmission is shown in Fig. 4-10. The 4-cm-long PPLN crystal is located inside the white teflon oven which in turn sits on top of a multi-axis stage for x, y, z, tilt, and rotation. The light travels unidirectionally inside the resonator and from left to right through the PPLN, as indicated by the overlaying lines in Fig. 4-10. The 75 mm radius-of-curvature mirror $M1$ ($M2$) served as the input (output) for the probe (signal) and was coated for high reflection at λ_p and high transmission at λ_1 (λ_2). All optical components of the resonator were AR coated by VLOC Inc. Mirror $M3$ was a 2.15%-T flat coupler through which the pump laser entered the ring cavity. The leakage

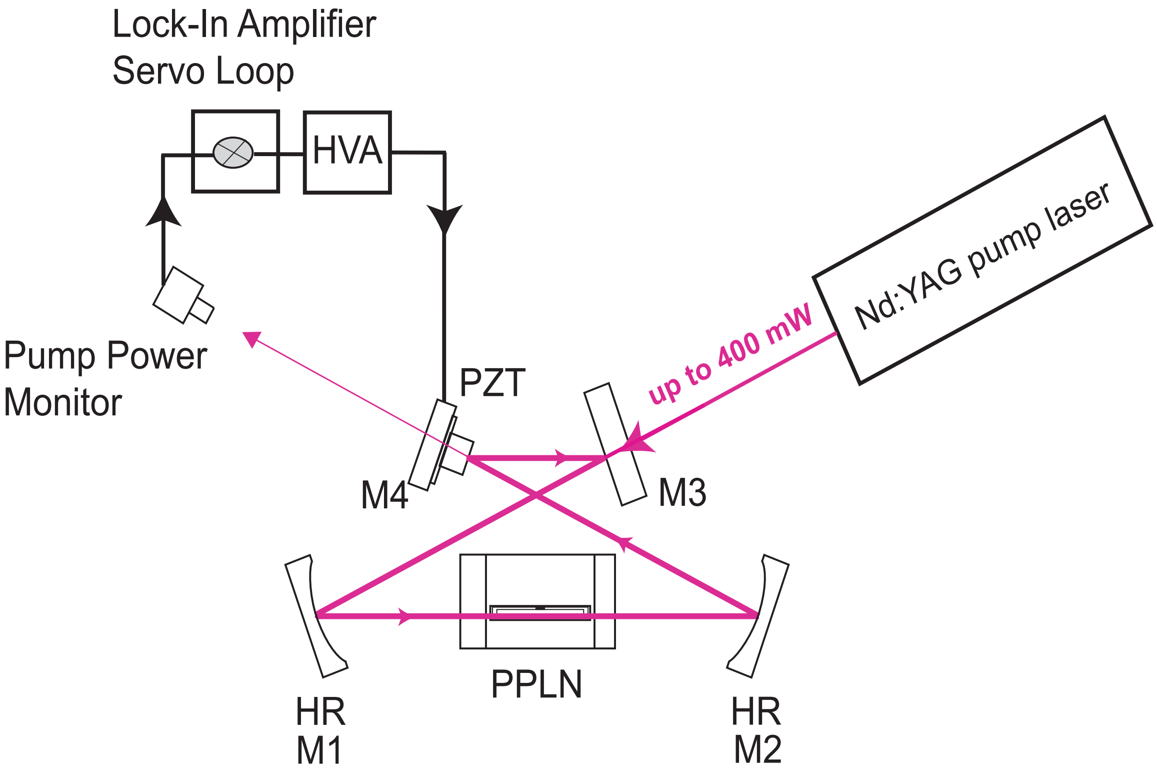

Figure 4-9: Diagram showing the main optical components of the ring cavity and the servo components for upconversion. HR: high-reflector at 1064 nm and high-transmission for 1550 and 633 nm; HVA: high-voltage amplifier; PZT: piezoelectic transducer.

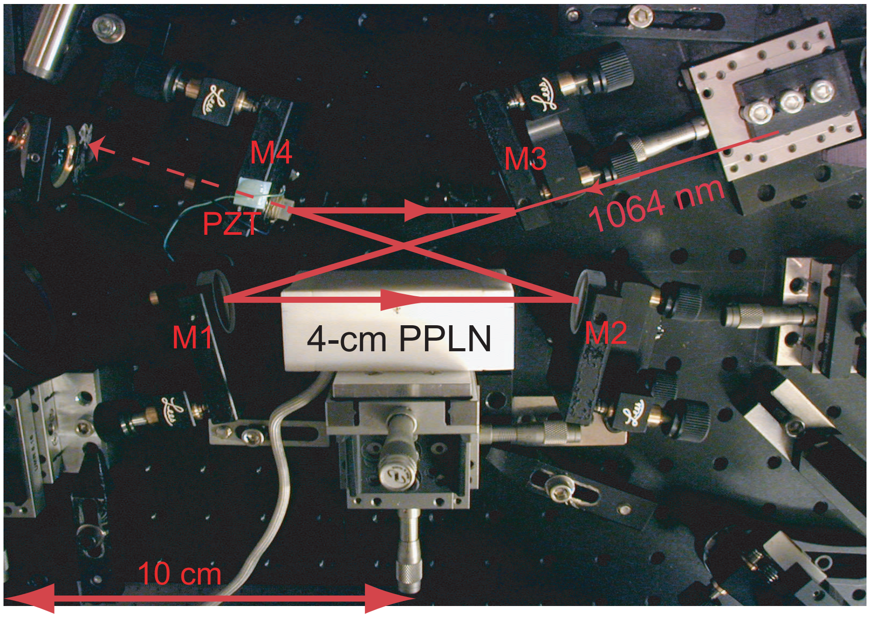

Figure 4-10: Picture of the ring cavity used for in the high-efficiency single-photon frequency upconversion experiments. The path traveled by the pump inside the resonator is indicated by the overlaying lines.

through the flat highly-reflecting mirror $M4$, with a transmission at the angle of incidence of ~0.02% at 1064 nm, was used to monitor the circulating pump power P_p using a high-speed amplified InGaAs photodiode (ThorLabs PDA400). The detector had a 1-mm diameter active area, a peak responsivity of 0.95 A/W at 1550 nm, 10-MHz bandwidth, and variable gain that could be adjusted by two orders of magnitude (up to 1.5×10^6 V/A). The measured responsivity of the InGaAs detector at 1064 nm was 0.74 A/W and the gain used during the measurements was 0.75×10^4. We mounted $M4$, which had a diameter of 7.75 mm, on a small piezoelectric transducer (PZT) and varied the length of the cavity by applying a triangular voltage waveform to the PZT. The waveform was generated by a Stanford Research Systems synthesized function generator (DS 345) and had an amplitude of 0 - 6 V at a frequency of 13 Hz. This signal was amplified by a factor of 100 using a high-voltage amplifier (Trek 601C) and then delivered to the PZT which swept the length of the cavity over a free spectral range. We servo-locked the cavity to the pump transmission peak using a dither-and-lock servo feedback loop. The block diagram and the schematic of the electronics used in the servo circuit are shown in Figs. 4-11 and 4-12.

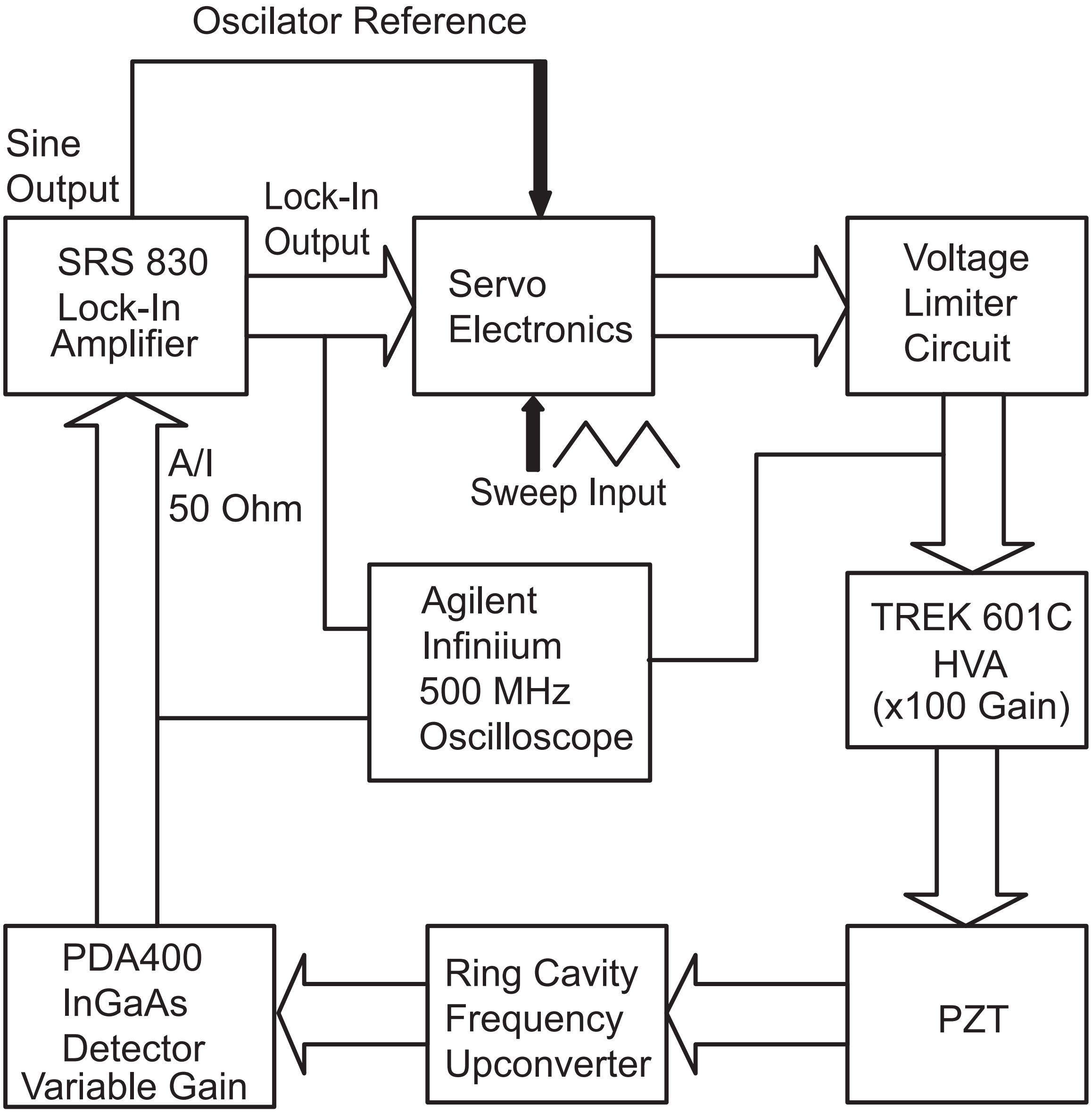

Figure 4-11: Block diagram of the servo system used to lock the ring cavity using a dither-and-lock technique.

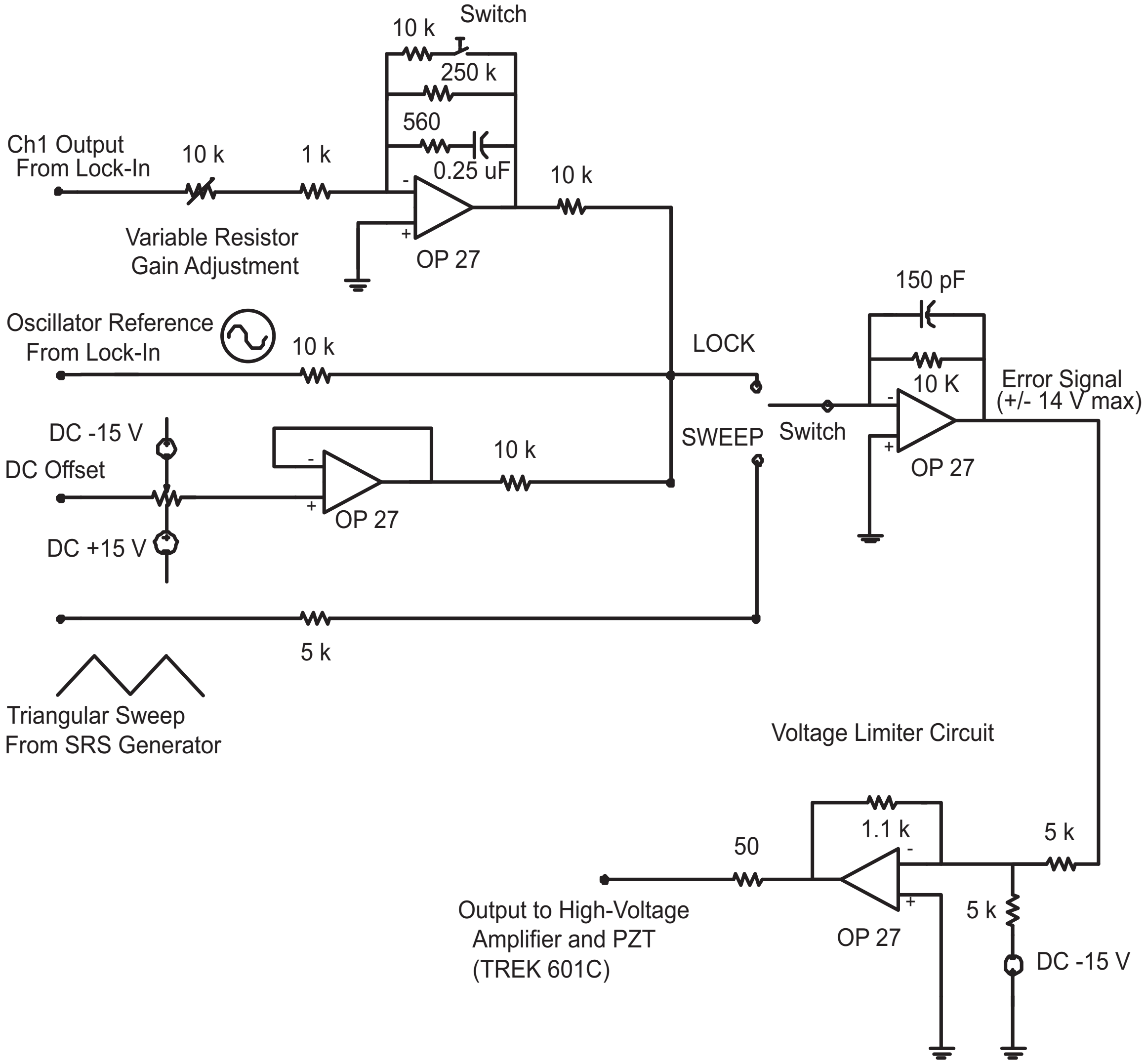

Figure 4-12: Schematic of the electronics inside the servo and voltage-limiter circuits used to sweep the length of the cavity and lock the ring resonator at the transmission peak.

The experimental setup for efficient upconversion is shown schematically in Fig. 4-13. The pump beam was first sent through a Faraday isolator (FI) to prevent back-reflections and a half-wave plate (HWP) and polarizing beam splitter (PBS), not shown in Fig. 4-13, that together functioned as a variable attenuator. The polarization of the pump beam was rotated by the second HWP to be horizontal or TM polarized. Horizontal (TM) polarization refers to polarization parallel to the surface of the optical bench while vertical polarization (TE) refers to polarization that is normal to the surface of the table. The crystal's z-axis was oriented horizontally or parallel to the plane of the optical table and all input and output beams were horizontally polarized, as required for phase matching. We mode-matched the pump beam into the cavity using a 300-mm lens AR-coated at 1064 nm situated on a micrometer stage just outside the resonator, before the input coupling mirror, $M3$. The input to

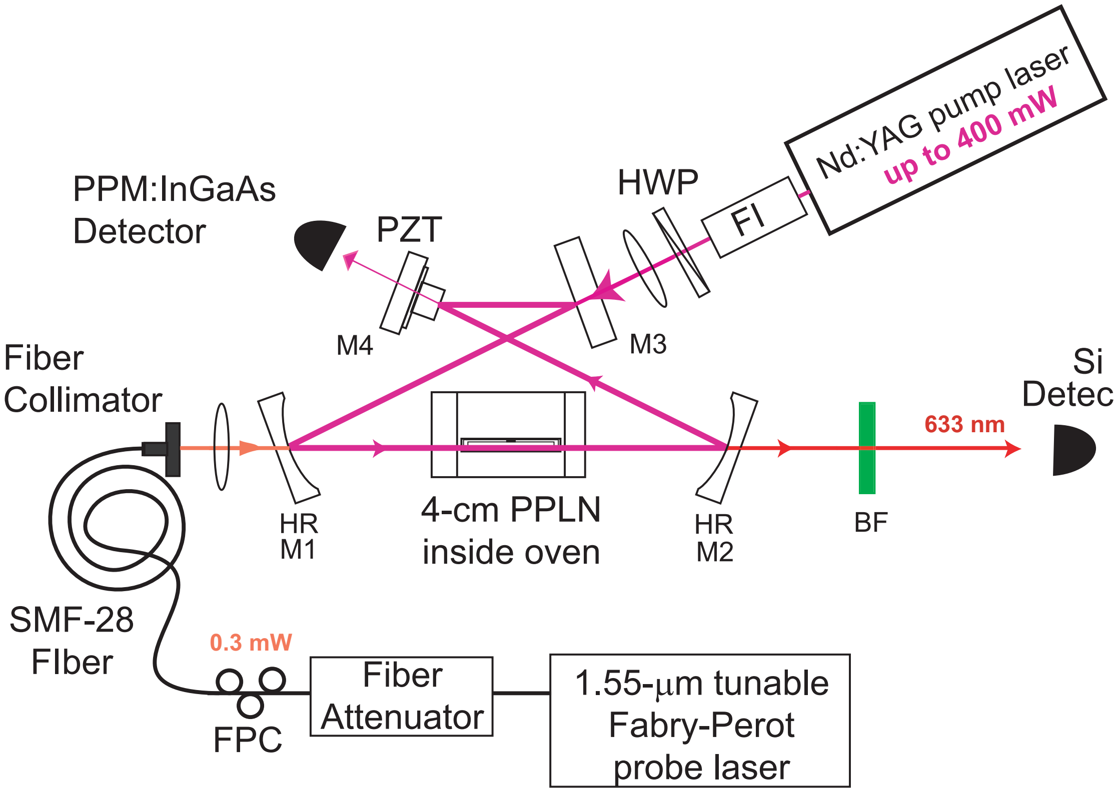

Figure 4-13: Experimental setup for near-unity upconversion of a weak-probe at 1.55 μm. FI: Faraday isolator; HWP: half-wave plate; FPC: fiber optic polarization controller; HR: high-reflector at 1064 nm; PPM: pump power monitor; PZT: piezoelectric transducer, BF: 10-nm bandpass filter centered at 633 nm.

the upconverter or probe light was supplied by a cw fiber-coupled Fabry-Perot laser (Agilent HP 81689A), tunable from 1524 nm to 1576 nm and capable of delivering up to 4 mW. A second fiber-coupled Fabry-Perot laser (Agilent HP 81649A), tunable from 1568 nm to 1620 nm, was utilized for upconversion experiments using the longer PPLN gratings on the crystal. The power of the input probe light was controlled with a 100-dB fibercoupled JDS Uniphase (HA9) optical attenuator. We calibrated the attenuator carefully using wavelength-flattened inline taps and an ultra-sensitive fiber-coupled InGaAs detector with 10 fW sensitivity. Precision and highly-repeatable attenuation could be achieved with this instrument down to the single photon regime. We adjusted the polarization of the 1.55 μm probe light with a fiber PBS that was followed by another free-space PBS.

The probe beam was collimated for propagation through free space using a fiberoptic collimator and we mode-matched the 1.55 μm light into the ring cavity with an $f = 150$ mm AR-coated lens situated on an x-y-z stage. The beam was adjusted to have a waist of ~67 μm at the center of the PPLN, and to overlap the pump-beam mode throughout the length of the cystal. We measured the actual beam waists with a beam scanner and monitored the horizontally polarized probe input to the cavity upconverter. We scanned the length of the cavity over a free spectral range by applying a triangular waveform to the PZT. We measured a cavity finesse (Finesse $= \frac{\text{FSR}}{\text{FWHM}}$) of ~210 and obtained a maximum circulating power $P_p \approx 23\,\text{W}$ using the 400-mW pump laser. Figure 4-14 shows scope traces of the pump and upconversion resonances in the cavity sweep mode at high pump power. Thermal hysteresis, the broadening of the transmission peaks at high pump power, on the leading edge of the cavity sweep waveform is clearly visible.

For continuous-wave operation we closed the feedback loop and locked the cavity to the pump transmission peak. The servo loop had a unity-gain frequency of ~20 kHz, and we were able to maintain a highly stable cavity lock for many minutes with an rms fluctuation of less than 1% in P_p. While pumping the PPLN at the highest pump levels and with the cavity locked, we observed significant thermal hysteresis due to the high circulating power. This was responsible for the heating of the crystal

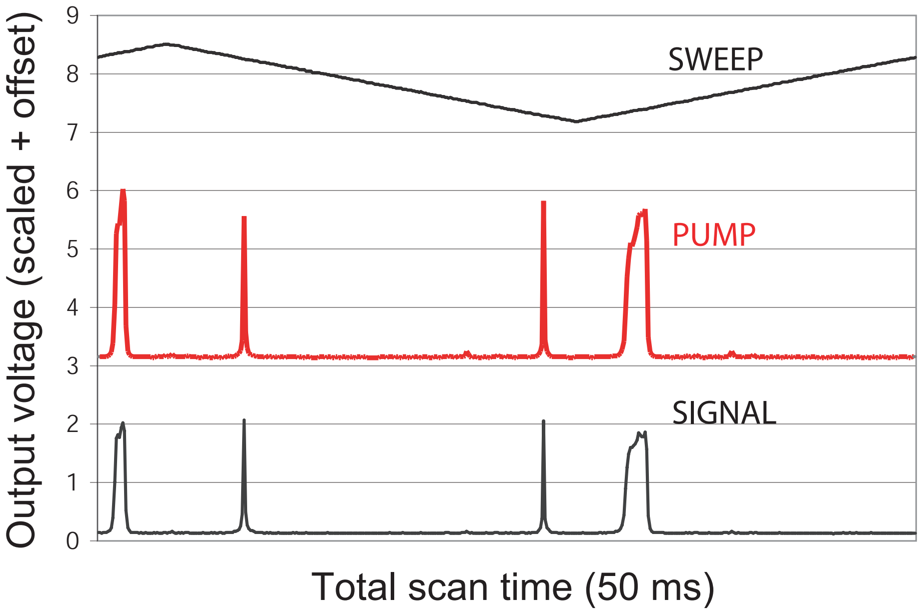

Figure 4-14: Upconverter operation in cavity scan mode at high pump power, showing the triangular sweep voltage applied to the PZT, the pump cavity resonances, and the upconversion signal. There is clear evidence of thermal hysteresis due to crystal heating.

and, in this regime, we noticed that the servo became slightly less stable. Figure 4-15 shows oscilloscope traces of the pump and upconverted light with the cavity locked. The fluctuations are small and the upconverter can operate in continuous mode with good long-term stability.

Initial measurements of the weak-probe upconversion efficiency were done with 284 μW of input power at $\lambda_1 = 1548.47$ nm. The cw output at 631 nm was filtered with a 1.06-μm HR mirror and a 10-nm interference filter centered at 633 nm. The imaging optics and spectral filters had an overall transmission of 68%. We aligned and calibrated our system with a HeNe laser and also in-situ using the upconverted signal. The upconverted light was detected using an amplified Si photodiode (ThorLabs PDA55). The detector had a large active area, 3.6 mm × 3.6 mm, a peak responsivity of 0.6 A/W at 960 nm, and 10-MHz bandwidth. The detector gain could be adjusted by two orders of magnitude (up to 1.5×10^6 V/A). We measured a responsivity of 0.317 A/W for the Si detector at 632.8 nm using a HeNe laser. The gain setting used in the measurements was 1.5×10^4 V/A. Figure 4-16 shows the intrinsic upconversion

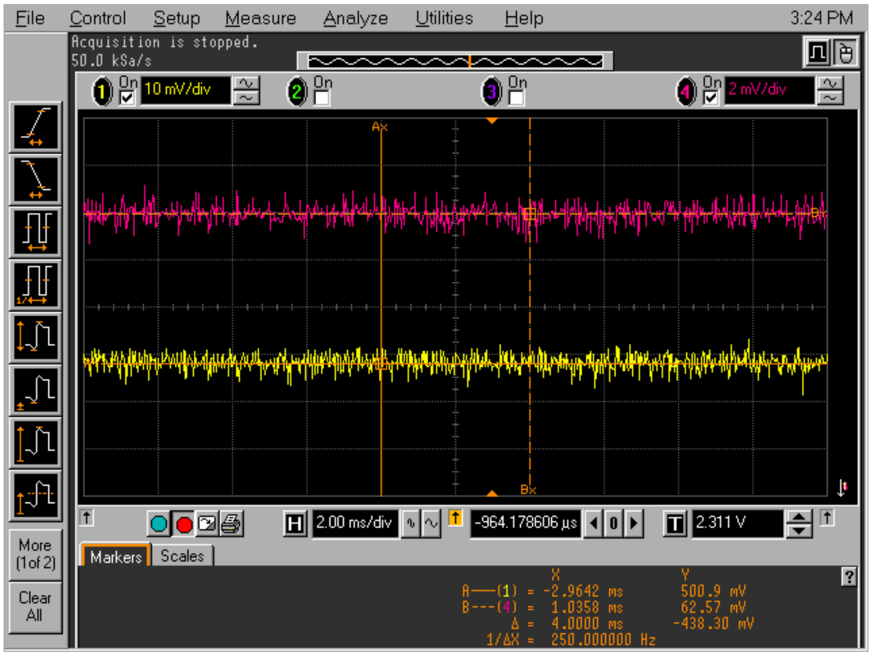

```
Acquisition is stopped.
50.0 kSa/s
```

```
1 On 10 mV/div
2 On
3 On
4 On 2 mV/div
H 2.00 ms/div
-964.178606 µs
T 2.311 V
```

```
                  X                  Y
A——(1) =  -2.9642 ms         500.9 mV
B---(4) =   1.0358 ms         62.57 mV
      Δ =   4.0000 ms       -438.30 mV
   1/ΔX =   250.000000 Hz
```

Figure 4-15: Upconverter operation in the continuous-wave mode, with the ring cavity locked to the pump transmission peak. The resonating pump power (lower trace) and upconversion signal (upper trace) are stable over several minutes with fluctuations of less than 0.5% and 1% respectively.

efficiency as a function of P_p while the solid line is a fit to the data using the functional form of Eq. 4.2 [34, 35].

From the data shown in Fig. 4-16 we notice that at low pump powers the efficiency is linearly proportional to P_p. This linear dependence agrees well with theory and with the data shown in Fig. 4-5 for the shorter PPLN and confirms that there was no pump saturation (for example due to high-power damage to the PPLN). A very similar linear dependence was found when the input probe power was gradually attenuated while keeping the pump power fixed, also in agreement with theoretical predictions. At high pump powers, the efficiency saturates as it approaches unity, also in excellent agreement with theoretical predictions. Our upconversion efficiency reached 93% at $P_p = 23\,\mathrm{W}$, with an estimated uncertainty of ±3% due to calibration accuracies. We were unable to reach unity efficiency due to insufficient pump power. From the fit in Fig. 4-16 we estimate $P_{\max} = 31\,\mathrm{W}$. This higher than estimated $P_{\max}$ is probably caused by a smaller d_{eff} (sub-optimal PPLN quality) and less-than-perfect

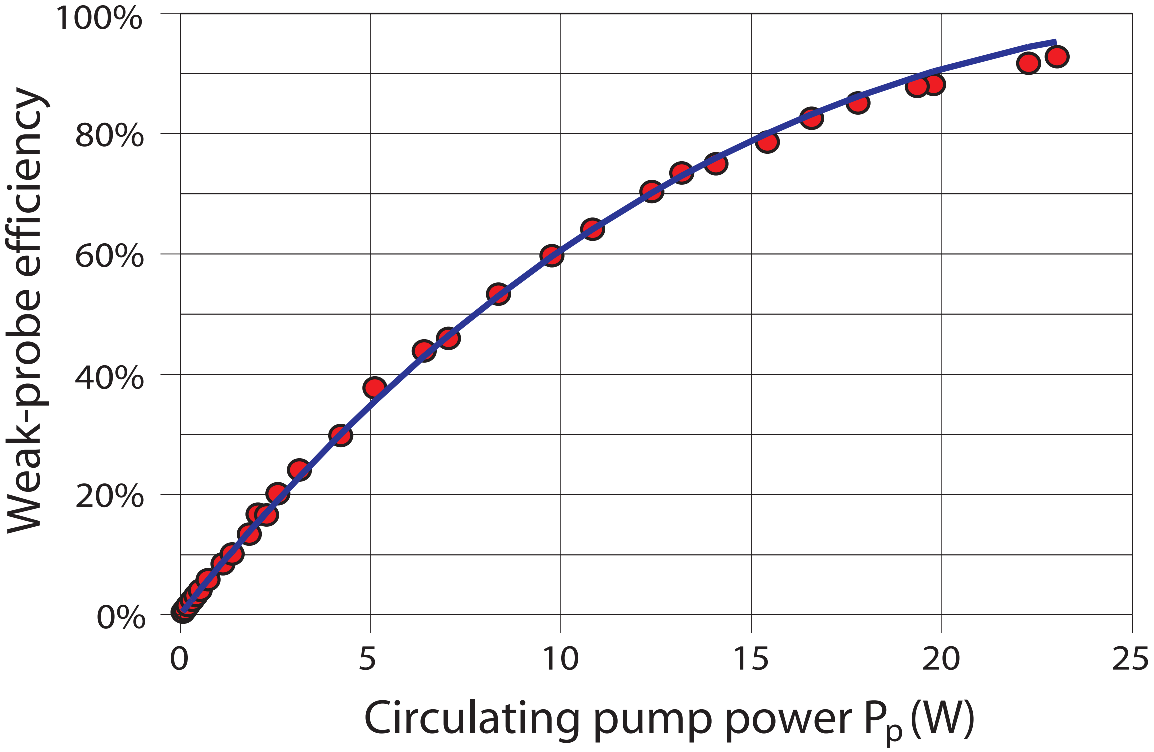

Figure 4-16: Weak-probe continuous-wave upconversion efficiency as a function of P_p. Filled circles: experimental data; solid line: functional fit of Eq. 4.2 with $P_{\max} = 31\,\text{W}$.

mode matching between the probe and the slightly astigmatic pump.

As an additional test of the performance of our frequency converter, we measured the depletion of the input probe light. The schematic for this measurement is shown in Fig. 4-17. At the upconverter's output we used a dichroic mirror with high reflection at 1.55 μm and high transmission at 633 nm and 1604 nm and measured the probe light with an InGaAs photodiode. A scope trace showing the pump power and the depleted probe light is shown in Fig. 4-18. As the pump power increases the upconversion efficiency goes up, which in turn results in a near complete depletion of the probe input. We obtained a maximum depletion of 89% at $P_p \approx 21\,\text{W}$, which is in very good agreement with the upconversion measurements shown in Fig. 4-16. The functional dependence of the probe depletion with increasing pump power is the complement of the upconversion efficiency function and was found to follow a $\cos^2 = 1 - \sin^2$ curve, as predicted by theory. [1]

---

[1] Along with the upconversion we observed, as part of the upconverter output the second harmonic of the 1064 nm pump, at 532 nm. It was important to investigate the magnitude of the

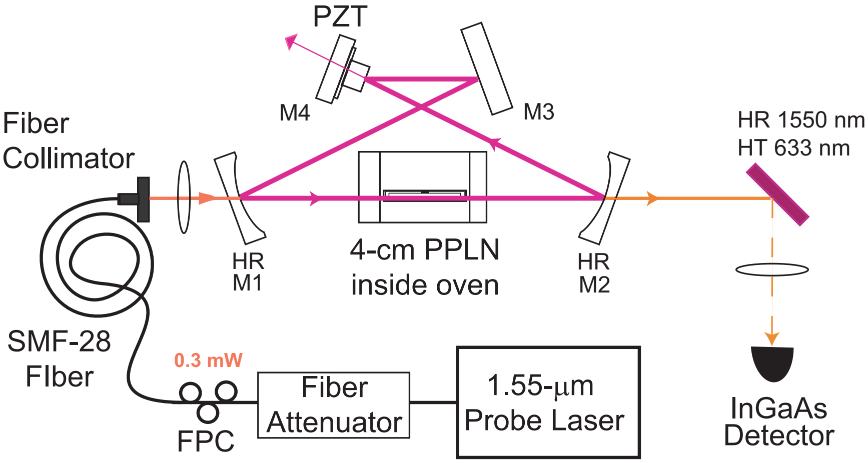

Figure 4-17: Experimental setup for measuring the probe depletion at high upconversion efficiency.

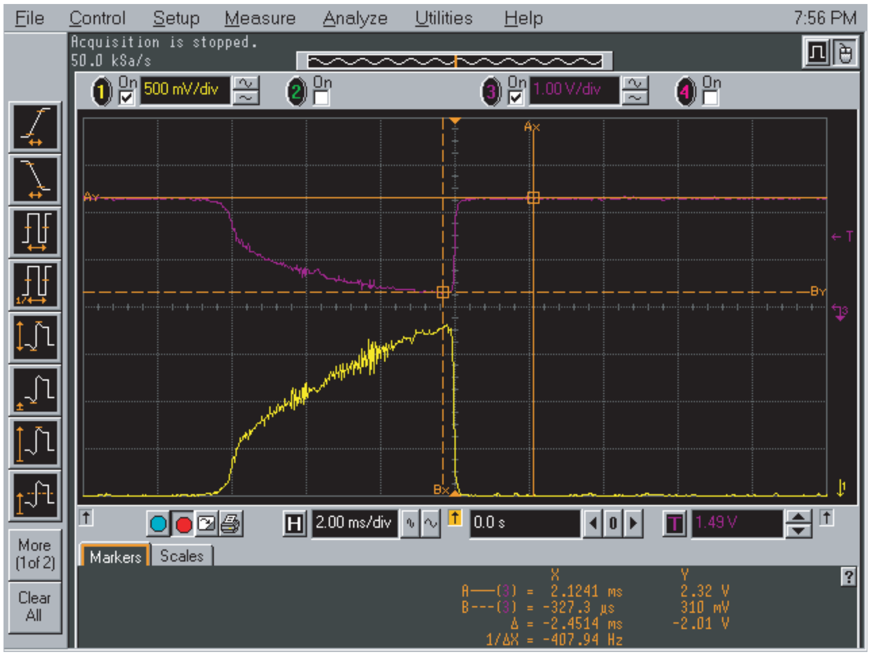

```
Acquisition is stopped.
50.0 kSa/s
```

```
                X           Y
A——(3) =  2.1241 ms      2.32 V
B---(3) = -327.3 µs      310 mV
      Δ = -2.4514 ms    -2.01 V
   1/ΔX = -407.94 Hz
```

Figure 4-18: Depletion of input probe at high pump power, showing the depletion of the probe (upper trace) as the pump (lower trace) is increased. The peak probe depletion in this measurement is ∼87% – achieved at a pump power of ∼20 W.

4.3 Upconversion of Individual Photons and Efficient Photon Counting at 1.55 μm

For upconversion at the single-photon level we attenuated the input probe power to 0.95 photon/μs using the JDS Uniphase optical attenuator. This input photon flux was low enough to eliminate multi-photon events in the measurement interval. The output imaging system for single-photon upconversion, shown schematically in Fig. 4-19, was more elaborate than that used for the weak probe measurements (Fig. 4-13) because it was essential to minimize any stray light or pump leakage reaching the Si SPCM. For additional output filtering of the upconverter, we used a dispersing prism and a 100-μm-diameter pinhole. The spectral and spatial filtering system was effective in preventing the weak second-harmonic light, the leakage pump, and the off-axis upconverted light from causing high background counts. The overall transmission of the imaging system was $\sim$58%, which included the 10-nm bandpass filter with T$\sim$71% centered at 633 nm. We focused the upconverted signal onto a commercial free-space Si Geiger-mode APD (PerkinElmer SPCM-AQR-14) using an AR-coated lens mounted on a two-dimensional translation stage. This SPCM had an active area diameter of $\sim$150 μm, a nominal quantum efficiency of 65%, and a dark count rate of $\sim$51 Hz.

The photon-counting data acquisition was computer-controlled using LabView. For continuous wave upconversion at the single photon level, we locked the cavity to the peak of the pump resonance and measured the counts as a function of P_p with and without the probe input. In Fig. 4-20, we show the cw output of the upconverter

---

SHG contribution, since a significant amount of light at 532 nm is known to produce photorefractive damage inside PPLN crystals. This could prove catastrophic in a cavity-enhanced frequency upconversion experiment in which circulating pump powers in excess of 20 W are expected. Moreover, if the 532 nm light is strong enough, green-induced infrared absorption may also become important. These issues are important in the weak probe as well as the single-photon upconversion regimes. Measurements of the SHG power indicated a low conversion efficiency for this non-phase matched interaction even at the highest pump powers. Therefore we did not expect the spurious SHG light to create significant problems in the near-unity upconversion experiments. Since the spectral separation between the upconverted light at $\sim$633 nm and the SHG is very wide ($>$ 100 nm), we expected that the SHG light can be suppressed with standard optical components, such as the dispersing prism and the 10-nm bandpass filter centered at 633 nm which we planned to use in the photon counting experiments.

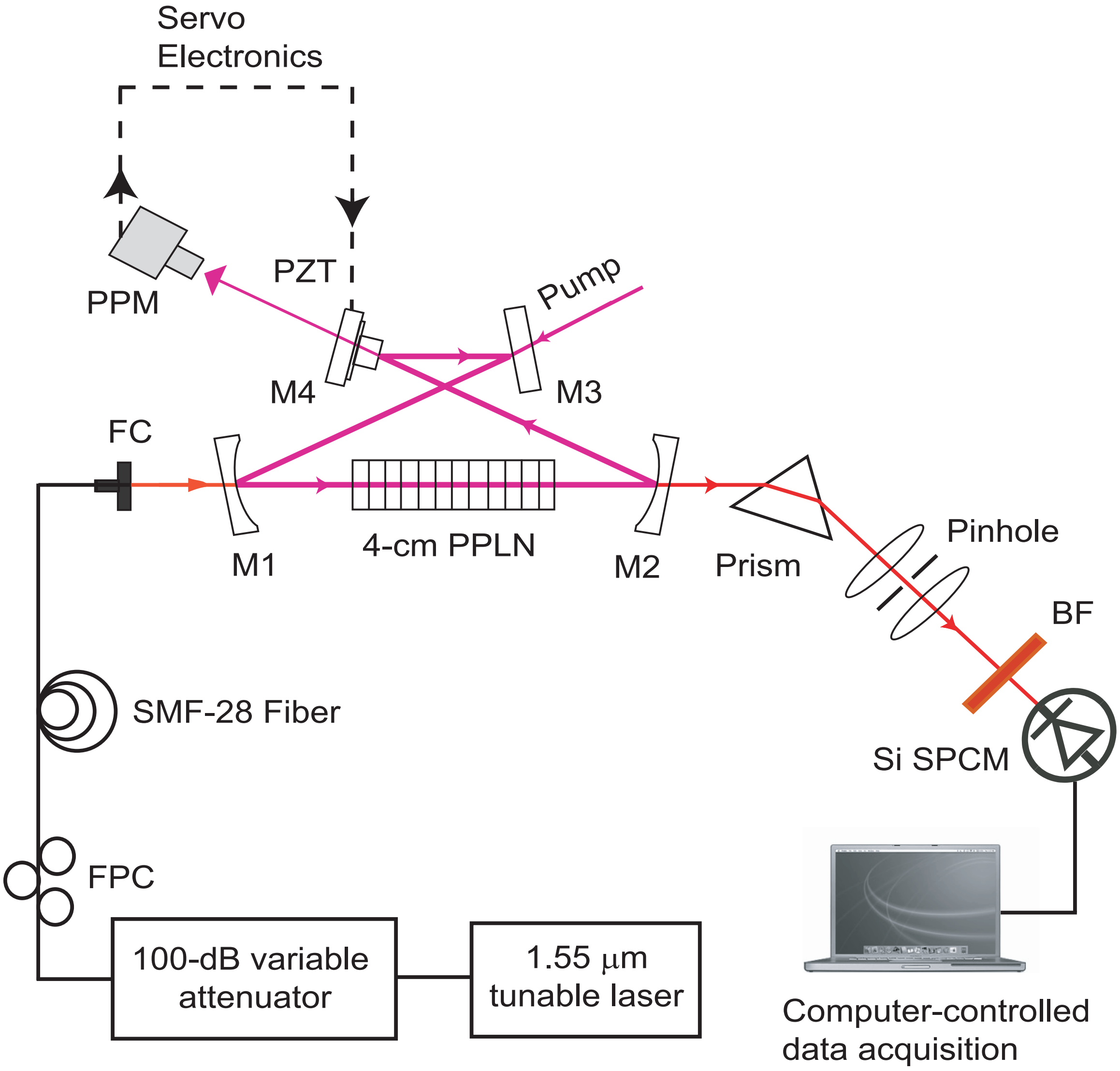

Figure 4-19: Experimental setup for single-photon detection at 1.55 μm via upconversion. FC: fiber optic collimator; BF: 10-nm interference filter at 633 nm and 1064-nm HR mirror; PPM: pump power monitor; FPC: fiber optic polarization controller; PZT: piezoelectric transducer.

after detection by the Si SPCM. For this measurement, the ring cavity was locked at a circulating pump power of ∼12 W and ∼90 x 10^3 dark counts (per second) were recorded by the photon counter at that pump power. At this P_p, the detected upconversion counts were a factor of 3 higher than the dark counts. Figure 4-21 shows the counts recorded by the Si SPCM as a function of circulating pump power in the absence of input probe light. The background contribution becomes significant at circulating pump powers in excess of 15 W. A maximum of 486 x 10^3 dark counts (per second) were detected by the Si SPCM at the peak circulating power of 21.6 W. The overall stability of the setup was good over several minutes as indicated by the scan time in Fig. 4-20. Figure 4-22 shows the intrinsic single-photon upconversion efficiency (filled circles) after subtracting the dark counts, indicating a maximum of 90% at $P_p = 21.6\,\mathrm{W}$. Along with the experimental data we also plot the functional fit of Eq. 4.2 as a solid line, showing again the excellent agreement between theory and experiment. The single-photon upconversion data is in very good agreement

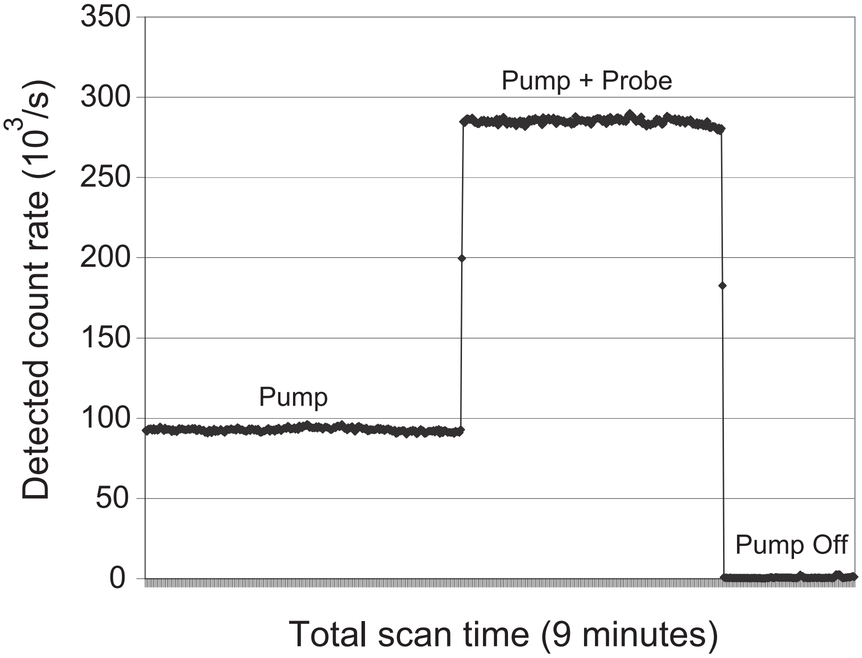

Figure 4-20: Photon-counting detection on the upconverter's output in continuous-wave mode at a circulating pump power of ∼12 W. Even in the absence of any input probe photons at 1.55 μm significant counts near 633-nm were recorded by the Si SPCM.

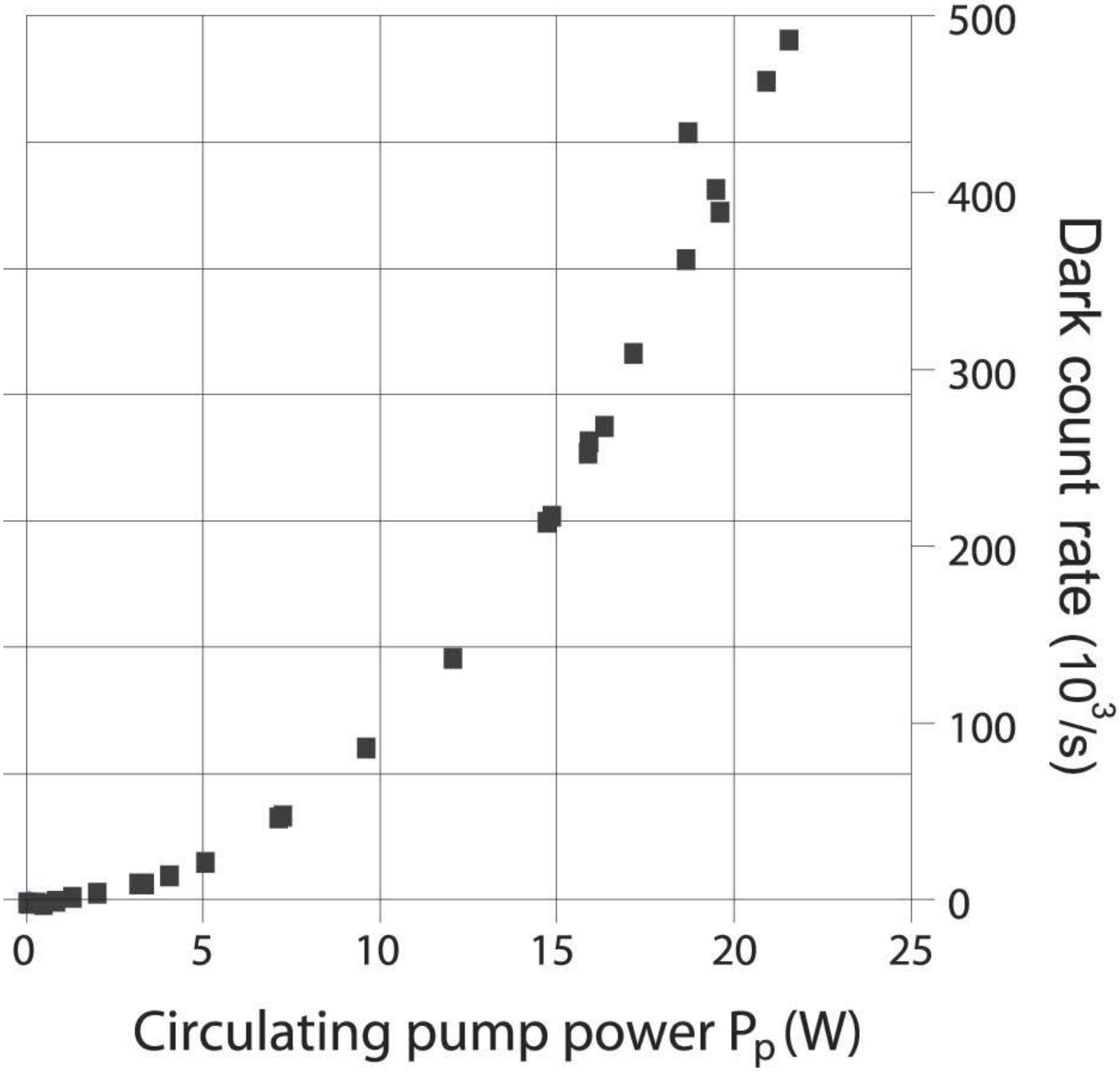

Figure 4-21: Dark counts detected by the Si SPCM as a function of P_p in continuous-wave mode in the absence of 1.55 μm input photons.

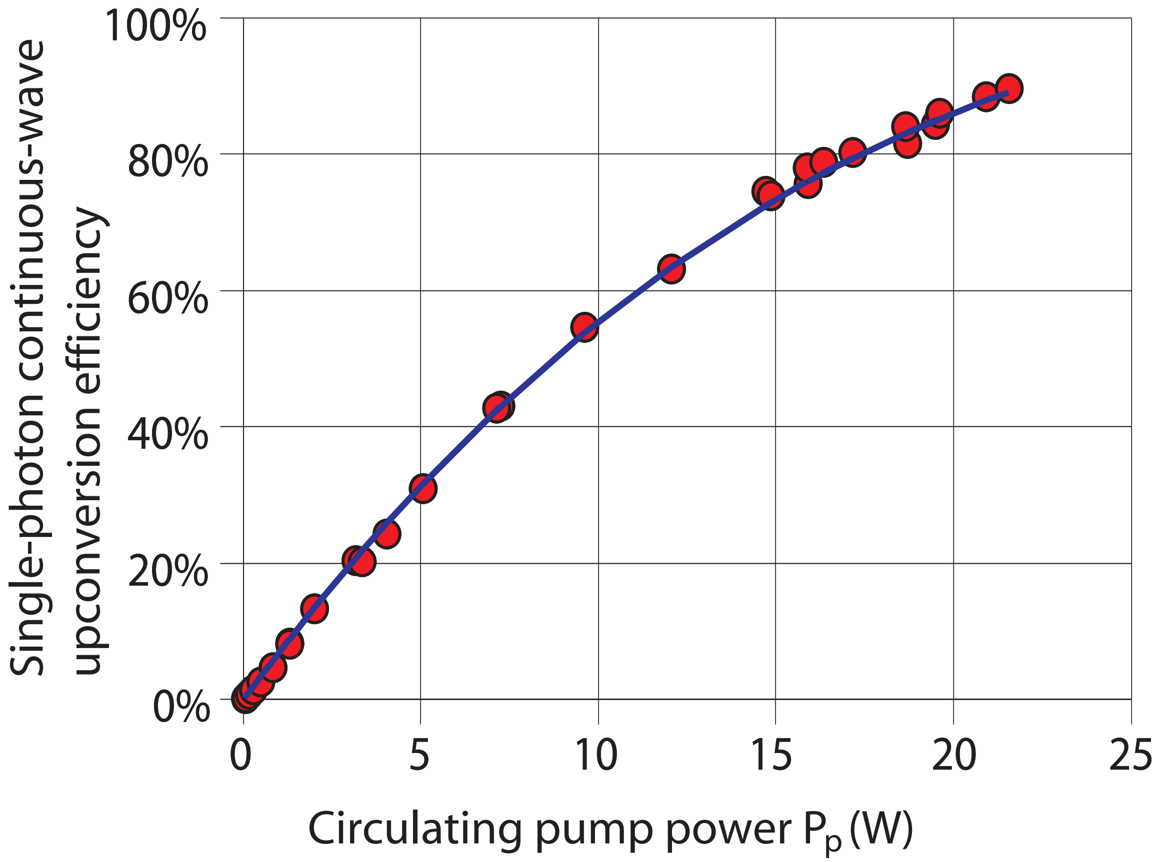

Figure 4-22: Single-photon continuous-wave upconversion efficiency as a function of P_p (filled circles). Solid line: functional fit of Eq. 4.2 with $P_{\max} = 35\,\mathrm{W}$.

with the data obtained in the weak-probe experiment. The major difference is that, in the single-photon measurements, at high P_p we observed the extraneous (dark) counts, noted earlier. These included detector dark counts and stray light of ~300/s. Figure 4-23 shows on the same graph, the upconversion efficiency on the left axis, the dark counts (open squares), and the net upconverted signal counts (filled circles) as a function of the circulating pump power inside the resonator. The net upconverted signal counts were obtained by subtracting the dark counts (without probe) from the total counts (with probe). These counts were not a factor in the weak probe upconversion regime because their effect is below the sensitivity of the measurement apparatus used in the weak-probe experiment.

An interesting effect we observed was the heating of the crystal at the highest P_p. This caused a small rise in the crystal temperature that in turn moved us off the phase-matching peak and slightly decreased the efficiency of the upconverter. This heating effect was evident only under cw operation and only at the highest pump powers. We compensated for the temperature shift by adjusting slightly either the probe wavelength (a maximum of < 0.2 nm) or the oven temperature set point to maintain peak upconversion efficiency. We note that the fit to the experimental data in the single-photon regime (Fig. 4-22) yields a unity-conversion pump power, $P_{\max} = 35\,\mathrm{W}$. This value is higher than that obtained in Fig. 4-16, ~31 W, probably as a result of slight pump-probe misalignment (the data was recorded at a later time).

The large number of extraneous counts that appear at high pump powers, as shown in Fig. 4-21, even in the absence of a probe input, can be a severe limitation in photon-counting applications. However, they are less of a problem for coincidence counting applications: a 1-ns coincidence window yields a maximum probability of an extraneous coincidence count of only 4.9×10^{-4} ($\leq 0.05\%$). We performed further experiments to study the nature of the extraneous counts recorded by the Si SPCM in the absence of 1.55-μm light. Using various spectral and spatial filtering techniques, we discovered that these extraneous counts are spectrally indistinguishable from the upconverted input counts and that there is little one can do to block them out of the

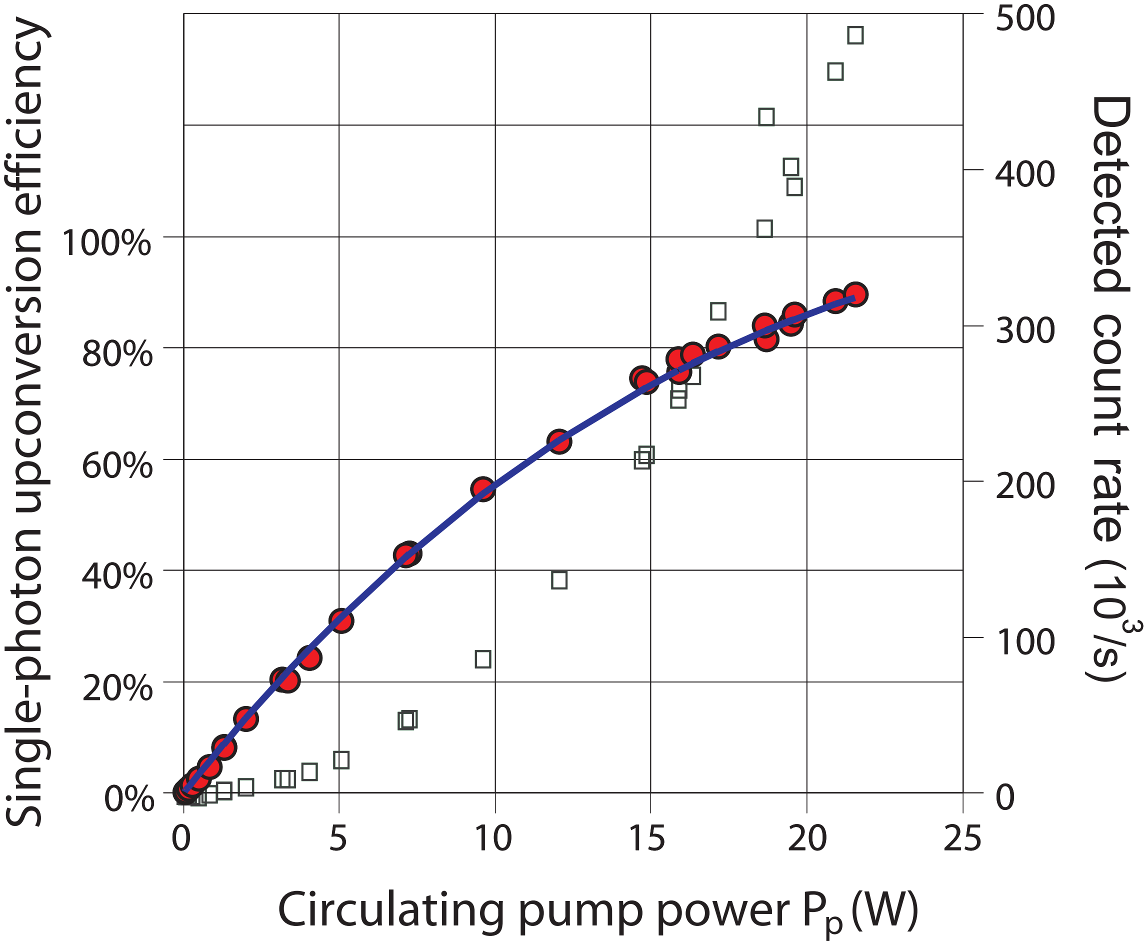

Figure 4-23: Right axis: upconverted signal counts (filled circles) and extraneous counts (open squares) as a function of resonant pump power (P_p). Left axis: upconversion efficiency at the single photon level and data fit.

output.

We note that the extraneous photons are likely due to a two-step cascaded process: pump-induced fluorescence or (non-phase-matched) parametric fluorescence at the probe wavelength λ_1, followed by upconversion from λ_1 to λ_2. The process is illustrated in Fig. 4-24. Our system, therefore, efficiently upconverted not only the input probe photons but also the small amount of fluorescence photons produced by the strong pump within the phase-matching bandwidth and with the same spatial mode as the input probe light. It is however possible to significantly reduce these unwanted counts. If we were to choose the pump wavelength to be longer than the probe wavelength, $\lambda_p > \lambda_1$, such that the energy of a pump photon is lower than the energy of the probe photon, the first step, generating the fluorescence photons, can be reduced. The concept is illustrated in Fig. 4-25. Yes, the high-flux pump will still spontaneously downconvert, but only over a spectral region far away from the upconversion bandwidth. We believe this is an important consideration when applying this technique for low-noise detection of infrared photons. Eliminating most of the extraneous counts will make this technique an even more attractive option for

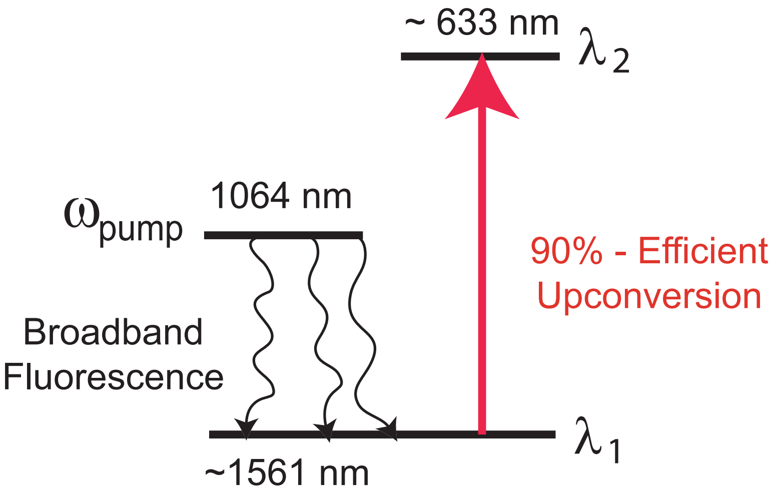

Figure 4-24: Cascaded interaction in PPLN at high circulating pump power in the absence of probe input. There are more than 10^{20} pump photons per second passing through the nonlinear crystal at high conversion efficiency. A small amount of pump-induced fluorescence or pump-driven parametric fluorescence around 1.55 μm is efficiently upconverted to the visible.

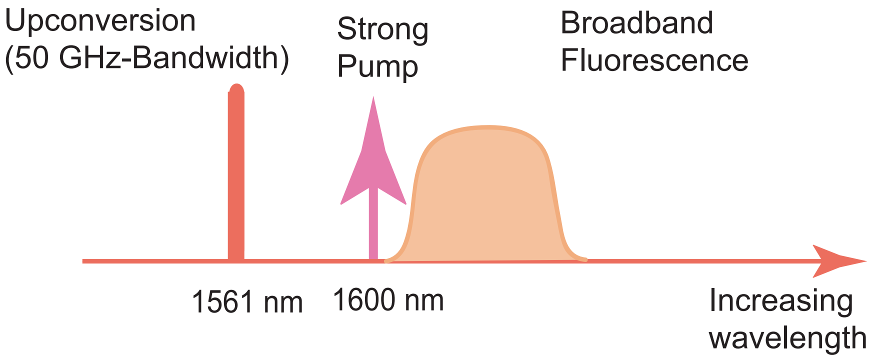

Figure 4-25: Background counts can be reduced by using a pump laser at a wavelength longer than the probe wavelength. In this way, the fluorescence generated will be mainly outside the upconversion bandwidth.

many quantum and classical applications. More recent studies by the Fejer group at Stanford University [56], have confirmed our thinking of the nature of these unwanted counts. Using a PPLN waveguide, a lower pump power, and the strategy suggested above, they have been able to significantly suppress the extraneous counts while maintaining a high system detection efficiency. The residual extraneous counts observed in their fiber-coupled waveguide setup are due to Raman scattering, which appears to suggest that complete elimination of the noise may not be straightforward.

Efficient single-photon upconversion from 1.55 μm to the visible or near infrared followed by Geiger-mode Si APD detection is an extremely attractive way to do 1.55 μm photon counting. The difference between the performance of photon-counting detectors at 1.55 μm and 795 nm is summarized in Fig. 4-26. The benefits of using Si Geiger-mode APDs rather than InGaAs photon counters are clear. By combining a 90%-efficient upconverter with a Si SPCM with 70% quantum efficiency, one may achieve cw counting of 1.55-μm photons at MHz rates with no afterpulsing. Figure 4-27 shows the performance of this type of detection scheme. An overall system detection efficiency in excess of ~60% can be achieved with this setup, which is much higher than that of current InGaAs detectors (see Fig. 2-8 for a direct comparison). If dark counts are the main concern, operation at 40% efficiency is possible with a dark-count probability of ~0.17% (per 20-ns measurement interval). In our upconversion scheme all wavelengths are widely tunable. Although the 633 nm output wavelength

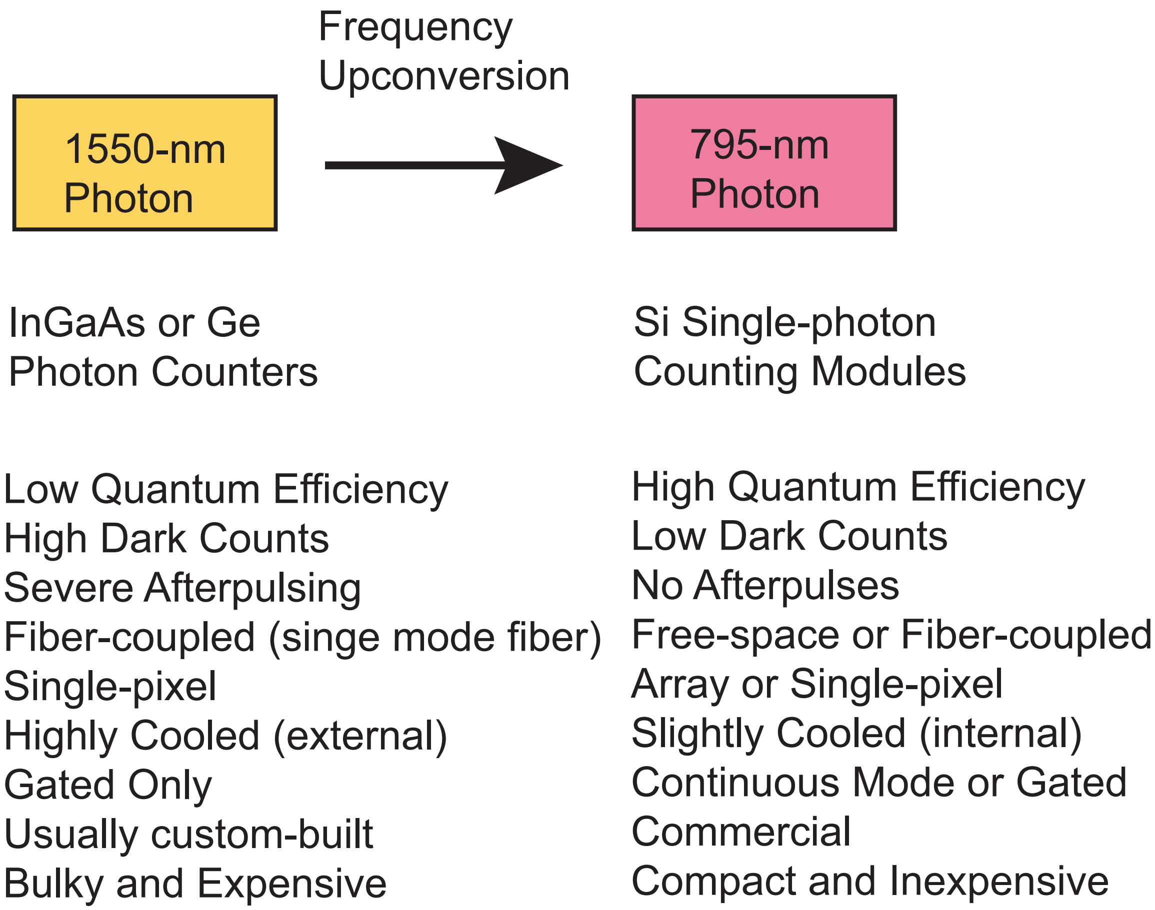

InGaAs or Ge Photon Counters	Si Single-photon Counting Modules
Low Quantum Efficiency	High Quantum Efficiency
High Dark Counts	Low Dark Counts
Severe Afterpulsing	No Afterpulses
Fiber-coupled (singe mode fiber)	Free-space or Fiber-coupled
Single-pixel	Array or Single-pixel
Highly Cooled (external)	Slightly Cooled (internal)
Gated Only	Continuous Mode or Gated
Usually custom-built	Commercial
Bulky and Expensive	Compact and Inexpensive

Figure 4-26: Comparison between the current performance of Si SPCMs and InGaAs photon-counting APDs.

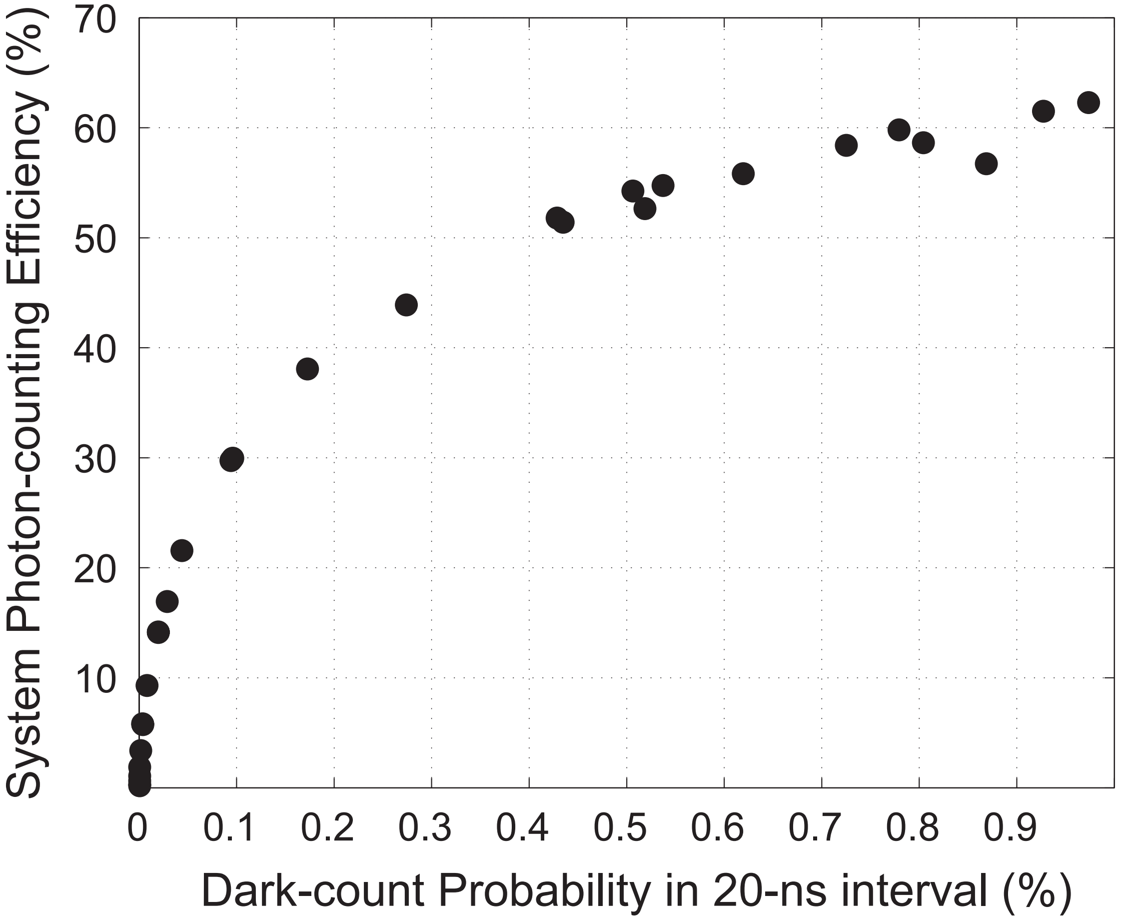

Figure 4-27: Performance of a detection system for 1.55 μm light using the 90%-efficient upconverter and a Si SPCM which performs photon-counting on the upconverter's output. The net system quantum efficiency is plotted as a function of dark count probability (per 20-ns gate) for easy comparison with Fig. 2-8.

of the upconverter does not match the absorption line of the Rb atom memory, as depicted in Fig. 1-2, that particular output wavelength could be achieved with a different PPLN grating and a pump laser at a longer wavelength.

In this chapter, we have reported efficient cw wavelength-tunable detection of 1.55-μm photons via sum-frequency mixing in bulk PPLN. The lack of sufficient pump power and sub-optimal mode matching limit our maximum upconversion efficiency to $\sim$90%. Higher efficiency may be achieved if one simply had access to a more powerful pump laser. If a more powerful pump is not available, modifications could be made to the upconversion setup to increase the finesse of the pump cavity or to further optimize the mode matching. Our scheme is also suitable for pulsed-input upconversion as long as the pulse bandwidth is narrower than the 0.3 nm phase-matching bandwidth of the PPLN crystal. Such pulses would permit the loading of trapped-atom quantum memories with typical bandwidths of 50 MHz [2]. Because the temporal upconversion bandwidth is inversely proportional to the length of the crystal, one could use a shorter PPLN to allow for the efficient conversion of pulses of longer duration than the transform limit of 50 MHz bandwidth. The upconverter also acts as a narrowband detection filter with a 0.3-nm passband, which is the natural bandwidth for a 4-cm long PPLN. The intrinsic spectral filtering capability of our upconversion scheme can be useful for free-space optical communication in which there is need for background suppression. Another feature of our photon counting scheme, of use for classical optical communications, is its intrinsic polarization selectivity. Because of the restrictions imposed by phase matching, only input light of a chosen, well-defined polarization, gets upconverted. This results in additional noise-count suppression capabilities for this detection scheme, which could prove useful for power-limited long distance optical communication. Unfortunately, this feature of our upconversion technique is undesirable for the teleportation-based quantum communication architecture. Sending polarization-entangled idler photons produced in the experiment described in Chapter 2 through the polarization-selective frequency upconverter would, due to its polarization dependence, collapse its polarization state to a definite value and hence preclude the proper loading of the Rb atom quantum memory.

4.4 Alternative Configurations for Upconversion

There are several techniques that could be used to implement an efficient single-photon upconverter. Possible schemes use nonlinear crystals in either bulk [34, 35, 57] or waveguide configurations [58]. The main advantage of using a PPLN waveguide rather than a bulk crystal is the possibility of more efficient intrinsic upconversion in a single pass geometry. Moreover, waveguide structures can be fiber-coupled and the entire experiment could be performed in fiber, taking advantage of inexpensive off-the-shelf telecom-grade components. In contrast, a bulk conversion scheme, such as the scheme demonstrated in the previous sections, employs a more complicated ring-cavity scheme for the pump that requires active servo-locking of the resonator. In a waveguide structure, the input probe and pump laser would both be fiber-coupled, mode-matching the three-wave-mixing interaction would be simplified, and the upconversion efficiency per unit length greatly enhanced. The required pump power for unity upconversion can be reduced by two orders of magnitude by using a PPLN waveguide. The delivery of the upconverted signal photons to remotely located atoms, as required for long distance quantum communication, would also be easier since the light would already be fiber coupled. All these benefits come however at the expense of waveguide and coupling losses that severely limit the maximum achievable overall efficiency. For example, for the best custom-designed waveguide structures, that are fabricated in-house and thus not commercially available, the overall transmission is on the order of ∼75% [58]. Commercially-available PPLN waveguides such as those from HC Photonics, suffer from even larger coupling losses, ∼25% at each interface between the fiber pigtails and the waveguide. Moreover, waveguide modal losses also reduce the net light throughput and therefore the maximum achievable upconversion efficiency.

For waveguide upconversion the natural choice is to use a fiber-coupled laser and a 1 W-class erbium-doped fiber amplifier (EDFA) pump system. EDFA systems are commercially available at wavelengths in the third telecommunication window. If we select the EDFA pump wavelength to be longer than the probe wavelength, $\lambda_p > \lambda_1$, such that the energy of a pump photon (at 1.57 μm for example) is lower than the energy of the probe photon (at 1.55 μm), the extraneous count problem described in Section 4.3 will be greatly reduced. However, an EDFA amplifies the pump but also adds amplified spontaneous emission noise. This noise is spectrally flat and could generate additional extraneous counts when this pump is used for single-photon upconversion. Moreover, the unavoidable sum-frequency generation from the pump (1.57 μm $\Rightarrow$ 785 nm) will, for this choice of wavelengths, be spectrally near the desired upconversion wavelength (1.57 μm + 1.55 μm $\Rightarrow$ 780 nm). This will impose much tighter spectral filtering requirements on the output of the upconverter (bulk or waveguide based) in order to suppress the unwanted light.

At the time this work was performed, an EDFA pump-laser system and low coupling-loss PPLN waveguides with independent temperature controls were not available in the laboratory. Therefore much more practical, in the near term, were the upconversion schemes which used bulk PPLN upconversion and the available Nd:YAG pump laser. However, the advantage of low-noise operation, the relative system simplicity achievable with a EDFA-pumped PPLN waveguide, and improving waveguide fabrication technologies, render waveguide upconversion a desirable choice for future experiments. Recent experiments on single-photon detection via upconversion in a PPLN waveguide [56] show that an overall system detection efficiency of ∼45% is possible. Upconversion with a pulsed pump and probe has also been recently demonstrated [57] in a bulk PPLN crystal. This scheme requires accurate timing synchronization of the incoming pulses and suffers from the same extraneous light problem observed in the other upconversion configurations.

4.5 Application of Polarization-Selective Upconversion for Long-Distance Teleportation

In the context of the MIT/NU proposal for quantum teleportation one might consider first an experiment which uses the polarization-entanglement source described in Chapter 2 together with the polarization-selective upconverter. The experimental configuration of the cascaded system consisting of the downconverter followed by the upconverter is shown in Fig. 4-28. In this setup, the 1.55-μm idler photons produced

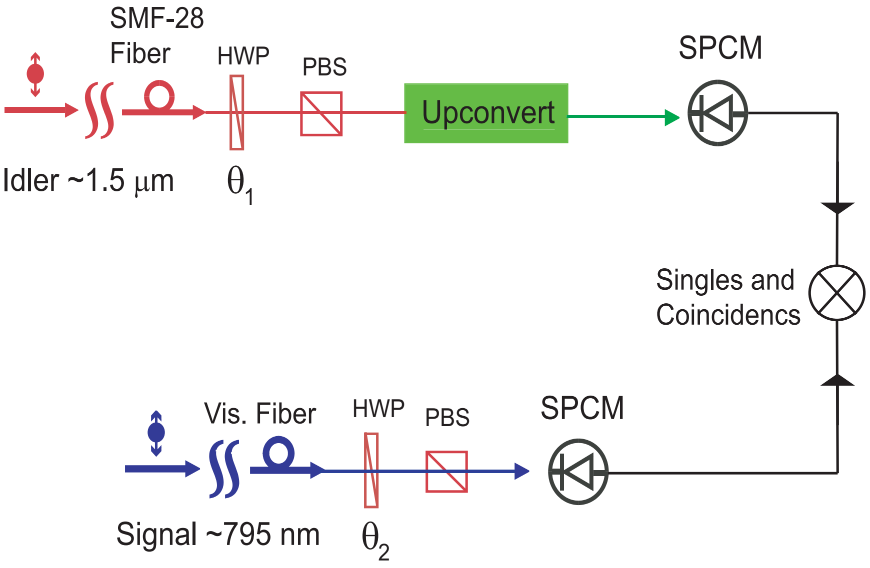

Figure 4-28: Schematic of frequency upconversion of a linearly-polarized portion of the idler state generated via downconversion. This setup allows us to measure the quantum interference and test the violation of Bell's inequality. Upconvert: polarization-selective single-photon upconverter; SPCM: Silicon single-photon counting module; HWP: half-wave plate; PBS: polarizing beam splitter.

in the PPLN SPDC would travel over an SMF-28 optical fiber and pass through a polarization-state analyzer composed of a HWP and a PBS. The fraction of the 1.55-μm photons that are upconverted to the Rb absorption line using a polarization-dependent upconverter are then detected with a free-space SPCM. The conjugate downconverted signal photons at 795 nm are delivered via a near infrared single-mode fiber to another SPCM after traveling first through the respective polarization-state analyzer. By fixing the angle (θ_1) of the idler HWP at 0°, 22.5°, and 45° (since these are HWP angles, the polarization rotation is twice θ_1), and sweeping the angle (θ_2) of the signal HWP one could measure a quantum interference signature similar to that shown in Fig. 2-5. This experiment is interesting and would provide insights into the process of entanglement transfer and upconversion. For example one could use this setup to demonstrate a violation of the CHSH form of the inequality derived by Bell. However, we point out that arbitrary-state upconversion is not possible with this configuration.

The MIT/NU protocol for long-distance quantum communication needs to load remotely located Rb atoms. Therefore, one must be able to direct the polarization-entangled idler photons into an upconverter that is capable of converting the frequency of individual photons of an arbitrary polarization. The generic setup is shown in Fig. 4-29. In contrast to the setup shown in Fig. 4-28, the Bell-state analysis here

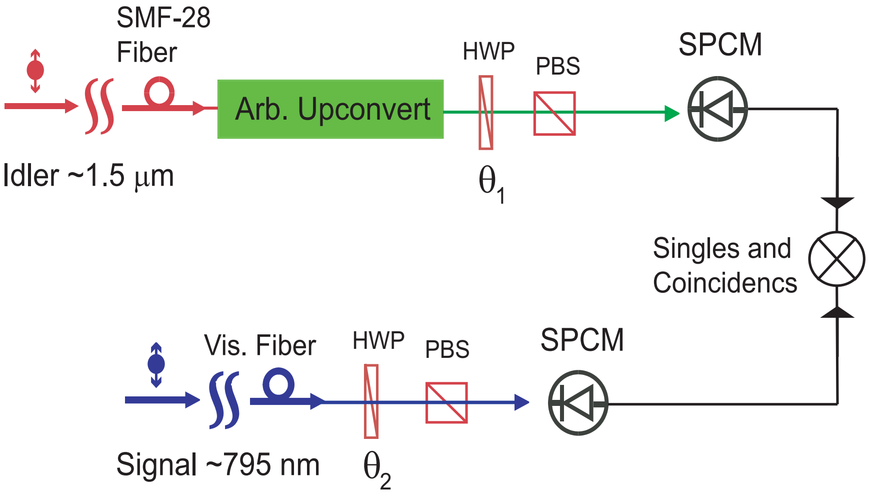

Figure 4-29: Schematic of full quantum-state upconversion of the downconverted idler state. Arb. Upconvert: polarization-independent single-photon frequency upconverter; SPCM: Silicon single-photon counting module; HWP: half-wave plate; PBS: polarizing beam splitter.

occurs after the input idler photons of arbitrary polarization have been upconverted. Although the two configurations look very similar, there is a significant difference between the schemes shown in Fig. 4-28 and Fig. 4-29. In the configuration illustrated in Fig. 4-29, the upconverted idler photon at ω_2 is still entangled with its paired signal photon at ω_s, thus permitting the option of sending the ω_2 photon to load an atomic memory. The setup shown in Fig. 4-28, on the other hand, allows one to measure the quantum interference and validate the violation of Bell's inequality but does not permit the transfer of photonic entanglement to atomic states – because the entanglement is destroyed by the HWP-PBS polarization analysis, which collapses the idler photon's state to a known linear polarization. In the following Chapter, we describe several experimental configurations that can perform polarization-preserving frequency upconversion.

Chapter 5

Schemes for Polarization Preserving Frequency Conversion

As we showed in Chapter 3, quantum state-preserving (unity efficiency) frequency translation of a linearly polarized single-photon quantum field centered at frequency ω_1 to a higher center frequency at ω_2 is theoretically possible. In Chapter 4, we demonstrated 90% upconversion efficiency of a linearly-polarized single photon input field. The feasibility of the quantum frequency upconversion scheme has been shown theoretically [23] and verified experimentally with pulsed twin beams of light [54]. Using a type-II birefringently phase matched KTP crystal, Kumar and his co-workers measured nonclassical intensity correlations of ~1.5 dB below the shot-noise limit between the upconverted beam and the remaining beam.

The efficient frequency upconversion scheme that we have implemented is only capable of upconverting photons of a well-defined, in our case horizontal, polarization. This constraint is imposed by the phase-matching geometry for type-I QPM in PPLN. In fact our geometry is not special. Most nonlinear conversion experiments use crystals that intrinsically phase match light of a definite polarization. A more specialized setup that is capable of upconverting an arbitrarily-polarized input state is required to convert entangled photons from one frequency to another with polarization-state preservation. The basic idea of arbitrary-state wavelength conversion is illustrated in Fig. 5-1. In the context of the long-distance quantum communication scheme

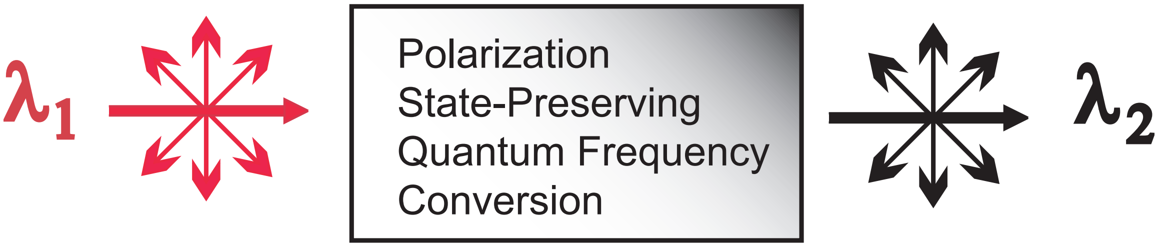

Figure 5-1: Frequency translation of arbitrarily-polarized photons from λ_1 to λ_2 with polarization-state preservation.

this polarization-insensitive frequency converter is a key quantum-interface component that would enable the loading of remote quantum memories. First, however, an efficient single-photon polarization insensitive frequency upconverter has to be demonstrated. Unfortunately such a device does not currently exist. Moreover, one has to show that the photonic entanglement of the flying qubits survives the frequency translation process. The schematic of the experiment which needs to be performed in order to determine if this is indeed the case is shown in Fig. 5-2.

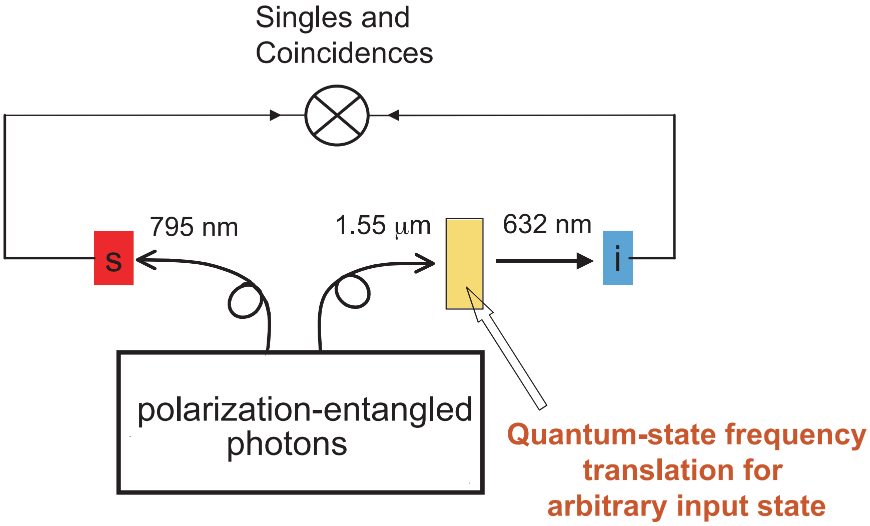

Figure 5-2: Conceptual sketch of quantum-state upconversion of polarization-entangled photons. Geiger-mode detectors for the signal (s) and upconverted idler (i) photons are used to measure the quantum correlations.

5.1 Upconversion in a Dual-PPLN Mach-Zehnder Interferometer

The most natural option for upconverting an arbitrary polarization state uses two of the polarization-selective PPLN upconverters described in Chapter 4 arranged in a parallel configuration. The schematic for this experiment is shown in Fig. 5-3. The input to the upconverter is the ~1.55-μm idler arm of the entangled quantum state characterized by the wavefunction $|\psi\rangle_{si}$ of Eq. 1.1. The idler photons are delivered over a long SMF-28 fiber-optic cable from the SPDC source to the upconverter. In this configuration, the beam is first separated with a PBS into horizontal or TM components (denoted by $\updownarrow$) and vertical or TE components (denoted by $\bullet$). The TM-polarized photons take the upper path and, because they have the right polarization, are frequency translated by the upper ring-cavity upconverter. They travel a total distance L1 before they reach the second PBS. The TE-polarized photons, sent through the lower path, L2, are first rotated with a HWP into TM polarization and are then upconverted by the lower upconverter. The Nd:YAG laser at 1064 nm is split in half and coherently pumps the two cw single-photon ring-cavity upconverters. If this arrangement were built using one 400-mW pump laser then the maximum up-

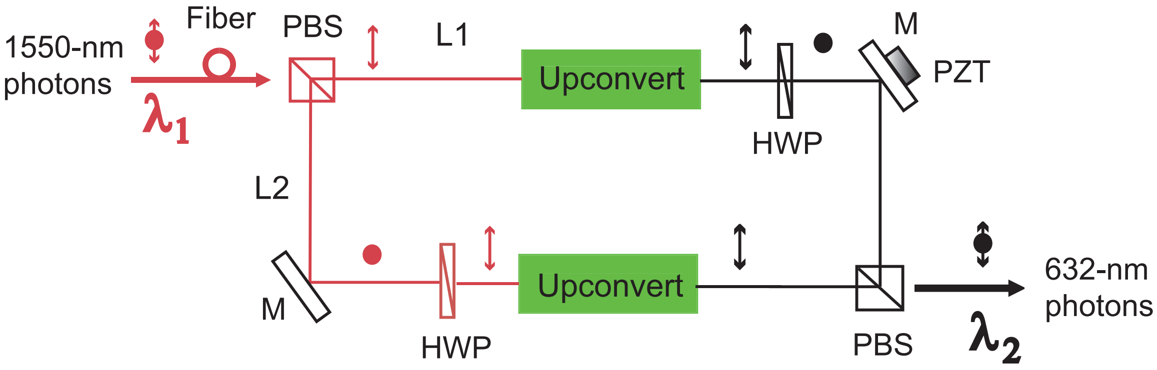

Figure 5-3: Implementation of polarization-preserving frequency upconversion in a dual-PPLN configuration. L1 and L2 are the distances traveled by the photons through the upper and lower paths, respectively, from the input PBS to the combining PBS. M denotes reflecting mirrors, one of which is mounted on a piezoelectric transducer (PZT) to control the relative delay between the two paths and phase-lock the Mach-Zehnder interferometer.

conversion efficiency would be limited to ~60% for each path because the circulating power in each ring cavity would be half of what we achieved in our Chapter 4 experiment (see Fig. 4-22). Higher efficiency could be achieved if one had access to a more powerful pump laser. Upon exiting the respective upconverters, the upper and lower signal outputs at 632 nm are both TM polarized. The visible photons generated in the upper path are transformed to TE polarization with a HWP and reflected by the second PBS. The photons that travel the lower-path are left unchanged and, after traveling a total distance L2, are transmitted by the second PBS. The two beams are interferometrically combined and directed to a single-photon counter. After the polarization-insensitive upconversion is implemented, the correlations between the upconverted and conjugate signal photons from the downconverter could be measured with a pair of polarization-state analyzers and SPCMs. Coincident-photon counting on the output of the upconverter and the signal arm of the SPDC output would then permit verification that the initial entanglement had been translated from one frequency to the other. A test of Bell's inequalities could be implemented using the setup shown in Fig. 5-4. The boxed area represents the quantum-state upconverter, which includes the two coherently-pumped polarization-selective cw single-photon upconverters.

Interferometric combination of the two arms and phase stabilization are required to maintain the polarization state of input light through the upconversion process. The net delay between the two arms of the interferometer must be compensated such that the photons completely overlap in time within their ~60 GHz bandwidth upon emerging from their respective upconverters. Therefore the two path-lengths of the Mach-Zehnder interferometer must be equal ($L1 = L2$) to within a tenth of the free-space length of the photons (~300 μm). Moreover active phase stabilization of the ϕ time-phase drift is also required. A length stabilization of the interferometer within $<< \lambda_2/2 \approx 315$ nm is necessary. This could be achieved by mounting one of the reflecting mirrors on a PZT, and servo-locking the interferometer between the two beam splitters using a side-lock technique. Without interferometric control of the output state the quantum visibility will be severely reduced. Spatial-mode

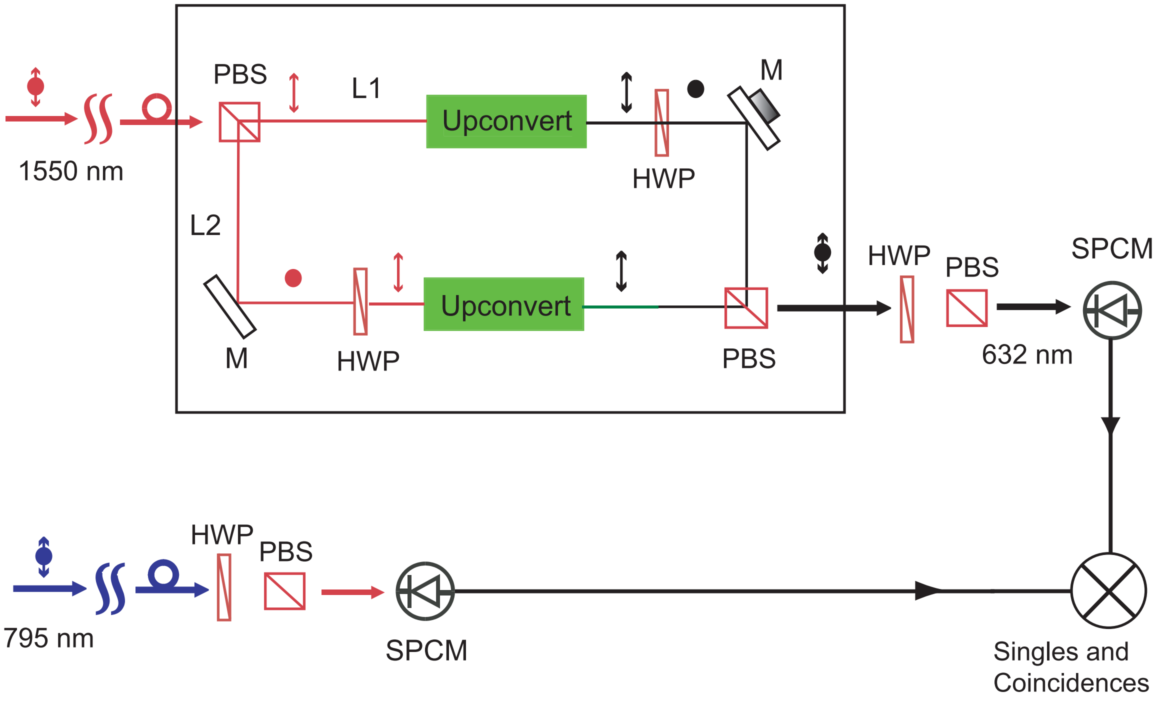

Figure 5-4: Verification of entanglement transfer via coincident-detection measurements of the CHSH form of Bell's inequalities.

overlap between the emerging upconverted beams is also required in order to ensure entanglement preservation. This could be realized by using identical optics and mode-matching parameters in both beam paths.

Dual-PPLN upconversion scheme for arbitrarily-polarized light could, alternatively, be implemented in two crystals arranged in series and rotated at a 90-degree angle with respect to each other. In this way, the first PPLN would upconvert horizontally-polarized light while the vertically-polarized component of the input light would be converted inside the second PPLN crystal. This cascaded configuration is similar to that reported by Kwiat [11] for efficient entanglement generation in a pair of birefringently mode matched BBO crystals. Since we have already demonstrated the feasibility of the polarization-selective ring cavity upconversion method, the dual-PPLN configuration scheme appears straightforward to implement. For simplicity, we assumed in the analysis that the free-space and crystal losses are the same for the upper and lower paths. If this is not true, one branch of the upconverter will be more efficient than the other, and the resulting asymmetry will degrade the quantum-interference visibility. The challenge this scheme poses is servo-locking of the Mach-Zehnder interferometer while also maintaining stable, phase-locked operation of the two independent ring-cavity upconverters. Because the input and upconverted light are at the single photon level, these wavelengths cannot be used to lock the Mach-Zehnder interferometer. One option for a locking signal would be to use the residual pump light that exits each of the upconverter resonators. Another option for phase stabilization may be to use the undesirable byproduct of our upconversion scheme, i.e., the green second-harmonic light, or inject a monitor wavelength for locking.

5.2 Polarization-Preserving Upconversion via Time-Division-Multiplexing

The second potential configuration we investigate in this Chapter employs time-division-multiplexing (TDM) to achieve the goal of polarization-preserving frequency translation. In contrast to the parallel upconverter scheme described above, it relies on a single polarization-selective ring-cavity upconverter. The setup, configured for a test of the CHSH inequality, is shown in Fig. 5-5. The boxed area represents the single-polarization quantum state upconverter. The scheme employs two electro-optic modulators (EOMs), one operating at 1.55 μm and the other at $\sim$632 nm. These EOMs rotate the polarization of optical radiation via the Pockel's effect. In a CHSH experiment, the SPCM for the 795 nm photon triggers the EOMs which rotate the polarization of the photons. The SPDC idler photons are delivered from the source to the upconverter by an SMF-28 fiber-optic patch cord. In this scheme the arbitrarily-polarized input idler state at 1.55 μm is first separated into TM and TE components with a fiber-optic PBS. The TE-polarized photons are delayed by $\Delta T \approx$ several ns with respect to the TM photons using a loop of optical fiber of length L1. The two polarizations recombine at the second PBS as shown in Fig. 5-5 resulting in a train of TM and TE-polarized photons temporally separated by ΔT. The 1.55-μm photons exit the fiber and are directed through the first bulk EOM. This free-space

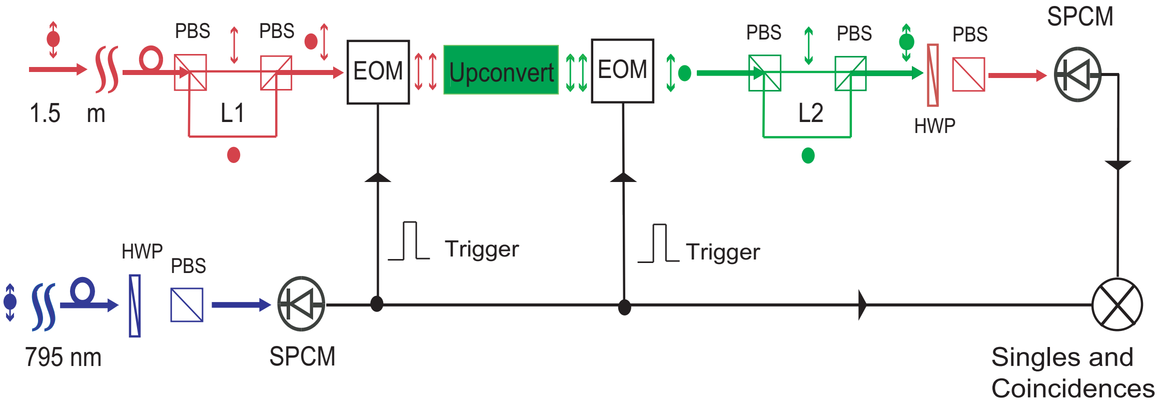

Figure 5-5: Arbitrary-polarization upconversion scheme which uses TDM and a single ring-cavity cw single-photon upconverter. For a CHSH Bell's inequality measurement the SPCM triggers the EOMs which rotate the polarization of the photons. For the MIT/NU implementation TDM without external triggering will be required [2].

modulator rotates the polarization of the TE-polarized photons while letting the TM-polarized photons pass through with their polarization unchanged. All TE-polarized photons are therefore transformed to TM in preparation for their subsequent upconversion in the cw single-photon upconverter. After emerging from the PPLN crystal, the upconverted signal at 632 nm consists of a sequence of TM-polarized photons, still temporally separated by $\sim \Delta T$. These visible photons then pass through a second free-space EOM which performs the conjugate polarization transformation, after which the photons are coupled into a single mode fiber for visible wavelengths. Upon traveling through the second fiber-optic delay line of length L2, the TM and TE photons are overlapped in space-time with another fiber PBS. At the output of the quantum state upconverter a frequency-translated version of the input entangled idler state is in this way generated. The entanglement between the upconverted and conjugate signal photons is measured with a pair of polarization-state analyzers and SPCMs and a test of the CHSH form of Bell's inequalities is performed.

In order for this scheme to be feasible, the polarization rotation must work with low insertion loss and high polarization contrast at speeds on the order of 100-200 MHz for typical fiberoptic delays of 5-10 ns. EOMs with those performance specifications are commercially available. For example the NewFocus model 4102 free-space broadband amplitude modulator works for wavelengths between 500 and 900 nm, has a radiofrequency bandwidth of 200 MHz, and requires a switching voltage of 195 V. For the 1.55 μm photons, the NewFocus model 4104 EOM has similar performance: 200 MHz RF bandwidth and 300 V for switching. Both of these units would be capable of rotating the polarization of individual photons separated by a minimum time delay of $\Delta T \approx 10$ ns. Another option is to use two pulse-selection systems from Conoptics. For the visible wavelength, the 307A driver mated to the 350-50 modulator provides switching pulses with a $\sim$5 ns rise time at maximum repetition rates of 50 kHz for a $\sim$10 cm long modulator with a clear aperture of 3.1 mm. For 1.55 μm operation the 307A driver and 360-40 modulator provide a performance similar to that of the visible wavelength unit. The typical insertion loss for these Conoptics modulators is 6%. The overall losses for the TDM scheme would consist of the fiber PBS loss ($\sim$0.9 dB), EOM insertion loss ($\sim$6%), and losses associated with the fiber-coupling of the upconverted photons into the visible fiber delay loop ($\sim$30%). For the CHSH test, both the infrared and visible EOMs would be gated-on by the SPCM for the 795-nm downconverted signal. Therefore care must be taken that the overall electronic triggering system is properly synchronized. Because the bandwidth of the fiber-coupled downconverted photons is $\sim$60 GHz, the path difference $(L1 - L2)$ must be less than a tenth of the free-space length of the photons ($\sim$300 μm). Moreover interferometric path-length stabilization will be required in order to maintain a constant phase ϕ and also to measure the quantum interference. Since the delays are provided by fiber-optic patch cords, the process of servo-locking this setup will be more complicated than would be the case for the parallel upconverter implementation we considered earlier. Locking could perhaps be achieved by using a fiber-optic stretcher but it is not clear what signal could be used to provide the necessary feedback to stabilize the interferometers. Without interferometric control of the output state the quantum-interference visibility will be severely reduced. Alternatively, the TDM upconversion scheme could be implemented with a pair of fiber-optic switches, instead of the EOMs, in a configuration very similar to that shown in Fig. 5-5. These switches would combine the TM and TE components of the input and upconverted photons after they have been delayed relative to each other using length-matched fiber-optic delay loops.

As explained above, delay compensation and interferometric stabilization would still be required. High-speed switches with < 3 dB insertion loss, 1-ns switching times, and crosstalk isolation better than 30 dB are available for 1.55 μm operation from EOspace and JDS Uniphase. For example, the 2 × 2 interferometric switch from JDS Uniphase (Model 10020457) requires less than 7 V of drive voltage, has high extinction, and achieves switching times below 1 ns. However, all these devices work for wavelengths in the telecommunication window. For operation at the upconverted wavelength of 632 nm custom-made switches would be needed.

The preceding description of the TDM-based upconversion, although satisfactory for the CHSH verification, cannot be used as shown in Fig. 5-5 for the MIT/NU teleportation protocol because EOM triggering in that architecture cannot be derived from detection of the 795-nm photons. TDM-based upconversion can, nevertheless, be very useful for the MIT/NU teleportation architecture. According to that proposed protocol [2], fiber-optic cables in excess of 50 km would be used to transfer the entangled photons from the source to the storage nodes. A polarization-entangled state could be badly degraded by this propagation process, due to inherent polarization-dependent fiber inhomogeneities (eg., refractive index, polarization-mode dispersion). To circumvent these polarization degradations, the MIT/NU protocol proposes to postpone the polarization combining of the 1.55 μm outputs from its dual downconverter source. The scheme instead proposes transmitting them as time-separated temporal modes that are in the same linear polarization and accompanied by a strong pilot pulse of the same polarization that is combined to a third time slot. Pilot-pulse polarization analysis is then used to derive the information needed to restore the 1.55 μm downconverter output temporal modes that arrive at the remote location to the desired linear polarization. These polarization-restored modes may be upconverted in our single-polarization ring-cavity system, after which the EOM-based polarization combining, shown in Fig. 5-5, can be used, with the triggering derived from pilot-pulse timing measurements.

5.3 Bi-directional Upconversion of Arbitrarily Polarized Light in Bulk PPLN

Another interesting scheme for arbitrary-state upconversion uses bi-directional pumping of a single PPLN crystal located at the center of a standing-wave cavity with two counter-propagating directions for the input as well as the upconverted beams. The ~1.55 μm idler arm of the entangled quantum state characterized by the wavefunction $|\psi\rangle_{si}$ of Eq. 1.1 is transmitted over an SMF-28 fiber-optic cable from the SPDC source to the upconverter. Rather than separating the input beam into vertical and horizontal components, as in the schemes described above, the entire entangled state is sent through a single polarization-selective upconverter. One potential realization of this scheme is shown in Fig. 5-6. The standing-wave cavity is only resonant at the pump frequency and is single-pass for the probe and upconverted output. The arbitrarily-polarized idler photons of the entangled quantum state exit the optical

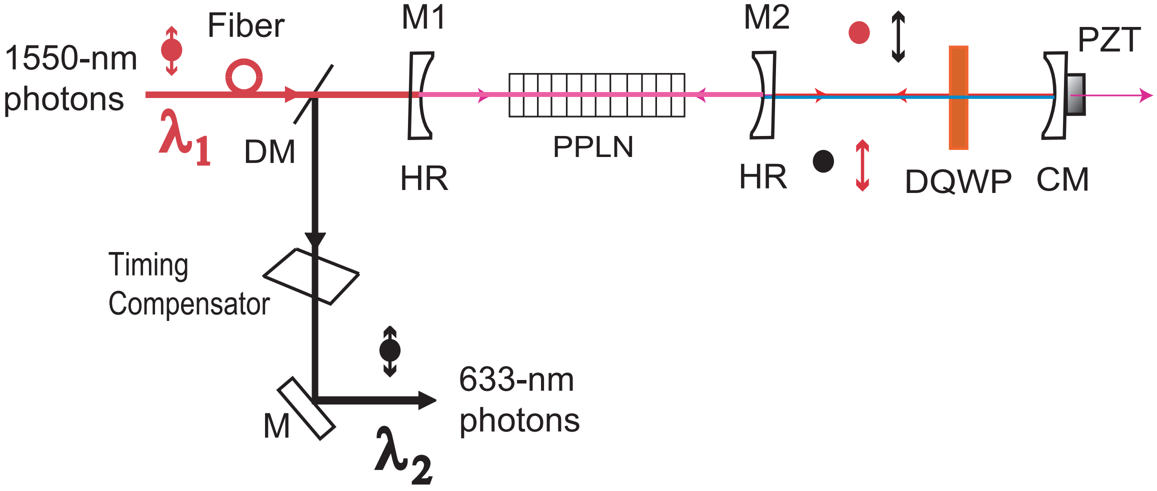

Figure 5-6: Arbitrary-state upconversion in a single bi-directionally pumped bulk PPLN crystal. Two counter-propagating pump beams inside a standing-wave cavity produce upconverted light in the forward and backward directions. DM: dichroic mirror (HR for 632 nm, HT for 1.55 μm); DQWP: dual-wavelength quarter-wave plate for 632 and 1550 nm; PZT: piezoelectric transducer; CM: curved mirror (HR for 632 nm and 1.55 μm, HT for 1064 nm).

fiber and are mode-matched into the polarization-dependent single-photon upconverter. In its first pass through the PPLN, from left to right, the horizontal (TM) component of the input idler state would be upconverted. The remaining portion of the input photons would be mostly vertically (TE) polarized. The idler photons that were not upconverted then exit the upconverter along with the visible output photons which are TM-polarized. The entire output beam is then reflected back into the upconverter after a 90° polarization rotation, achieved for example using a dual-pass through a dual-wavelength QWP. The visible photons that were generated in their first pass through the nonlinear crystal will now be vertically polarized and will traverse the crystal unaffected by the non-phase-matched nonlinear interaction. The portion of the input idler photons that were not converted in their first pass will now be horizontally polarized and will be upconverted to 632 nm during their second pass through the PPLN. The stream of upconverted photons with horizontal and vertical polarization, now traveling in the same direction, are separated from the input with a dichroic beam splitter. The photons now pass through a birefringent crystal which compensates for the time delay that has accumulated between the two orthogonal polarizations and are detected with a photon-counting detector.

This scheme has the appealing qualities of being the most elegant and least expensive to implement. Although a standing-wave cavity would be required for the implementation of this scheme, the same optical elements that were used in the ring-cavity upconverter can be used. Yet several issues would have to be addressed. We mention that a QWP that works well at the vastly different idler and output wavelengths, 1.55 μm and 632 nm, is required. A birefringent timing-compensator which will temporally overlap the upconverted photons of TM and TE polarization is also needed. Since the time-delay accumulated by the infrared and visible photons could be significant, the length of this timing compensator, an unpoled piece of $LiNbO_3$ for example, could be inconvenient. Servo-locking this standing-wave cavity may prove to be more challenging. To achieve a higher damage threshold an MgO-doped PPLN crystal would have to be used to handle the higher peak power that this type of cavity will require if it is to achieve high-efficiency upconversion. These MgO:PPLN crystals are now commercially available and have a damage threshold that is a factor of 170 higher (1,700 kW/cm^2 at 488 nm) than that of undoped congruently grown PPLN devices. Phase-locking the path-length between M2 to CM is also required. The Fabry-Perot interferometer could be locked using the residual pump light at 1064 nm or the second-harmonic light at 532 nm, with both of these signals originating from inside the cavity and traveling the same path length as the probe and upconverted light.

5.4 Upconversion in a PPLN-based Sagnac Interferometer

The fourth and last scheme we have considered for polarization-preserving upconversion is shown schematically in Fig. 5-7. Just like the bi-directional upconversion scheme described above, it uses a single PPLN crystal located inside a standing-wave cavity. The difference is that in this configuration, the input and upconverted light travel clockwise (CW) and counter clockwise (CCW) inside a Sagnac loop and additional locking is not required.

The probe beam at 1.55 μm is first separated with a PBS into horizontal (TM), denoted by (↕) and vertical (TE) components, denoted by (•). The horizontally polarized photons take the upper path through the loop. Since they have the proper polarization, these photons are frequency translated as they travel clockwise around the Sagnac interferometer. After upconversion, the 632-nm light traveling CW passes through a dual-wavelength HWP which imparts a 90° polarization rotation to the photons (• ⇄↕). The 633-nm light is then reflected by the dual-wavelength PBS and separated from the input light by a dichroic mirror. The fraction of the input photons that have vertical polarization are meanwhile sent through the lower path, and travel CCW along the Sagnac loop. They are first polarization-rotated by the same dual-wavelength HWP into horizontal polarization and are then upconverted. The 632-nm output light is transmitted by the dual-wavelength PBS and is separated

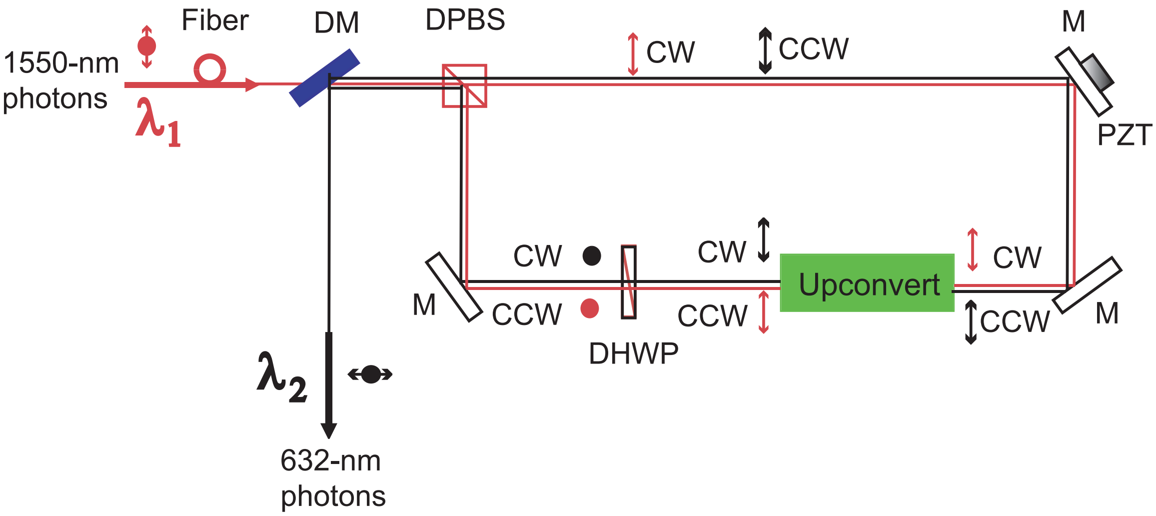

Figure 5-7: Frequency upconversion of an arbitrary polarization state can be implemented using a single PPLN crystal located inside a Sagnac interferometer. DHWP: dual-wavelength half-wave plate for 1550 and 632 nm; DM: dichroic mirror (HR for 632 nm, HT for 1.55 μm); DPBS: dual-wavelength polarizing beam splitter for 1550 and 632 nm; PZT: piezoelectric transducer.

from the input light by the dichroic mirror. The visible photons at the output now consist of a frequency translated version of the input light. The photons are directed towards a Si photon counter for coincidence-counting. We note that for the actual realization of this scheme a dual-wavelength HWP and PBS are needed.

In the next Chapter, we demonstrate the experimental implementation of a polarization-insensitive frequency conversion scheme that uses bi-directional pumping of a single bulk PPLN crystal inside a standing-wave cavity. We show polarization-state preservation of arbitrarily polarized input light in the low-flux as well as single-photon regimes.

Chapter 6

Polarization-Preserving Frequency Upconversion

In Chapter 5, we investigated several configurations that would allow the realization of a polarization-preserving upconverter. In this Chapter, we describe the experimental implementation of one of these schemes. We demonstrate polarization-preserving upconversion from 1.56 μm to 633 nm. In this novel scheme the input horizontal (vertical) polarization is upconverted in the forward (backward) direction and a dichroic Michelson interferometer is used to adjust the relative phase to maintain the polarization angle. In this way an input photon at 1.56 μm with an arbitrary polarization is upconverted to 633 nm photon with the same polarization at the output. This polarization-preserving upconversion scheme represents an important step towards implementing polarization-preserving quantum-state frequency conversion for use in long-distance quantum communication schemes such as the one shown in Fig. 1-2.

6.1 Polarization-Preserving Upconversion

For type-I quasi-phase matching in PPLN utilizing the d_{33} nonlinear coefficient, the coupled-mode analysis derived in Chapter 3 only applies to linear polarizations along the crystal's z axis. No upconversion occurs for the linear polarization that is orthogonal to this axis. Quantum optical communication requires quantum-state upconversion, for which the first step is to achieve polarization-independent upconversion. The configuration we have chosen for this purpose is shown in Fig. 6-1. It employs type-I phase matching in a single, polarization-selective, PPLN upconverter. The PPLN crystal is phase matched for horizontal (in plane) polarization, denoted by $\updownarrow$ in Fig. 6-1. Thus, only the horizontally-polarized input at the wavelength $\lambda_1 = 2\pi c/\omega_1$ is upconverted in its first pass, from right to left, through the crystal. The vertically-polarized (out-of-plane) λ_1 input, denoted by $\bullet$ in Fig. 6-1, is not phase matched and thus unaffected during its right-to-left passage through the crystal. At the output of the forward passage, both the input and upconverted light are reflected with $\pi/2$ polarization rotations via double passes through quarter-wave plates QWP1 and QWP2, respectively. In the backward direction, from left to right, the unconverted probe at λ_1, initially vertically polarized at the input, is now polarized horizontally and thus is upconverted to λ_2. The light that was upconverted in the forward direction is now vertically polarized, and not being phase matched does not undergo any nonlinear interaction during its return path through the crystal. At the output, the two upconverted polarizations combine to yield a beam that is a $\pi/2$ polarization-rotated upconverted replica of the input light provided that the λ_1 and λ_2 paths are phase locked to each other.

6.2 Experimental Setup for Polarization-Preserving Frequency Upconversion

We have implemented the polarization-insensitive frequency upconversion scheme (Fig. 6-1) described above using the setup shown in Fig. 6-2. We used a compact 400-mW cw Nd:YAG laser (Lightwave Electronics 122) operating at 1064.2 nm as our pump source. From our previous fixed-polarization single-photon upconversion work, [34, 35] the required pump power for unity conversion efficiency is $P_{\max} \approx 35\,\mathrm{W}$. A figure-8 pump enhancement standing-wave cavity with a finesse of ~130 was used to boost the circulating pump power to ~15 W, at which point the intrinsic conversion

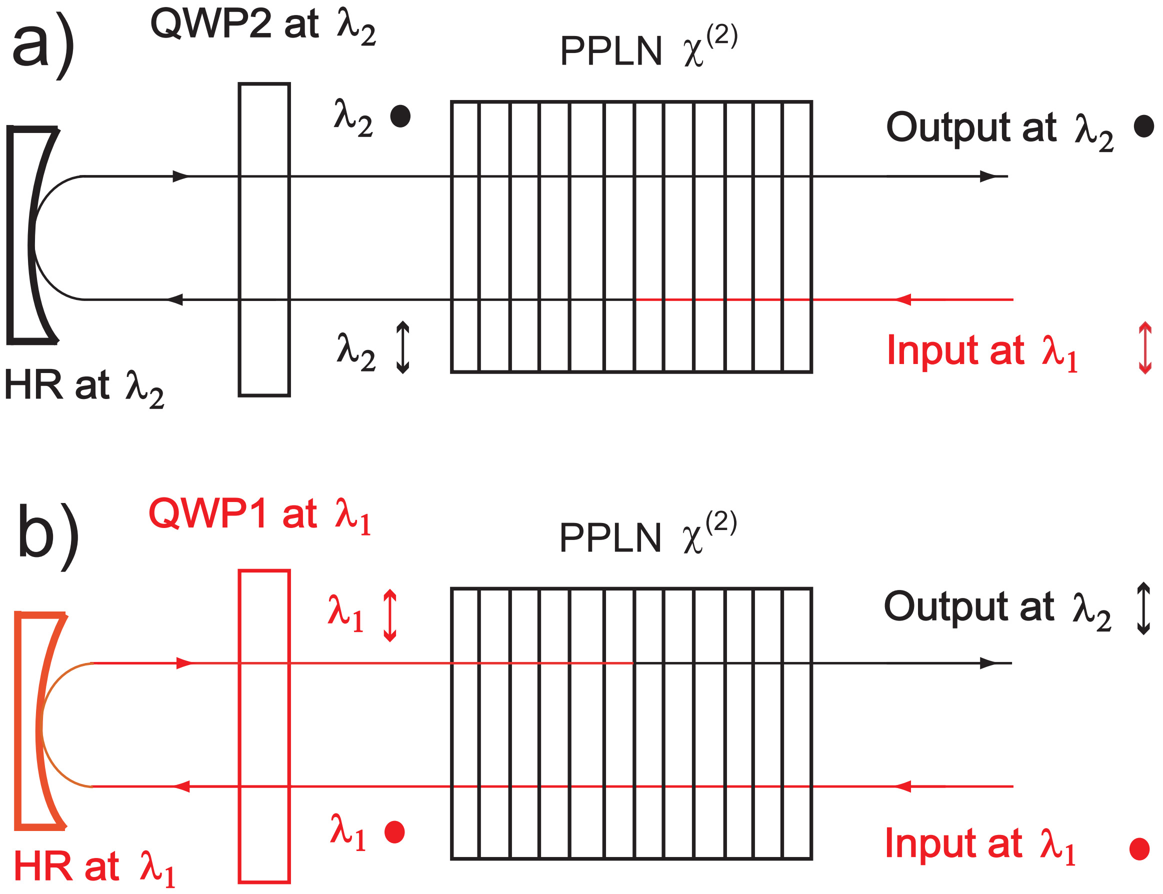

Figure 6-1: Polarization-preserving frequency conversion scheme using type-I phase matching in PPLN. a): Horizontally-polarized input light (↕) at λ_1 is upconverted to λ_2 as it travels from right to left through the crystal. b): Vertically-polarized input light (●) at λ_1 is 90°-rotated and then upconverted to λ_2 as it passes from left to right through the crystal. QWP1(2): quarter-wave plate for $1.55\,\mu$m (633 nm); HR: high reflector. For clarity, the horizontally-polarized pump beam is not shown here. In the actual realization of this scheme we only use one PPLN crystal.

efficiency is estimated to be 73%. The cavity was single-pass for the probe input at $\lambda_1 = 1.561\,\mu$m and the upconverted signal at $\lambda_2 = 633\,$nm. The 40-mm-long × 0.5-mm-thick bulk 5%-molar magnesium oxide-doped PPLN (MgO:PPLN) crystal was placed at the center of the pump enhancement cavity. The crystal was a multi-grating PPLN with 6 gratings, ranging from 11.2 to 12.2 μm in 0.2 μm steps. Each grating channel was 0.8-mm-wide, and the gap between the gratings was 0.06 mm. The crystal's faces were triple-wavelength anti-reflection coated at the pump (<0.3%), input (<0.5%), and output (<1.5%) wavelengths. The MgO:PPLN crystal was housed in an oven set at ∼89°C for first order, type-I, quasi-phase matched sum-frequency generation of $\lambda_2 = 633\,$nm from inputs at $\lambda_1 = 1561\,$nm and $\lambda_P = 1064.2\,$nm using the 11.8-μm grating. The oven was controlled to within ±0.1°C using a commercial temperature controller. The 75-mm radius-of-curvature mirrors M1 and M2 were coated for high reflection (HR) at λ_P (∼99.9%) and high transmission (HT) at λ_1 (∼96%) and λ_2 (∼93%). M3 was a 2.15% flat coupler for the pump, and the leakage through the flat HR mirror M4 ($T \sim 0.07 \times 10^{-3}$ at normal incidence) was used to monitor the circulating pump power (P_P) inside the cavity using a high-speed amplified InGaAs detector with adjustable gain (ThorLabs PDA400).

Figure 6-3 shows a detailed view of the Michelson interferometer. A triangular sweep voltage (V) can be applied to the PZT attached to one of the highly-reflecting mirrors in order to scan the length (L2) of one of the arms of the interferometer. We used a side-lock technique to phase-stabilize the interferometer. A block diagram of the side-locking electronics used to stabilize the Michelson interferometer is shown in Fig. 6-4. A picture of the experimental setup is shown in Fig. 6-5 (all of the numerous optical components shown in the picture are needed). The standing wave cavity is at the center of the picture. The 4-cm-long Mg:O PPLN crystal is located inside the black oven (denoted by the arrow) that sits on top of a multi-axis stage which allows one to adjust the x, y, z, tilt, and rotation. Figure 6-6 shows a photograph of the main part of the polarization-insensitive upconverter. The pump light travels back and forth between the two flat high-reflectors inside the standing wave cavity. The direction is indicated by the overlaying lines in Fig. 6-6.

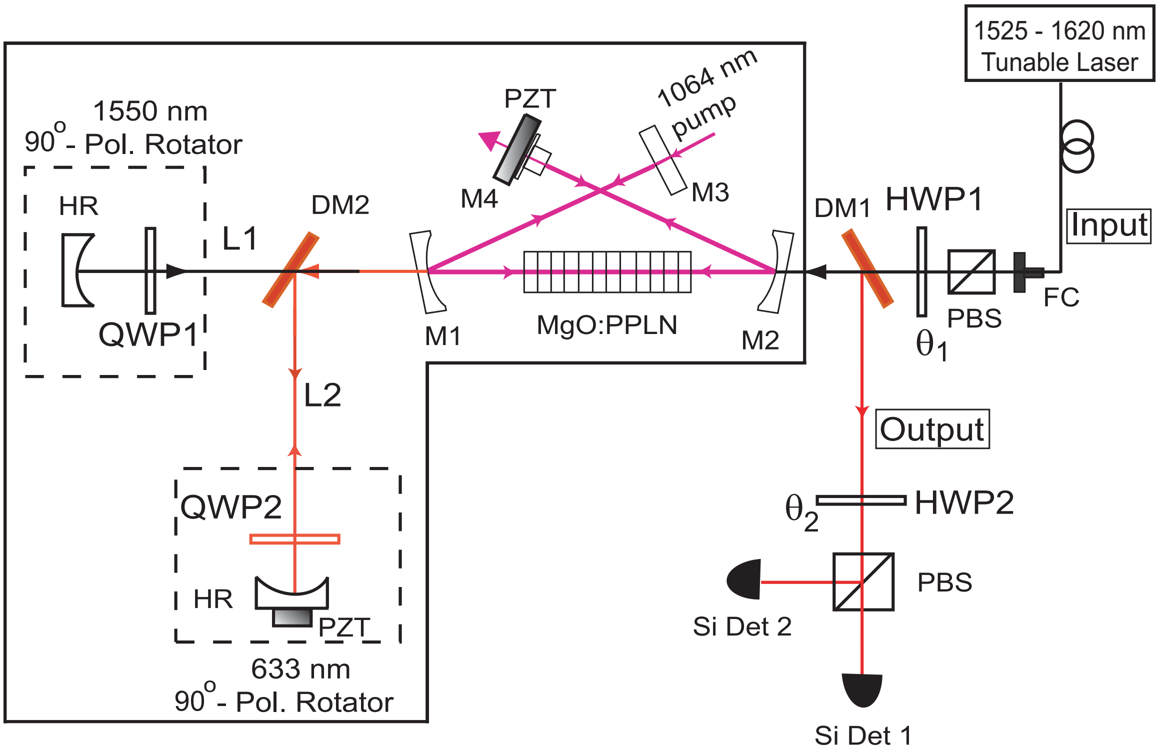

Figure 6-2: Experimental implementation of the polarization-preserving frequency upconversion scheme shown in Fig. 6-1. FC: fiber-optic collimator; PBS: polarizing beam splitter; DM1(2): dichroic mirrors; HWP1(2): half-wave plates for 1.55 μm (633 nm); QWP1(2): quarter-wave plates for 1.55 μm (633 nm); HR: high reflector; PZT: piezoelectric transducer. The solid box encloses the polarization preserving upconverter. The electronics for the cavity and Michelson servo-locking are omitted for clarity.

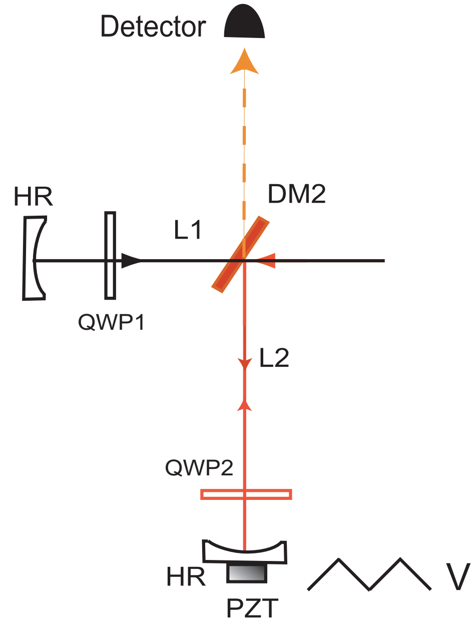

Figure 6-3: Detailed view of the upconverter interferometer. The signal on the unused port of the interferometer is used to lock the Michelson interferometer at the correct phase using a side-lock technique. We permit an asymmetry in the lengths L1 and L2 to allow for timing compensation.

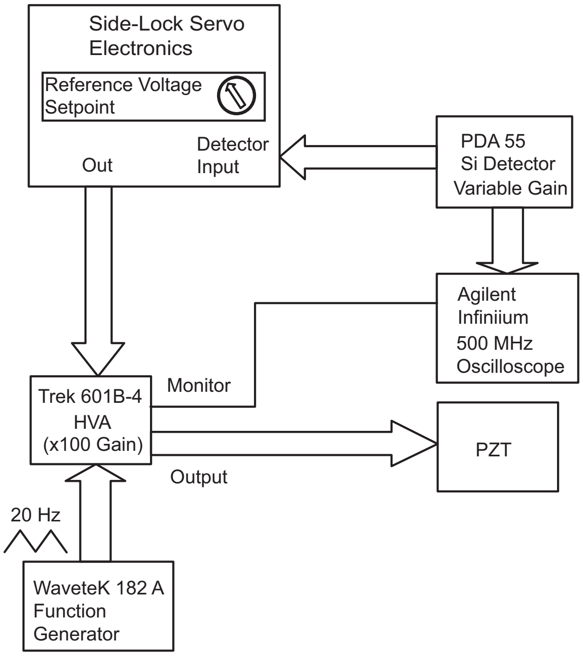

Figure 6-4: Block diagram of the components used to lock the Michelson interferometer at the correct phase using a side-lock technique.

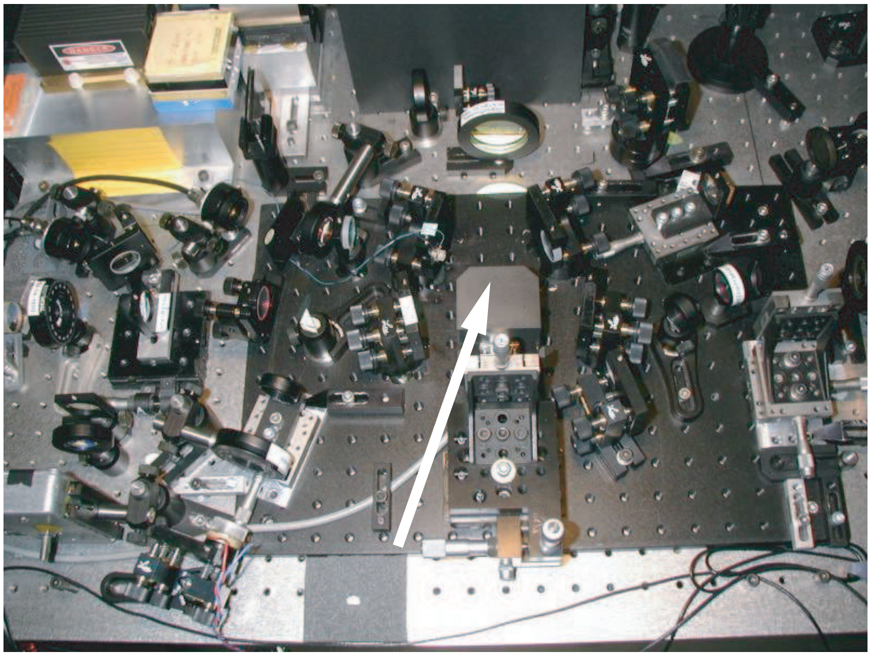

Figure 6-5: Photograph of the experimental setup for polarization-independent frequency upconversion. The standing wave cavity and the crystal oven (rectangular box denoted by the arrow) are situated in the center of the picture.

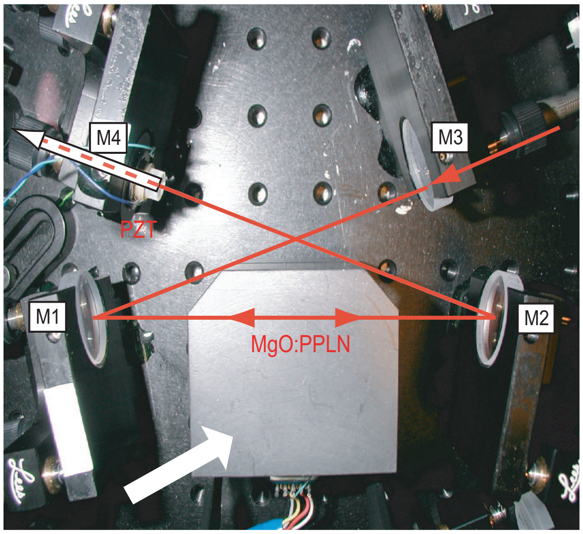

Figure 6-6: Photograph of the standing wave cavity and the crystal oven (rectangular box denoted by the arrow). The solid lines indicate the direction of light travel inside the cavity. The dashed line is the leakage through the small cavity high-reflector which is used to stabilize the cavity.

The pump beam at 1064 nm was sent through a Faraday isolator, to prevent back reflections, followed by a half-wave plate (HWP) and polarizing beam splitter (PBS) that together functioned as a variable attenuator. The polarization of the pump beam was rotated by a second HWP to be horizontal, aligned with the crystal's z-axis. For clarity these 4 optical elements, which precede the pump beam's entry into the cavity through mirror M3 (input coupler), as well as the electronics for stabilizing the cavity and Michelson interferometer are not shown in Fig. 6-2. The circulating pump leakage out of the cavity, through M4, was used to monitor the intra-cavity pump power and for cavity-length stabilization. The cavity was servo-locked to the pump transmission peak using a dither-and-lock servo feedback loop. The electronics used for this purpose are similar to the feedback circuitry used in the ring cavity upconversion experiments and will not be shown again here.

Figure 6-7 shows an oscilloscope trace of the standing wave cavity transmission peaks as monitored through mirror M4 by the InGaAs photodiode (see Fig. 6-1). A triangular voltage sweep was applied to the cavity PZT and the transmission peaks for the leading and lagging voltage slopes are clearly visible. Significant thermal hysteresis is again present, as it was in the ring cavity upconversion experiments. However, the broadening of the transmission peak on the leading edge of the cavity sweep is approximately 50% wider than the corresponding broadening observed in the ring cavity experiments. This effect happens at the expense of a significant narrowing of the transmission peak on the opposite, lagging, slope of the cavity sweep voltage. We typically locked the cavity at the peak of the broad transmission resonance, as indicated by the arrow in Fig. 6-7. The performance of the upconverter was investigated with a single-mode coherent field from a cw laser whose photon statistics were governed by the usual Poisson distribution. The probe light was supplied by a 4-mW cw fiber-coupled Fabry-Perot laser (Agilent HP81689A), tunable from 1.524 to 1.576 μm. The power of the input probe light was controlled with the 100-dB fiber-coupled optical attenuator (JDS Uniphase HA9) that we had used in our polarization-selective experiments. For operation at the single-photon level, we highly attenuated the probe beam. The input to the bidirectional upconverter was a

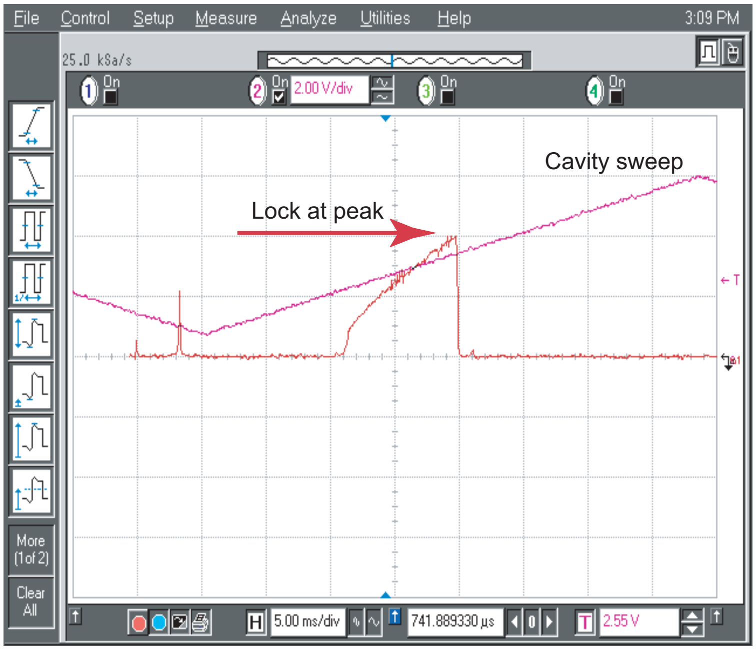

Figure 6-7: Standing wave cavity thermal hysteresis in the cavity sweep mode at high pump power. Top trace: PZT voltage sweep. Lower trace: resonances on the rising and falling edge of the cavity sweep voltage.

coherent field with an average flux of ∼0.025 photon per 25-ns measurement interval, which is low enough to neglect multiphoton events. Polarization adjustment for the 1.56-μm light was achieved with a PBS and a HWP, as shown in Fig. 6-2.

The standing-wave pump cavity allowed efficient upconversion (up to ∼55%, limited by the pump power) of continuous-wave light in both the forward and backward directions. The setup is also capable of upconverting pulsed light as long as the pulse bandwidth is less than the crystal's phase-matching bandwidth. The temporal pulse acceptance width of the upconverter is inversely proportional to the length of the PPLN crystal and, for typical interaction lengths of 1 to 5 cm, is on the order of several picoseconds. The cavity finesse and maximum circulating pump power were lower than in our previous experiment [35], because of the higher losses of our standing wave cavity compared with those of the ring cavity configuration. The multi-grating PPLN design along with temperature tuning allowed the upconverter to work for input wavelengths ranging from 1.52 to 1.66 μm, covering the entire C and L telecommunication bands. The upconverted light, in the red region of the visible spectrum, could be tuned from 627 to 645 nm, near the peak quantum efficiency window of Si single-photon counters. For example, using the 11.8 μm grating and operating at a temperature of 89°C the probe wavelength corresponding to peak upconversion was 1.561 μm. With a slight change in the PPLN temperature to 74°C and using the same grating, the peak probe wavelength could be translated to 1.557 μm resulting in a system tuning coefficient of $\sim$0.25 nm/°C.

The visible light was detected with a linear-mode Si APD with a large detection area and adjustable gain (ThorLabs PDA55). The input light was mode-matched into the standing-wave cavity after passing through a dichroic mirror (DM1). On the left side of the pump enhancement cavity in Fig. 6-2 a second dichroic mirror (DM2) separated the input probe at λ_1 and the upconverted light at λ_2 for $\pi/2$ polarization rotation and mode-matched reflection of the two beams back into the cavity. The dichroic mirrors were >99.9% reflective at 633 nm and had $\sim$98% transmission at 1561 nm. These values were nearly identical for both the vertical and horizontal polarizations at an angle of incidence of $\sim$10°. The polarization of the input light was set by the angle θ_1 of the input half-wave plate (HWP1). By adjusting the angle of HWP1 we could therefore select any linear polarization. When horizontally-polarized input light ($\updownarrow$) was sent through the cavity, upconversion occurred during the first pass, from right to left, through the PPLN crystal. When vertically-polarized input light ($\bullet$) entered the cavity, it was not immediately upconverted. In this case, the probe light passed through the dichroic mirror DM2 and was polarization-rotated by $\pi/2$ in a double pass through QWP1, thus preparing the probe light for upconversion during its second pass through the PPLN crystal. Therefore, in the backward (left-to-right) direction, upconversion occurred for λ_1 light that was initially vertically polarized. The dichroic mirror DM1 directed the total upconverted light to a half-wave plate (HWP2) set at angle θ_2 and a PBS for polarization analysis. The output light was detected with two Si detectors situated at the output ports of the PBS cube, as shown in Fig. 6-2. Along with the upconverted light at 633 nm, we measured some light which was generated at the second harmonic of the pump wavelength. This stray light was filtered out of the output with a prism along with spectral and spatial filtering, see Fig. 6-8.

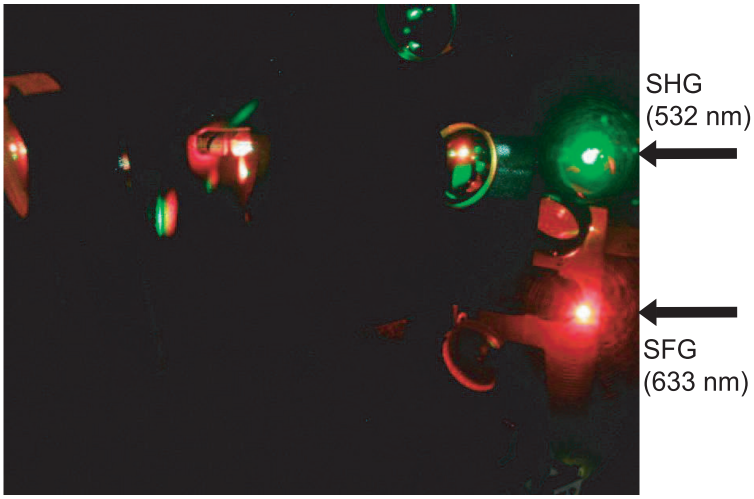

Figure 6-8: Photograph of the output of the polarization preserving upconverter in cw mode at high pump power. Along with the upconverted light at 633 nm (lower spot) we observed some SHG of the pump light (upper spot).

6.3 Polarization-Preserving Upconversion Results

Consider a single-photon input state of an arbitrary polarization

$$\vec{E}_{in} = H_{in}\vec{h} + e^{i\phi_{in}}V_{in}\vec{v} \tag{6.1}$$

at frequency ω_1, where $\vec{h}$ and $\vec{v}$ are the horizontal and vertical polarization unit vectors, respectively. The output state at frequency ω_2 after a double pass through the upconverter can be written as

$$\vec{E}_{out} = H_{out}\vec{v} + e^{i\phi_{out}}V_{out}\vec{h}\,. \tag{6.2}$$

where ϕ_{in} and ϕ_{out} are the input and output relative phases, respectively, and should be equal to each other for polarization-preserving upconversion. The input and output components are related by $H_{out} = \alpha_h\eta_h H_{in}$ and $V_{out} = \alpha_v\eta_v V_{in}$. Here, η^2 is the intrinsic upconversion efficiency and α^2 is the transmission through the bidirectionally pumped upconverter apparatus. We permit η and α to be different for the two polarizations to allow for potential differences in mode-matching efficiencies, as well as wavelength-dependent and polarization-dependent losses. Note the change in polarization vectors between the input and output states because of the $\pi/2$ polarization rotation at the dichroic Michelson interferometer, which can be easily corrected with the use of a HWP at the output. For polarization-preserving upconversion, it is necessary to have $H_{out}/H_{in} = V_{out}/V_{in}$, i.e., $\alpha_h\eta_h = \alpha_v\eta_v$, and $\phi_{out} = \phi_{in}$.

Figure 6-9 shows the signal at detector 1 (2) for the horizontally (vertically) polarized upconverted light as a function of input angle θ_1 of HWP1. The diagram just above the data shows the experimental configuration for the measurement. The input state is given by $\vec{E}_{in} = E_o(\cos 2\theta_1 \vec{h} + \sin 2\theta_1 \vec{v})$. For this measurement we removed HWP2 from the output beam path so that the output polarization at λ_2 was analyzed into H and V polarizations only. Therefore detector 1 (2) measures $|V_{out}|^2 = \alpha_v^2\eta_v^2 \sin^2 2\theta_1$ ($|H_{out}|^2 = \alpha_h^2\eta_h^2 \cos^2 2\theta_1$). The results shown in Fig. 6-9 clearly demonstrate that the outputs at the two detectors are sinusoidal, as expected, and that the overall conversion efficiencies for the two polarizations are matched, $\alpha_h^2\eta_h^2 = \alpha_v^2\eta_v^2$. Matching the upconversion efficiencies for horizontal and vertical polarizations is of course essential for quantum-state frequency conversion. Efficiency matching can always be achieved in our setup because our configuration employs two independent upconverter arms and we have the flexibility to insert a small amount of fixed attenuation into the higher-conversion arm to fine tune the balance between the forward and backward upconversion efficiencies. Figure 6-10 shows the net upconversion as a function of the input HWP1 angle without polarization-analyzing optics in the output beam path. The diagram just above the data shows the experimental configuration for the measurement. The output signal is given by

$$|H_{out}|^2 + |V_{out}|^2 = \alpha_h^2\eta_h^2 \cos^2 2\theta_1 + \alpha_v^2\eta_v^2 \sin^2 2\theta_1 \,. \tag{6.3}$$

Because we were able to match the overall conversion efficiencies for the two polarizations, $\alpha_h^2\eta_h^2 = \alpha_v^2\eta_v^2$, the total upconverted light level is constant, within the pump power fluctuations, regardless of the polarization state of the input light. This demon-

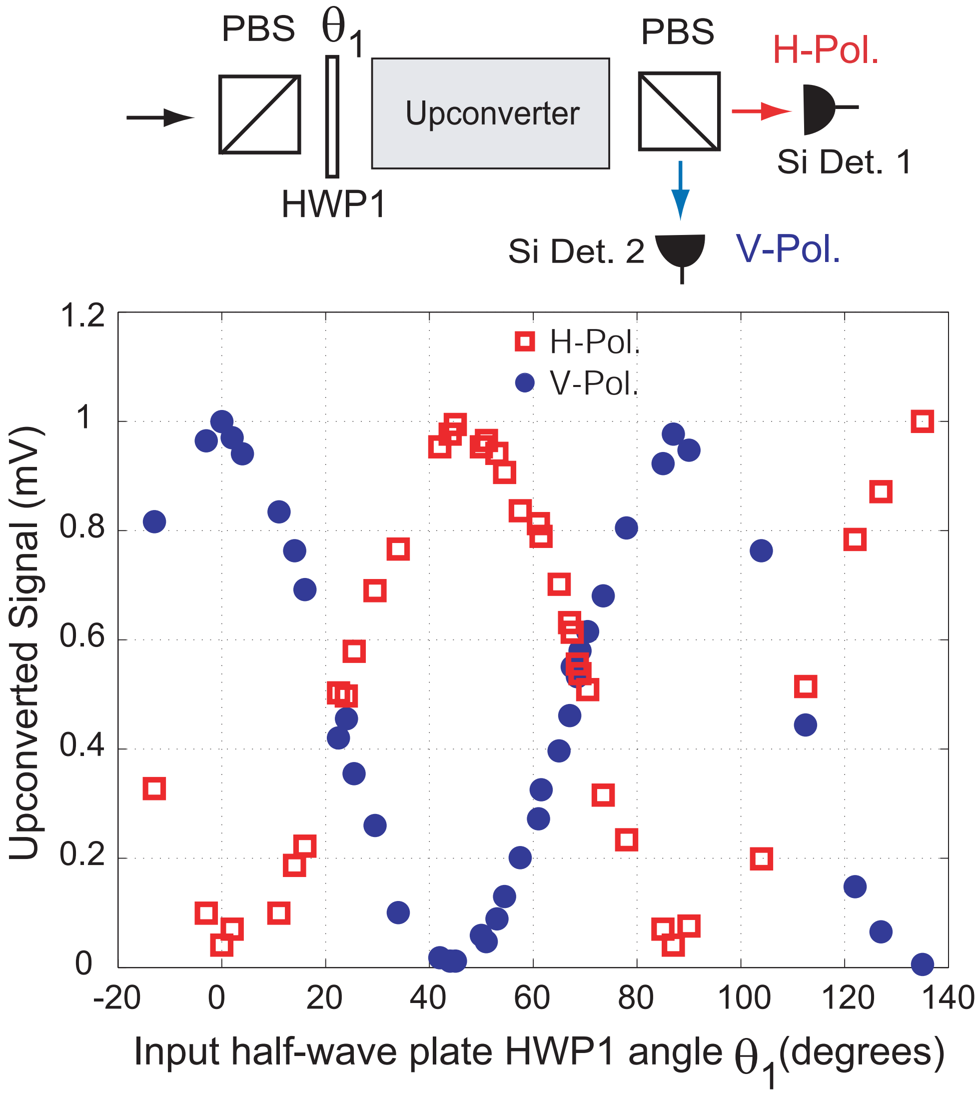

Figure 6-9: Upconverted outputs as a function of HWP1 angle θ_1. Top: measurement configuration. Bottom: experimental results for horizontally polarized (open squares) and vertically polarized (filled circles) outputs.

strates that the upconverter works equally well for all linearly-polarized inputs, i.e. it is polarization independent.

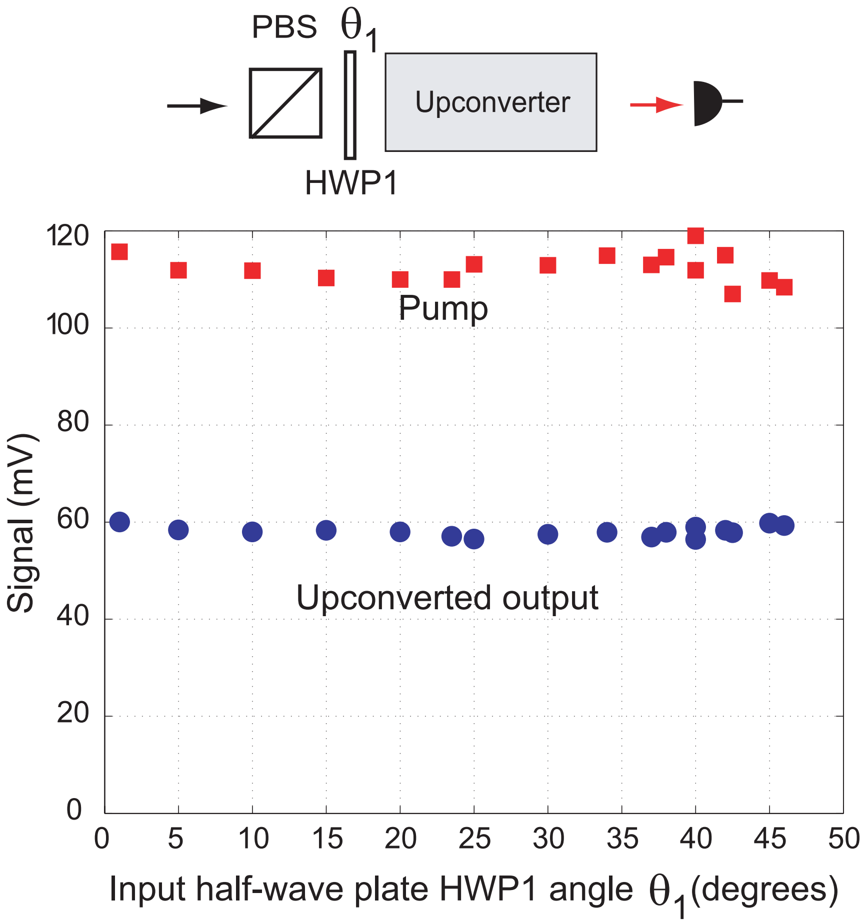

Figure 6-10: Polarization-independent upconversion output as a function of input half-wave plate HWP1 angle θ_1 without polarization-analyzing optics. Top: measurement configuration. Bottom: experimental results.

From Fig. 6-2 we note that the output polarization phase is determined by the forward and backward passages through the upconverter and the dichroic Michelson interferometer. The phase shift through the upconverter is caused by the crystal birefringence and dispersion at λ_1 and λ_2. The dichroic Michelson interferometer offers the easiest way to set the output phase properly by stabilizing the path length difference between the λ_1 and λ_2 paths. These two paths, L1 and L2, are formed by the dichroic mirror DM2 and the two high reflectors. To confirm the effect of the path length difference on the output phase ϕ_{out} we scanned the L2 path length with a PZT and observed the outputs after the polarization analyzer, as shown in Fig. 6-11. The diagram just above the data shows the experimental configuration. In this measurement, the input light was +45° linearly polarized by setting HWP1 angle to $\theta_1 = \pi/8$, such that $\vec{E}_{in} = E_o\vec{d}$, where the unit vectors $\vec{d} = (\vec{h} + \vec{v})/\sqrt{2}$, $\vec{a} = (\vec{h} - \vec{v})/\sqrt{2}$ define the two diagonal polarizations.

The output after the upconverter is given by

$$\vec{E}_{out} \propto \frac{E_o}{2}[(1 + e^{i\phi_{out}})\vec{d} - (1 - e^{i\phi_{out}})\vec{a}]\,. \tag{6.4}$$

$\vec{E}_{out}$ was polarization-analyzed along $\vec{d}$ and $\vec{a}$ by a combination of HWP2 set at $\theta_2 = \pi/8$ and a PBS, as shown in Fig. 6-11. Figure 6-11 clearly shows that the PZT sweep of path length L2 allowed the output phase ϕ_{out} to be swept in a smooth and predictable manner. This made it possible to lock the Michelson interferometer, which was required in order to stabilize the output phase. We used a side-lock technique to phase lock the Michelson interferometer, which is shown schematically in more detail in Fig. 6-3. The block diagram of the elements used for this purpose is shown in Fig. 6-4. We point out that the Michelson interferometer and the standing-wave cavity resonator had to be locked simultaneously – i.e. both the upconverter cavity and the interferometer had to be stabilized at the same time. At the highest resonating pump powers the servo became less stable due to heating of the crystal and multiple reflections off the PPLN faces. We chose to use the weak 1064-nm pump light that was incidentally transmitted through M1 (see Fig. 6-1) for the Michelson interferometer stabilization. The pump light was partially transmitted through and partially reflected by DM2 and traversed the same $L1$ and $L2$ path lengths as the input and upconverted light through the interferometer. A photodetector placed at the unused port of the Michelson interferometer was used to measure the 1064-nm interference signal. We applied a side-locking servo to stabilize the interferometer at the correct position. Alternatively, we could use the second harmonic of the pump—which was also generated, incidentally, in the non-phase matched MgO:PPLN crystal—for stabilization. Neither the 1.56 nor the 0.633 μm light was used for path length stabilization

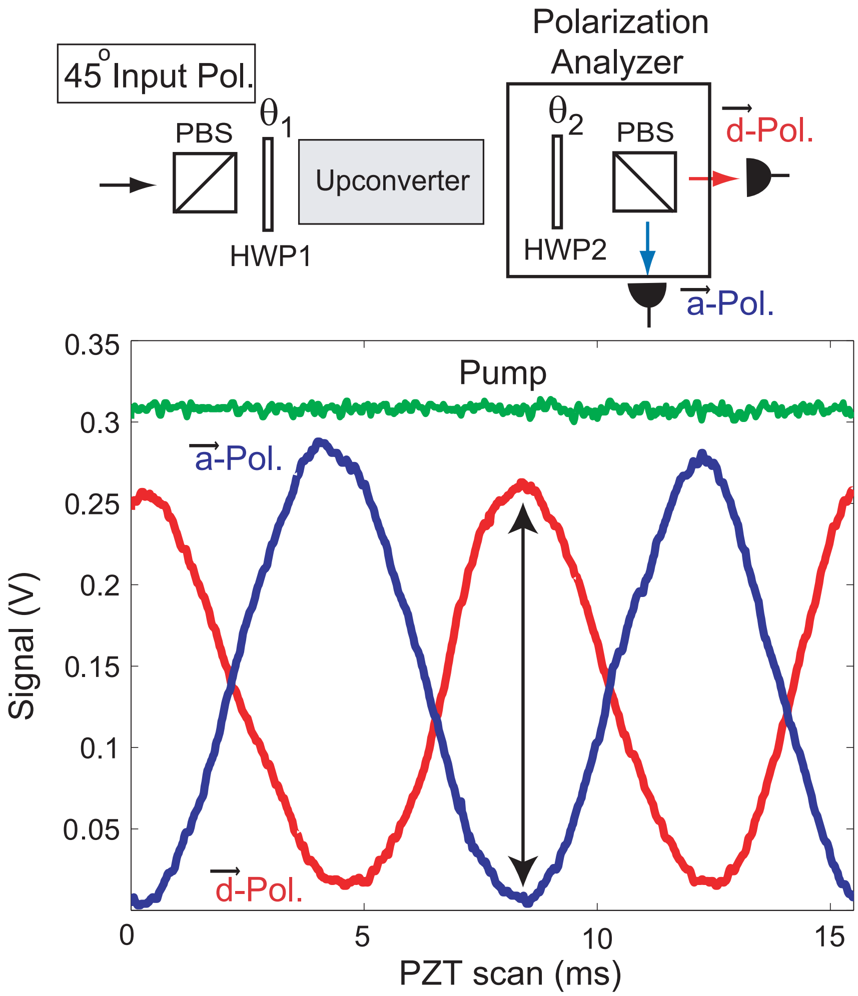

Figure 6-11: $\vec{d}$- and $\vec{a}$-polarized upconversion signal outputs as functions of upconverter interferometer PZT scan for +45° linearly polarized input (along $\vec{d}$). Top: measurement configuration. Bottom: experimental results; the arrow indicates the scan location at which the output field has the correct phase for polarization-state preservation. Here $\theta_1 = \theta_2 = \pi/8$.

because they could be at the single-photon level. Figure 6-12 shows the $\vec{d}$-polarized

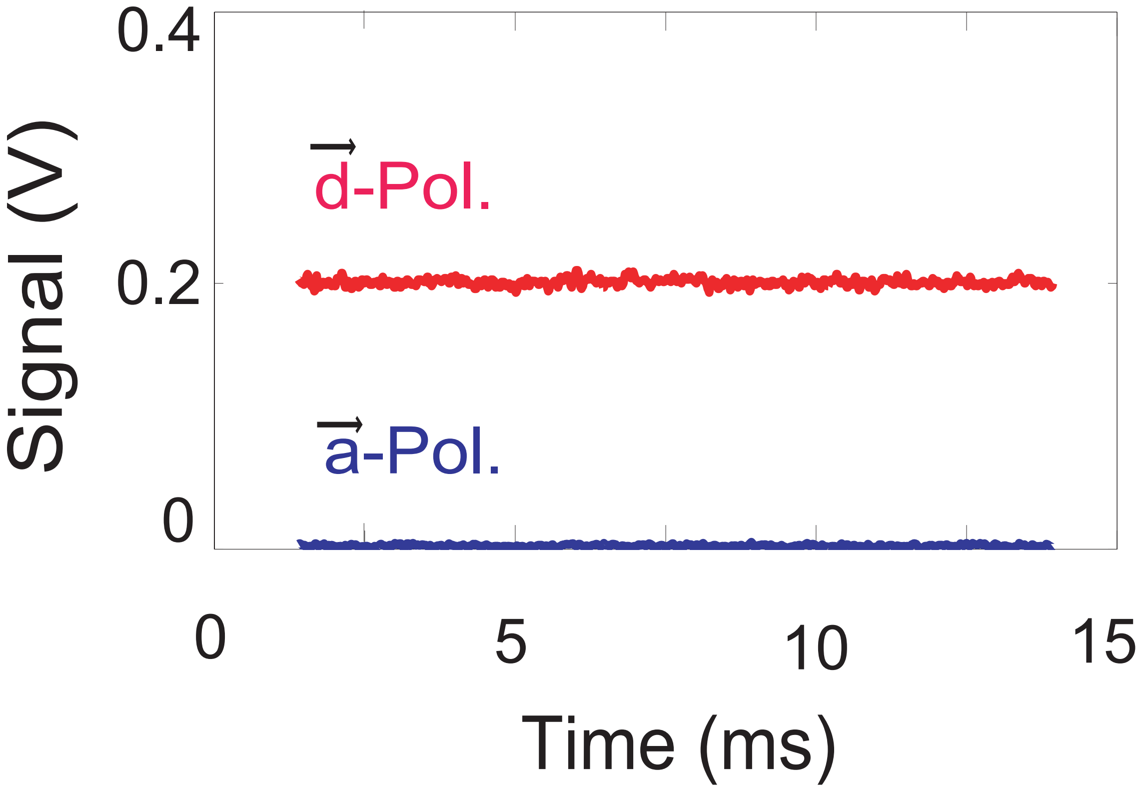

Figure 6-12: Upconversion signal analyzed after HWP2 along $\vec{d}$ and $\vec{a}$ polarization for +45° (along $\vec{d}$) polarized input under phase-locked conditions for the upconverter Michelson interferometer. The $\vec{a}$-polarized extinction is ~99%.

and $\vec{a}$-polarized outputs (see Fig. 6-11) with the dichroic Michelson interferometer servo locked to maintain the correct path length difference between L1 and L2. At the desired output phase, $\phi_{out} = \phi_{in}$, the $\vec{d}$-polarized output is maximized and the $\vec{a}$-polarized output is minimized, as clearly shown in Fig. 6-12. The steady outputs under servo-locked conditions suggest that the two upconverted fields H_{out} and V_{out} (or equivalently those along $\vec{d}$ and $\vec{a}$) were phase coherent, thus indicating the upconversion indeed preserved the polarization state. The non-zero output of ~1% in the $\vec{a}$-polarized port in Fig. 6-12 was likely the reflected leakage of the $\vec{d}$-polarized light due to an imperfect polarizing beam splitter. In minimizing the $\vec{a}$-polarized output using the HWP2 angle adjustment we estimate that the polarization phase angle uncertainty is ~1°.

The $\vec{d}$ and $\vec{a}$-polarized upconverted outputs under phase-locked conditions for the Michelson interferometer are shown in Fig. 6-13. The intrinsic upconversion efficiencies η_h^2 and η_v^2 were ∼50% for these experiments. We believe that polarization preservation with near-unity efficiency can be achieved in our setup by simply using a more powerful laser. Alternatively, one could boost the upconversion efficiency by employing greater resonant pump-power enhancement (a higher-finesse cavity) and by further optimizing the mode matching.

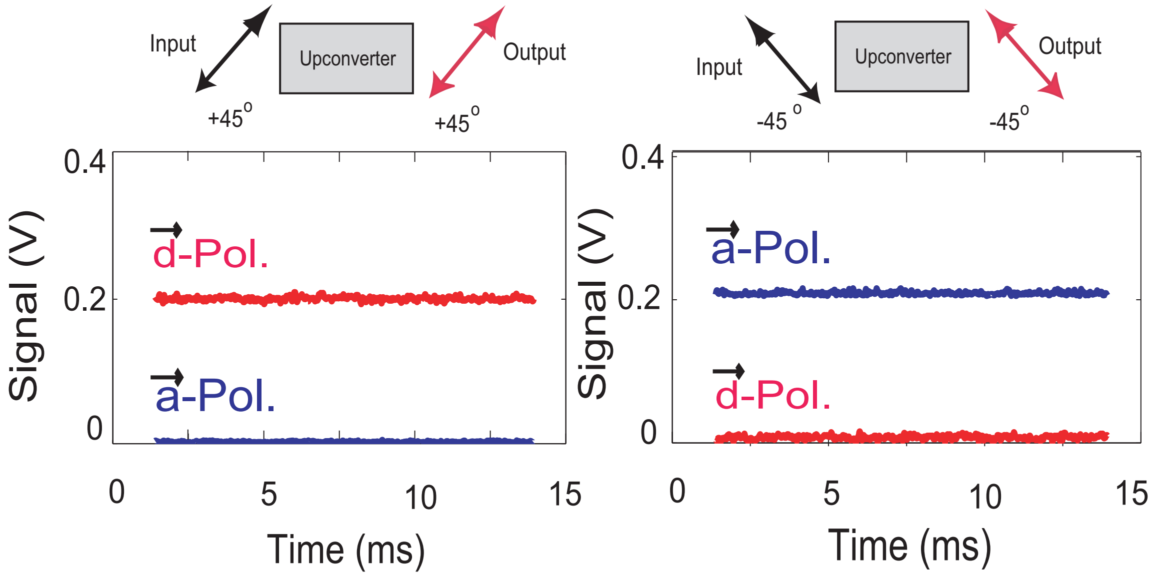

Figure 6-13: Upconversion signal analyzed after HWP2 along $\vec{d}$ and $\vec{a}$ polarizations for +45°-polarized (along $\vec{d}$) input (left panel) and -45°-polarized (along $\vec{a}$) input (right panel) under phase-locked conditions for the upconverter Michelson interferometer.

For upconversion at the single-photon level, we attenuated the input probe to ∼0.13 pW with a precision fiber-optic attenuator. This power level corresponded to an average flux of ∼1 photon/μs. The Poisson statistics governing the photon-number distribution for this source ensured that the probability of more than one photon entering the upconverter per measurement interval (∼25-ns long) was negligible. We note that the same photon number characteristics are applicable when the upconverter is used with a narrowband entangled-photon source, as long as the photon pairs are generated at low flux so that the probability of producing more than one pair per measurement time is low.

The experimental setup for these measurements was identical to that shown in Fig. 6-2, with a free-space single-photon counting module (PerkinElmer AQR-14) replacing the Si detector in the transmitted beam. We measured the upconverted counts for +45°-polarized input photons. At the correct phase, the $\vec{d}$-polarized output was again maximized which indicated that the upconversion indeed preserved the photon's polarization state. The single-photon upconversion results were obtained at an intrinsic conversion efficiency of ∼40%. Figure 6-14 below shows these results. Fig. 6-15 shows the single-photon upconversion as well as the extraneous counts measured by the Si SPCM for vertically-polarized input photons under phase-locked conditions. The polarization-preserving upconversion results at the single-photon level were consistent with those obtained in the low-power measurements, indicating that the cw upconversion scheme functioned well in the single photon as well as the low-power regime.

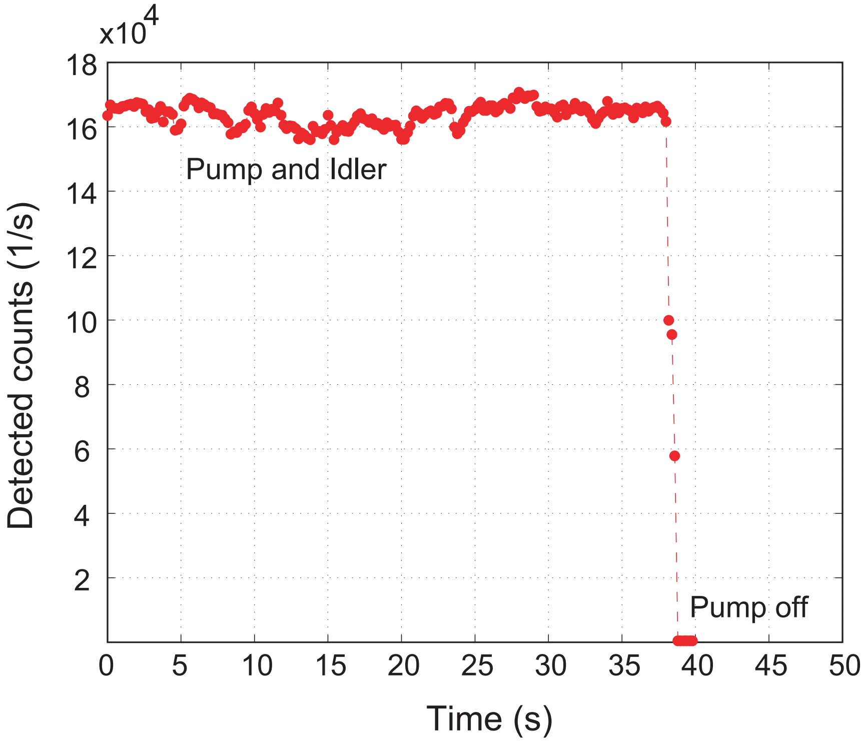

Figure 6-14: Single-photon upconversion signal analyzed after HWP2 along $\vec{d}$ polarization (with $\vec{a}$ minimized) for +45°-polarized (along $\vec{d}$) input under phase-locked conditions for the upconverter Michelson interferometer.

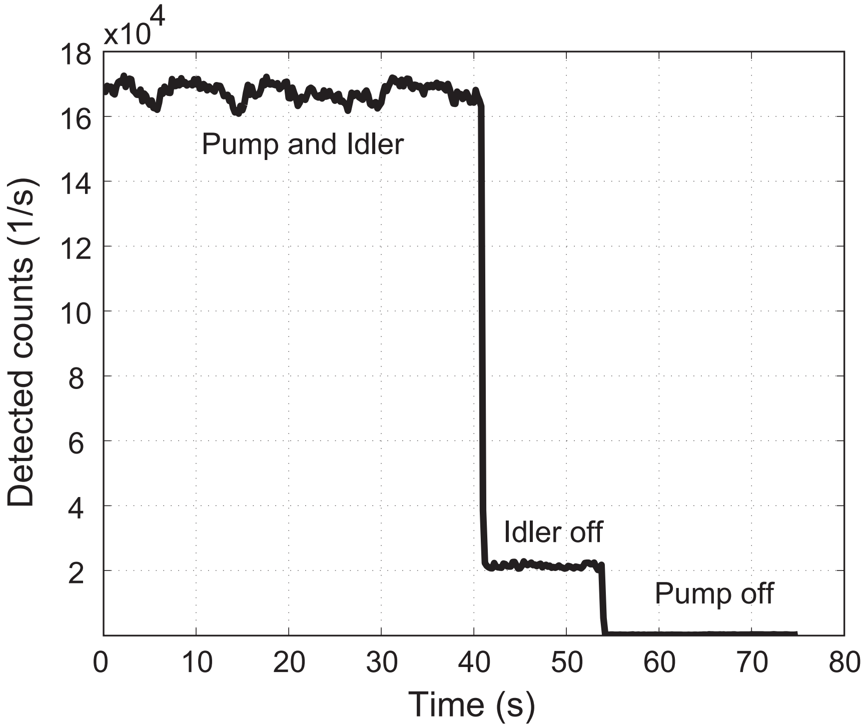

Figure 6-15: Single-photon upconversion signal for vertically-polarized input under phase-locked conditions for the upconverter Michelson interferometer.

6.4 Discussion

In order to implement quantum-state frequency conversion in our bidirectional setup, it is essential that the two upconverted fields combine in a phase coherent and indistinguishable fashion at the output. This is especially critical if this particular scheme is to be used for the teleportation-assisted long distance quantum communication protocol described in Chapter 1. The two spatio-temporal modes must be identical to avoid any form of distinguishability which would destroy the entanglement. Temporal mode matching is straightforward to implement by adjusting the relative path lengths, $L1$ and $L2$, of the two arms of the upconverter interferometer. We can estimate the temporal separation between the input and upconverted fields, caused by material dispersion, from the published refractive indices of $LiNbO_3$. Table 6.1 shows the indices of refraction for lithium niobate at a temperature of 89°C. We see

Notation	Definition
$n_o^o = n_o^{633} = 2.29792$	Ordinary refractive index at 633 nm
$n_e^o = n_e^{633} = 2.22784$	Extraordinary refractive index at 633 nm
$n_o^i = n_o^{1561} = 2.21594$	Ordinary refractive index at 1561 nm
$n_e^i = n_e^{1561} = 2.14542$	Extraordinary refractive index at 1561 nm

Table 6.1: Refractive indices of lithium niobate at the input and output wavelengths at a temperature of ∼89°C. The data is calculated from the Sellmeier equations reported in Reference [53].

that the following inequality is obeyed by the relevant indices of refraction of $\mathrm{LiNbO_3}$

$$n_o^o > n_e^o > n_o^i > n_e^i, \tag{6.5}$$

as defined in Table 6.1. After a dual pass through the PPLN crystal, the temporal separation that has accumulated between the horizontal and vertical polarization components of the output photons is $\delta t \sim 11\,\mathrm{ps}$. This corresponds to a free-space spatial separation of $\delta x = L[n_o^o - n_o^i] \sim 0.328$ cm. The proper timing compensation for the delay can be achieved by simply adjusting the separate path lengths traveled by the $0.633\,\mu$m and $1.56\,\mu$m light in the Michelson interferometer such that $L1 \sim L2 + \delta x/2$. Another way to temporally overlap the output would be to insert a birefringent compensating crystal, an unpoled piece of $\mathrm{LiNbO_3}$ for example, in the upconverter's output. Spatial mode matching can be achieved by adjusting the radii of curvature of the respective high-reflectors in the two independent upconversion arms. This could be done in situ with the cavity locked and at high conversion efficiency by using a weak probe input and measuring the confocal parameters of the respective upconverted outputs.

In conclusion, we have demonstrated efficient, cw, wavelength-tunable, polarization-preserving frequency upconversion of 1.56-μm light to the visible using a double-pass geometry in a single PPLN crystal. Our technique can be used to implement polarization-preserving quantum-state frequency translation for use in long-distance quantum communication architectures.

Chapter 7

Conclusion

7.1 Summary

Entanglement generation, transmission, long-term storage, conversion, and detection are several important resources and technologies which will be necessary for the realization of the novel quantum-based communication and computation infrastructure of tomorrow. In this thesis, we investigated several essential components of an entanglement-based architecture for long-distance quantum communication. The MIT/NU teleportation-based long distance quantum communication protocol requires an efficient and spectrally bright high-flux source of polarization-entangled photons at 795 nm for the loading of a local Rb memory and 1550 nm for low-loss fiberoptic delivery to a remote Rb atom. Efficient loading of the remote Rb memory depends on quantum frequency upconversion of the polarization-entangled idler light in order to match the photons to the absorption line of the atoms. The main accomplishments of this work were the demonstration of efficient upconversion of individual photons of fixed as well as arbitrary polarization, progress on the efficient generation of entangled light, as well as single-photon detection at 1.55 μm.

In Chapter 2 we described the main features of a source of polarization entanglement at $\sim$0.8 and 1.6 μm with an inferred bandwidth of $\sim$60 GHz and a spectral brightness of 300 pairs/s/GHz/mW of pump power. In Chapter 2 we also reported very good photon-counting performance at 1.55-μm with custom-built detectors capable of ∼20% quantum efficiency and dark-count probabilities of 0.16% per 20-ns gate. These photon-counting receivers have been used in a variety of quantum optical experiments perfomed in our group at MIT and at Lincoln Laboratory.

Efficient frequency translation at the single-photon level, never implemented until now, is central to several long-distance teleportation-based quantum communication architectures, such as those recently proposed in the literature. In Chapter 4 we demonstrated 90%-efficient polarization-dependent upconversion of single photons at 1.55 μm. This upconverter, when followed by a Si single-photon counter, also has applications in power-limited classical optical communications, eye-safe ranging, and imaging. Efficient upconversion affords photon-counting capabilities at wavelengths in the low loss fiberoptic and atmospheric transmission windows that are far in excess (e.g., ∼60% quantum efficiency, continuous-wave operation) of what is currently possible with semiconductor-based photon counting detectors such as those described in Chapter 2. Our scheme for near-unity upconversion used a high-finesse traveling wave cavity for the pump beam that was servo-locked to the pump transmission peak for high-power continuous-wave operation. In comparison with polarization-selective upconversion in a waveguide, our scheme is attractive because it uses commercial optical components and has the potential for the lowest overall losses.

The process of entanglement storage and long-distance teleportation relies on the coherent quantum information transfer between those photons that are suitable for long-distance transmission over standard single-mode optical fibers (∼1.55 μm) and photons that have the wavelength which matches the alkaline atomic transitions (∼750-850 nm). A novel kind of frequency upconverter is required to perform this specialized function. The necessary device is a quantum frequency translator which must serve as an interface between the flying qubits, the polarization-entangled photons, and the standing qubits, represented by cavity-trapped atoms. This device has to work efficiently with low insertion loss down to the single photon level. More importantly, however, the frequency-conversion process performed by this quantum interface has to take place without affecting the polarization state of the entangled photons, which is required in order to preserve their coherence. In Chapter 5 we explored several potential configurations that meet the stringent requirements for polarization-independent quantum-state upconversion.

In Chapter 6 we demonstrated a polarization-preserving upconversion technique that allows for the coherent transfer of arbitrary polarization states between photons at vastly different wavelengths. The input and output wavelengths of the upconverter can be tuned over a wide spectral range by changing the temperature of the nonlinear crystal and the pump wavelength. We implemented efficient polarization-preserving wavelength translation using bi-directional upconversion in a standing wave optical resonator, where the input horizontal (vertical) polarization was converted in the forward (backward) direction. A dichroic Michelson interferometer was stabilized using a side-lock method to lock the relative phase and maintain the polarization angle, thus maintaining the polarization state of the input light.

7.2 Future Work and Concluding Remarks

Future work could further improve the efficiency, stability, and overall compactness of our polarization-selective and polarization-preserving upconverters. An attractive alternative to polarization-preserving upconversion in a standing wave cavity with an external dichroic Michelson interferometer is the implementation of upconversion in a Sagnac interferometer. This could be achieved by using the configuration introduced in Chapter 5. In order to reduce the extraneous counts present in the output of the upconverters at high conversion efficiency, it is desirable to choose a different set of wavelengths for operation. A good choice would be to upconvert 1.55-μm light by using a pump derived from an EDFA-laser at $\sim$1.6 μm. For an upgraded version of the frequency upconverters described in this thesis, one might consider reducing the complexity introduced by the traveling and standing wave resonators by using a very strong pump laser or short pulses with high peak intensities in a single pass configuration.

The field of quantum information processing is rapidly growing. The implementation of polarization-preserving frequency conversion will enable the fiberoptic distribution of entanglement and the loading of remote atomic quantum memories. This will allow for the realization of novel architectures for teleportation-based long distance quantum optical communication. Technological advances in these areas will alter the way we communicate, compute, measure, and interact with the world surrounding us. The progress reported in this thesis should help move the concept of quantum communications away from the realm of laboratory demonstrations and closer to viable system implementations.

Bibliography

[1] L.-M. Duan, M. D. Lukin, J. I. Cirac, and P. Zoller. Long-distance quantum communication with atomic ensembles and linear optics. *Nature* **414,** 413 (2001). 23, 24

[2] J. H. Shapiro. Architectures for long-distance quantum teleportation. *New Journal of Physics* **4,** 47.1 (2002). 11, 17, 23, 24, 25, 26, 34, 89, 101, 103

[3] S. Lloyd, M. S. Shahriar, J. H. Shapiro, and P. R. Hemmer. Long-distance unconditional teleportation of atomic states via complete Bell state measurements. *Physical Review Letters* **87,** 167903 (2001). 23, 24, 25

[4] E. Schrödinger. Discussion of Probability Relations Between Separated Systems. *Proceedings of the Cambridge Philosophical Society* **31,** 555 (1935); also **32,** 446 (1936). 23

[5] *The Physics of Quantum Information: Quantum Cryptography, Quantum Teleportation, Quantum Computation*, edited by D. Bouwmeester, A. Ekert, and A. Zeilinger, Berlin: Springer-Verlag, 2000. ISBN 3540667784. 23, 24

[6] A. Aspect, J. Dalibard, and G. Roger. Experimental test of Bell's inequalities using time-varying analyzers. *Physical Review Letters* **49,** 1804 (1982). 23

[7] A. Einstein, B. Podolsky, and N. Rosen. Can quantum-mechanical description of physical reality be considered complete? *Physical Review* **47,** 777 (1935). 23

[8] J. S. Bell. On the problem of hidden variables in quantum mechanics. *Review of Modern Physics* **38,** 447 (1966). 23

[9] J. S. Bell. *Speakable and Unspeakable in Quantum Mechanics*. Cambridge University Press, 1987. ISBN 0521368693. 23

[10] P. Kwiat, K. Mattle, H. Weinfurter, and A. Zeilinger. New high-intensity source of polarization-entangled photon pairs. *Physical Review Letters* **75,** 4337 (1995). 24, 33

[11] P. G. Kwiat, E. Waks, A. G. White, I. Appelbaum, and P. H. Eberhard. Ultrabright source of polarization-entangled photons. *Physical Review A* **60,** R773 (1999); M. Oberparleiter and H. Weinfurter. Cavity-enhanced generation of polarization-entangled photon pairs. *Optics Communications* **183,** 133 (2000). 24, 33, 99

[12] S. Tanzilli, H. De Riedmatten, W. Tittel, H. Zbinden, P. Baldi, M. De Micheli, D. B. Ostrowsky, and N. Gisin. Highly efficient photon-pair source using periodically poled lithium niobate waveguide. *Electronics Letters* **37,** 26 (2001). 24

[13] C. H. Bennett, G. Brassard, C. Crepeau, R. Jozsa, A. Peres, and W. K. Wootters. Teleporting an unknown quantum state via dual classical and Einstein-Podolsky-Rosen channels. *Physical Review Letters* **70,** 1895 (1993). 24

[14] M. A. Nielsen and I. L. Chuang. *Quantum Computation and Quantum Information*. Cambridge University Press, 2000. ISBN: 0521635039. 24

[15] V. Giovannetti, S. Lloyd, and L. Maccone. Quantum-enhanced measurements: beating the standard quantum limit. *Science* **306,** 1330 (2004). 24

[16] Quantum Imaging, Special Issue, J. P. Dowling, A. Gatti, A. Sergkienko, Eds., *Journal of Modern Optics* **53,** March-April (2006). 24

[17] A. Ekert, J. Rarity, P. Tapster, and G. Palma. Practical quantum cryptography based on two-photon interferometry. *Physical Review Letters* **69,** 1293 (1992). 24

[18] N. Gisin, G. Ribordy, W. Tittel, H. Zbinden. Quantum cryptography. *Review of Modern Physics* **74,** 145 (2002). 24

[19] D. S. Bethune and W. P. Risk. Autocompensating quantum cryptography. *New Journal of Physics* **4,** 42.1 (2002). 24

[20] D. Stucki, N. Gisin, O. Guinnard, G. Ribordy, and H. Zbinden. Quantum key distribution over 67 km with a plug and play system. *New Journal of Physics* **4,** 41.1 (2002). 24

[21] R. J. Hughes, J. E. Nordholt, D. Derkacs, and C. G. Peterson. Practical free-space quantum key distribution over 10 km in daylight and at night. *New Journal of Physics* **4,** 43.1 (2002). 24

[22] J. H. Shapiro and N. C. Wong. An ultrabright narrowband source of polarizationentangled photon pairs. *Journal of Optics B: Quantum and Semiclassical Optics* **2,** L1 (2000); J. H. Shapiro. Long-distance high-fidelity teleportation using singlet states. *Quantum Communication, Measurement, and Computing* **3**, pages 367-374. Kluwer, New York, NY, 2001. 24, 34, 38

[23] P. Kumar. Quantum frequency conversion. *Optics Letters* **15,** 1476 (1990). 27, 95

[24] A. Lacaita, F. Zappa, S. Cova, and P. Lovati. Single-photon detection beyond 1 μm: performance of commercially available InGaAs/InP detectors. *Applied Optics* **35,** 2986 (1996). 27, 41

[25] D. Stucki, G. Ribordy, A. Stefanov, H. Zbinden, J. G. Rarity, and T. Wall. Photon counting for quantum key distribution with Peltier cooled InGaAs/InP APDs. *Journal of Modern Optics* **48,** 1967 (2001). 27, 41

[26] D. S. Bethune, W. P. Risk, and G. W. Pabst. A high-performance integrated single-photon detector for telecom wavelengths. *Journal of Modern Optics* **51,** 1359 (2004). 27, 41

[27] M. A. Albota. Single-photon detection of 1.55 μm entangled light and frequency upconversion in periodically poled lithium niobate for quantum optical communication. Master of Science Thesis, MIT, June 2002. 27, 39, 41, 63

[28] M. A. Albota and E. Dauler. Single-photon detection of degenerate photon pairs at 1.55 μm from a periodically poled lithium niobate parametric downconverter. *Journal of Modern Optics, Special Issue on Single Photon Detectors, Applications, and Measurement Methods* **51**, No. 9-10, 1417 (2004). 27, 39, 41, 43

[29] M. A. Albota, R. M. Heinrichs, D. G. Kocher, D. G. Fouche, B. E. Player, M. E. OBrien, B. F. Aull, J. J. Zayhowski, J. Mooney, B. C. Willard, and R. R. Carlson. Three-dimensional imaging laser radar with a photon-counting avalanche photodiode array and microchip laser. *Applied Optics* **41,** 7671 (2002). 27

[30] B. F. Aull, A. H. Loomis, D. J. Young, R. M. Heinrichs, B. J. Felton, P. J. Daniels, and D. J. Landers. Geiger-mode avalanche photodiodes for three-dimensional imaging. *Lincoln Laboratory Journal* **13,** 335 (2002). 27

[31] E. J. Mason, M. A. Albota, F. König, and F. N. C. Wong. Efficient generation of tunable photon pairs at 0.8 and 1.6 μm. *Optics Letters* **27,** 2115 (2002). 28, 37

[32] F. König, E. J. Mason, F. N. C. Wong, and M. A. Albota. Efficient and spectrally bright source of polarization-entangled photons. *Physical Review A* **71**, 033805 (2005). 28, 38, 40

[33] J. F. Clauser, M. A. Horne, A. Shimony, and R. A. Holt. Proposed experiment to test local hidden-variable theories. *Physical Review Letters* **23,** 880 (1969). 28

[34] M. A. Albota and F. N. C. Wong. Efficient single-photon counting at 1.55 μm via frequency upconversion. Postdeadline Paper **QThPDB11**, in *Quantum Electronics and Laser Science Conference (QELS)*, Vol. 89 of OSA Trends in Optics and Photonics Series, Baltimore, MD, May 2003. 29, 57, 75, 90, 110

[35] M.A. Albota and F.N.C. Wong. Efficient single-photon counting at 1.55 μm by means of frequency upconversion. *Optics Letters*, **29,** 1449 (2004). 29, 55, 57, 75, 90, 110, 117

[36] M. A. Albota, F. N. C. Wong, and J. H. Shapiro. Polarization-independent upconversion for high-efficiency photon counting and quantum optical communication. Postdeadline Paper **ThPD5**, in *OSA Conference on Nonlinear Optics* (NLO), Waikoloa, HI, August 2004. 29

[37] M. A. Albota, F. N. C. Wong, and J. H. Shapiro. Polarization-independent frequency conversion for quantum optical communication. *Journal of the Optical Society of America B* **23,** 918 (2006). 29

[38] K. Banaszek, A. B. U'rem, and I. A. Walmsley. Generation of correlated photons in controlled spatial modes by downconversion in nonlinear waveguides. *Optics Letters* **26,** 1367 (2001). 33

[39] C. Kurtsiefer, M. Oberparleiter, and H. Weinfurter. High-efficiency entangled photon pair collection in type-II parametric fluorescence. *Physical Review A* **64,** 023802 (2001). 33

[40] J. A. Armstrong, N. Bloembergen, J. Ducuing, and P. S. Pershan. Interactions between light waves in a nonlinear dielectric. *Physical Review* **127,** 1918 (1962). 33, 63

[41] M. M. Fejer, G. A. Magel, D. H. Jundt, and R. L. Byer. Quasi-phase-matched second harmonic generation: Tuning and tolerances. *IEEE Journal of Quantum Electronics* **28,** 2631 (1992). 33, 50, 59

[42] M. Yamada, N. Nada, M. Saitoh, and K. Watanabe. First-order quasi-phase matched $LiNbO_3$ waveguide periodically poled by applying an external field for efficient blue second-harmonic generation. *Applied Physics Letters* **62,** 435 (1992). 34, 59

[43] C. E. Kuklewicz, M. Fiorentino, G. Messin, F. N. C. Wong, and J. H. Shapiro. High-flux source of polarization-entangled photons from a periodically poled KTiOPO$_4$ parametric down-converter. *Physical Review A* **69,** 013807 (2004). 34

[44] T. Kim, M. Fiorentino, and F. N. C. Wong. Phase-stable source of polarization-entangled photons using a polarization Sagnac interferometer. *Physical Review A* **73,** 012316 (2006). 34

[45] D. N. Klyshko. *Photons and Nonlinear Optics.* Gordon and Breach, pages 285-357, 1988. 34

[46] G. D. Miller. Periodically poled lithium niobate: modeling, fabrication, and nonlinear-optical performance. PhD Dissertation, Stanford Univ., (1998). 35, 59

[47] E. J. Mason. Applications of optical parametric downconversion: I. Self-phase locking; II. Generation of entangled photon pairs in periodically-poled lithium niobate. PhD Dissertation, MIT (2002). 35, 59

[48] R. Sobolewski, A. Verevkin, G. N. Goltsman, A. Lipatov, and K. Wilsher. Ultrafast superconducting single-photon optical detectors and their applications. *IEEE Transactions on Applied Superconductivity* **13,** 1151 (2003). 41

[49] O. Kuzucu, M. Fiorentino, M. A. Albota, F. N. C. Wong, and F. X. Kaertner. Two-photon coincident-frequency entanglement via extended phase matching. *Physical Review Letters* **94**, 083601 (2005). 43

[50] Y. R. Shen. *The Principles of Nonlinear Optics.* Academic Press, 2^{nd} edition, 1988. ISBN 0471889989. 48

[51] G. D. Boyd and D. A. Kleinman. Parametric interaction of focused gaussian light beams. *Journal of Applied Physics* **39,** 3597 (1968). 49, 50, 63

[52] G. J. Edwards, M Lawrence. A temperature-dependent dispersion equation for congruently grown lithium niobate. *Optical and Quantum Electronics* **16,** 373 (1984). 50

[53] D. H. Jundt. Temperature-dependent Sellmeier equation for the index of refraction, n_e, in congruent lithium niobate. *Optics Letters* **22,** 1553 (1997). 13, 21, 50, 59, 61, 66, 129

[54] J. M. Huang and P. Kumar. Observation of quantum frequency conversion. *Physical Review Letters* **68,** 2153 (1992). 57, 95

[55] H. Kogelnik and T. Li. Laser beams and resonators. *Applied Optics* **5,** 1550 (1966). 66, 67

[56] C. Langrock, E. Diamanti, R. V. Roussev, Y. Yamamoto, and M. M. Fejer. Highly efficient single-photon detection at communication wavelengths by use of upconversion in reverse-proton-exchanged periodically poled $LiNbO_3$ waveguides. *Optics Letters* **30,** 1725 (2005). 85, 91

[57] A. P. Vandevender and P. G. Kwiat. High efficiency single photon detection via frequency up-conversion. *Journal of Modern Optics* **51,** 1433 (2004). 90, 91

[58] R. V. Roussev, C. Langrock. J. R. Kurz, and M. M. Fejer. Periodically poled lithium niobate waveguide sum-frequency generator for efficient single-photon detection at communication wavelengths. *Optics Letters* **29,** 1518 (2004). 90